AVANCES EN SISTEMAS INTERACTIVOS PARA PERSONAS CON PARÁLISIS CEREBRAL

María del Pilar Maldonado Illescas

UNIVERSITAT
ROVIRA i VIRGILI

Spin Crossover Phenomena: Towards Molecule-based Memories and Switches

---

María del Pilar Maldonado Illescas

DOCTORAL THESIS
2017

UNIVERSITAT ROVIRA I VIRGILI
AVANCES EN SISTEMAS INTERACTIVOS PARA PERSONAS CON PARÁLISIS CEREBRAL
María del Pilar Maldonado Illescas

UNIVERSITAT ROVIRA I VIRGILI
AVANCES EN SISTEMAS INTERACTIVOS PARA PERSONAS CON PARÁLISIS CEREBRAL
María del Pilar Maldonado Illescas

DOCTORAL THESIS

Spin Crossover Phenomena: Towards Molecule-based Memories and Switches

María del Pilar Maldonado Illescas

supervised by

Prof. Dr. José Ramón Galán Mascarós

Institut Català d'Investigació Química (ICIQ)

UNIVERSITAT
ROVIRA i VIRGILI

UNIVERSITAT ROVIRA I VIRGILI
AVANCES EN SISTEMAS INTERACTIVOS PARA PERSONAS CON PARÁLISIS CEREBRAL
María del Pilar Maldonado Illescas

Prof. Dr. José Ramón Galán Mascarós, Group Leader of the Institute of Chemical Research of Catalonia (ICIQ) and Research Professor of the Catalan Institution for Research and Advances Studies (ICREA),

STATES that the present study, entitled "**Spin Crossover Phenomena: Towards molecule-based memories and Switches**", presented by María del Pilar Maldonado Illescas for the award of the degree of Doctor, has been carried out under my supervision at the Institute of Chemical Research of Catalonia (ICIQ).

Tarragona, May 1st 2017

Doctoral Thesis Supervisor

Prof. Dr. José Ramón Galán Marcarós

UNIVERSITAT ROVIRA I VIRGILI
AVANCES EN SISTEMAS INTERACTIVOS PARA PERSONAS CON PARÁLISIS CEREBRAL
María del Pilar Maldonado Illescas

Contents

UNIVERSITAT ROVIRA I VIRGILI
AVANCES EN SISTEMAS INTERACTIVOS PARA PERSONAS CON PARÁLISIS CEREBRAL
María del Pilar Maldonado Illescas

Summary and objectives

Nowadays, the idea that molecules can be used as a target in an electronic device arouses scientific community around the World. The information storage capacity from technological demand a growing exponentially and depend on the development of Nanoscience. The aim is the storage of data quicker and the miniaturization of the devices and because of this, one of the most promising strategies is based on the concept of bistability between two electronic states of a molecule passing from one state (OFF) to another state (ON) under the influence of an external stimulus.

The objective of this thesis is the performance of new Iron (II) based 1,2,4-triazole derivatives, specifically anionic spin crossover compounds and spin crossover polymers in order to have the fundamental elements in the development of multifunctional materials. Moreover, we carried out successfully the incorporation in conducting polymer forming composites so as to approach to real application such as devices or switches.

In chapter 1, a brief introduction is presented to introduce the broader goal of our research.

In Chapter 2, we performed the synthesis of a new anionic spin crossover compound with room temperature hysteresis loop. We performed fortunately a trimer formed by three Iron (II) where the central Iron can be populated (compound **1**). Moreover, exploiting the

cation exchange, we can obtain successfully other compound which magnetic properties were tuned (compound **2**).

In chapter 3, we formed a composite based on a commercial conducting polymer, PEDOT:PSS and **1**. We observed a synergy between polymer and SCO, and present a precise effect in the physical properties. Moreover, we achieved an improvement in the T_{TIESST}, a record value in this kind of materials.

In chapter 4, we carried through the accomplishment of a composite formed by an Iron (II) 1,2,4-triazole polymer and polypyrrole. We synthetized this films at different pressures to see the effect in transport measurements. We observed an unmistakable evidence of bistability reaching also a record in the average, not observed in this class of materials.

Finally, in chapter 5, we exploited the thermoelectric behavior in an Iron (II) 1,2,4-triazole-derivative polymer and polypyrrole. We improved successfully the average in electric properties due to a betterment in the procedure of synthesis. In addition, an important improvement in the thermoelectric mechanism, due to the increasing of dopants in the polymer.

CHAPTER 1

Introduction

UNIVERSITAT ROVIRA I VIRGILI
AVANCES EN SISTEMAS INTERACTIVOS PARA PERSONAS CON PARÁLISIS CEREBRAL
María del Pilar Maldonado Illescas

1.1. Introduction to the spin crossover behavior

Cambri et al. observed in 1931 the first anomaly in the magnetic behavior with their compounds based on Iron (III) and dithiocarbamate [1]. This phenomenon was later called spin conversion or spin transition, currently known as spin crossover.

Spin crossover material is a compound that exhibits changes due to some external stimuli such as pressure, temperature, light or magnetic field [2, 3]. This process involves the rearrangement of electrons in a metal ion, usually d^4- d^7 electronic configuration and it is common in octahedral coordinated complexes in first row transition metal ions. Metallic centers which can present SCO are: Chromium (III) and Chromium (II) [4, 5], Manganese (III) [6, 7], and Manganese (II) [8, 9], Iron (III) [10, 11], and Iron (II) [12, 13]; Cobalt (II) [14, 15] and Cobalt (III) [16, 17].

In 1929, Crystal Field Theory arose to support this electronic distribution proposed by the physicist Hans Bethe [18]. Few years later, in 1935, J. H. Van Vleck introduced some variations in paramagnetic anisotropy [19].

1.1.1. Crystal field theory

Based on an electrostatic model, Crystal Field Theory describes the electron distribution in the orbital d or f of a metallic ion under different symmetries and explains the interactions between metal and ligand coordination complexes with transition metals being a good base to explain the phenomenon of spin transition. The metal is positively charged while the ligands have negative charge [20]. This implies an electrostatic attraction between the pairs of electrons of the ligands and the positively charged metal ion. This simple model supposes a free and gaseous metal ion, the ligands involve as point charges and there is not interaction between the orbital of the metal and the orbital of the ligand. Firstly, the approximation of the ligand electrons to the metal ion modifies the energy of metal ion d orbitals. Depending on the geometry of the complex, the metal orbitals along the bonding directions with the ligands will increase their energy, while the electrons located between them decrease their energy.

For octahedral complexes and more specifically Iron (II) complexes, the most used metal in this thesis; the six ligands are distributed along the cartesian axes, as shown in the figure 1.2.

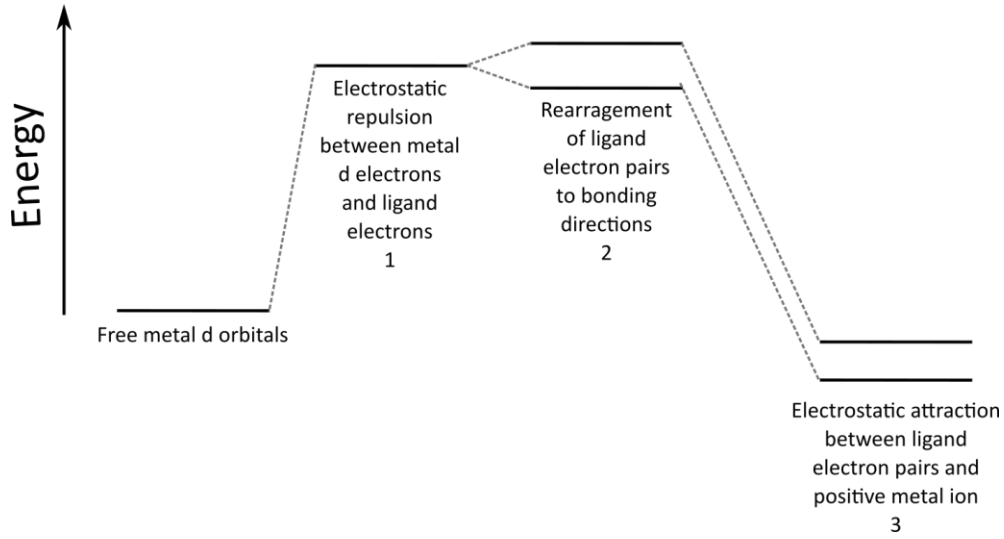

Figure 1.1. The hypothetical steps in complex ion formation according to crystal field theory

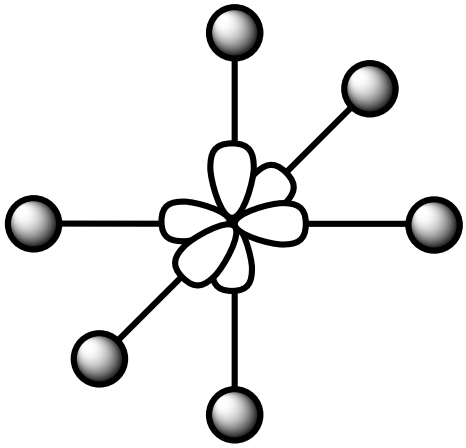

Figure 1.2. Orientation of six ligands respecting the d metal orbital

As a result of the presence of these negative charges, the d_{x2-y2} and d_{z2} orbital energies will be considerably higher than the others, with the energy difference defined as 10Dq [21].

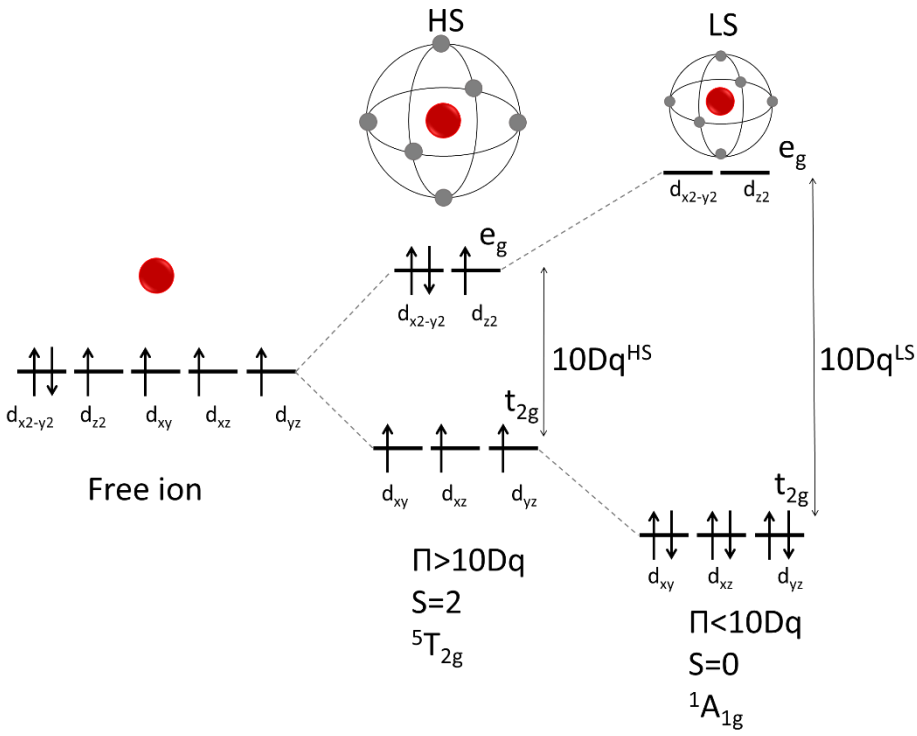

Figure 1.3. Separation of the d orbitals in an octahedral environment induced by the ligand field strength 10Dq

When 10Dq is lower than the electron spin pairing energy (Π), in a weak ligand field configuration, the electrons in the complex follow Hund's rule of maximum multiplicity. The number of unpaired electrons is maximized and the electrons occupy also the high energy orbitals, being the total spin, *S*=2, for the Iron (II). In this case, the paramagnetic state is called High Spin (HS) (Figure 1.3, right). On the other hand, strong ligand fields generate systems where 10Dq is larger than Π, favoring electron pairing since

María del Pilar Maldonado Illescas

the low energy orbitals are preferably occupied. This situation generates a total spin, *S*=0, for Iron (II). This diamagnetic state is named Low Spin (LS) (Figure 1.3, left). Therefore, spin transition occurs between these two states, the 1A1 singlet state (LS) and the 5T2 quintet state (HS).

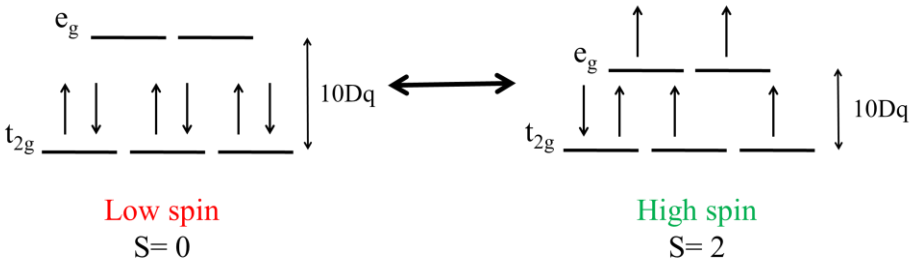

Figure 1.4. The two possible spin states for a d^6 metal ion when the metal is split by an octahedral ligand field, 10Dq

The relationship between these two states and the strength of the ligand field in an Iron (II) complex with an octahedral environment can be preceded with the *Tanabe-Sugano diagrams* [22, 23] .

1.1.2. Tanabe-Sugano diagrams

Tanabe-Sugano diagrams represent the energy of each electronic state respect to the strength of the ligand field. Thus, for an octahedral environment d^6 the free electron ground state is 5D, but under the influence of the ligand field this state is split into two, the new ground state, which is the named $5T_{2g}$ (High Spin state) and an excited state, which is called the $5E_g$ state (Figure 1.5). The $5T_{2g}$ state remains as a ground state and up to a value of approximately 10Dq = Π, which is called $10Dq_{crit}$. From this point the $1A_{1g}$ (Low Spin state) will be the new ground state.

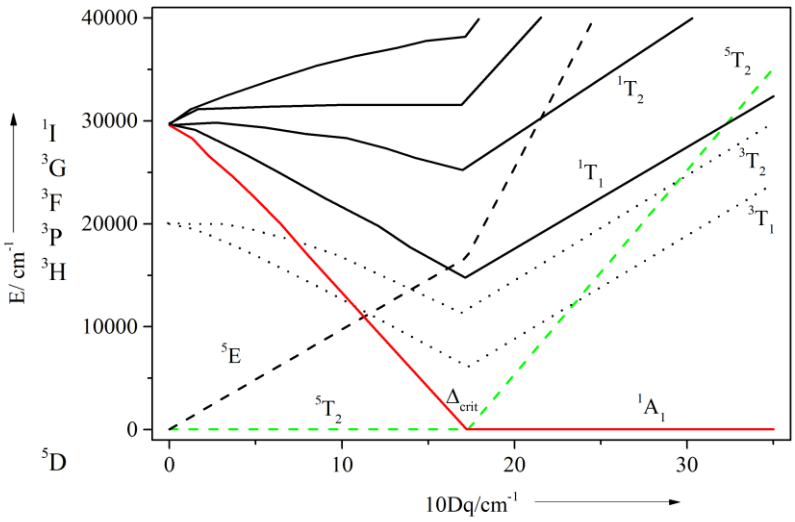

Figure 1.5. Tanabe-Sugano Diagrams for a d^6 metal ion

The ligand field strength is determined by the ligand features but also by other structural parameters the metal-to-ligand distance, and for Iron (II) the Fe-N distances and angles (Figure 1.6), supramolecular interactions, etc. The low spin state ($^1A_1$) has a low energy compared to the high spin state energy ($^5T_2$). On the other hand, the $^5T_2$ potential well is shifted a higher metal-to-ligand distance compared with $^1A_1$ potential well between 5-10%, and this value can be calculated by X-ray diffraction.

The crossing point of both states (curve) corresponds to the critical ligand field strength in the Tanabe-Sugano diagrams.

María del Pilar Maldonado Illescas

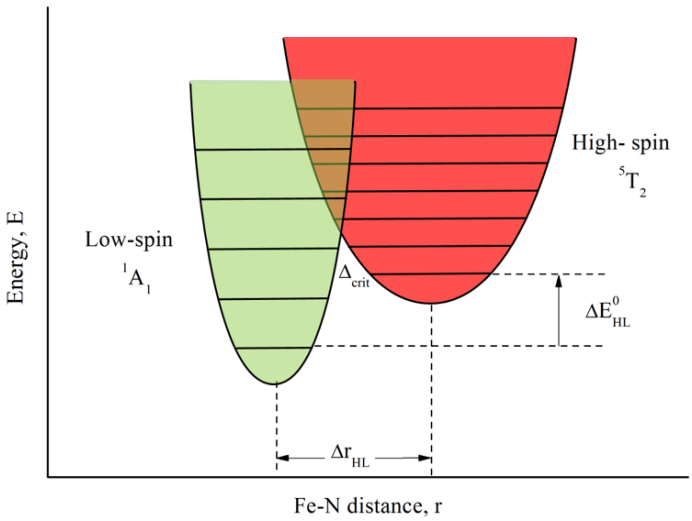

Figure 1.6. Schematic representation of the HS- $5T_2$ (red) and LS- $1A_1$ potential energy (green) for an octahedral Iron (II) complex in dependence of the metal-to-ligand distance, r

Considering the metal-to-ligand distance, for a coordination complex it is possible to calculate experimentally the energy according to a given distance:

$$10Dq(r) = 10Dq(r_0)\left(\frac{r_o}{r}\right)^6 \qquad (1.1)$$

which r_0 is the equilibrium distance.

However, for a spin crossover is possible to derive this formula and obtains an estimation, calculated as follow:

$$\frac{10Dq^{LS}}{10Dq^{HS}} = \left(\frac{r_{HS}}{r_{LS}}\right)^6 \approx 1.74 \qquad (1.2)$$

For a spin crossover compound with only one Iron (II), metal-to-ligand distance values usually range between 0.16 and 0.22 Å for both states,

specifically 1.96- 2.00 Å for low spin and 2.16-2.20 Å for high spin depending of the crystal structure [24-26].

The ranges of energy can be calculated with the values of 10Dq in all transition complexes, and theses ranges are:

$10Dq_{HS} < 11000\ cm^{-1}$	HS complex
$10Dq_{HS} \approx 11500\text{-}12500\ cm^{-1}$ **$10Dq_{LS} \approx 19000\text{-}21000\ cm^{-1}$**	Spin crossover complex
$10Dq_{LS} > 21500\ cm^{-1}$	LS complex

Table 1.1. 10Dq-ranges at which HS, LS or spin crossover complexes are expectable

The most common spin transition phenomenon is related with the temperature, moreover thermal-induced spin crossover phenomena are the most studied and this thesis are focused on it.

1.1.3. Thermal spin crossover behavior

In a spin crossover material, the ground state correspond to the LS configuration. However, the HS configuration corresponds to the first excited state and it can be thermally populated. The HS/LS distribution would depend on the temperature of the system, following a Boltzmann distribution [27]. Such a gradual transition (Figure 1.7.A) is the most common, and it was the only behavior observed until 1960 [28, 29].

In 1964, for the first time, a spin crossover compound exhibited an abrupt thermal-dependent curve. Baker and Bobonich carried out these measurements [30] for the $[Fe(phen)_2(NCS)_2]$ compound, being later verified by König and Hank [31]. The appearance of an abrupt transition is a consequence of the appearance of cooperativity due to the molecular interactions in a solid. This behavior is of elastic origin, due to the association of the spin transition with a crystallographic transition (figure 1.7.B).

Such cooperativity can give rise to the appearance of thermal hysteresis (figure 1.7.C). The first compound reported with a thermal hysteresis cycle is the $[Fe(4,7\text{-}(CH3)_2\text{-}phen)_2(NCS)_2)]$ discovered in 1976 by Konich and Ritter [32]. In this case, there are two transition temperatures, the heating transition temperature that appears in the heating branch and the cooling transition temperature for the cooling branch.

There are two possible origins of thermal hysteresis in spin transition curves; the spin transition can be due to a change of structural phase in the lattice or to an intramolecular structural change that propagates within the solid through the neighboring molecules promoting a high effective cooperativity between molecules [33]. The mod of these interactions is not always clear but it is generally accepted to be favored by intermolecular interactions. For example, π-π (including van der Waals) interactions between

aromatic moieties [10, 34]; hydrogen bonding in the coordination environment with other spin crossover centers via anion or solvent molecules [35, 36]; or with covalent bonds through multinuclear or polymeric coordination systems [37].

Spin transition can also take place by steps (Figure 1.7.D). The first spin transition compound by steps was obtained in 1981 by Zelentsov. The complex was an Iron (II) with 2-bromo-salyicylaldehyde-thiosemicarbazone [38]. This behavior appears when the spin crossover metal center occupies two or more different positions in the lattice [39, 40] .

Finally, spin transition can also be incomplete (Figure 1.7.E), where not all center can reach the LS or HS configurations. This can be due to the presence of impurities, or to dislocations and defects in the lattice, as a particular case of step transition.

María del Pilar Maldonado Illescas

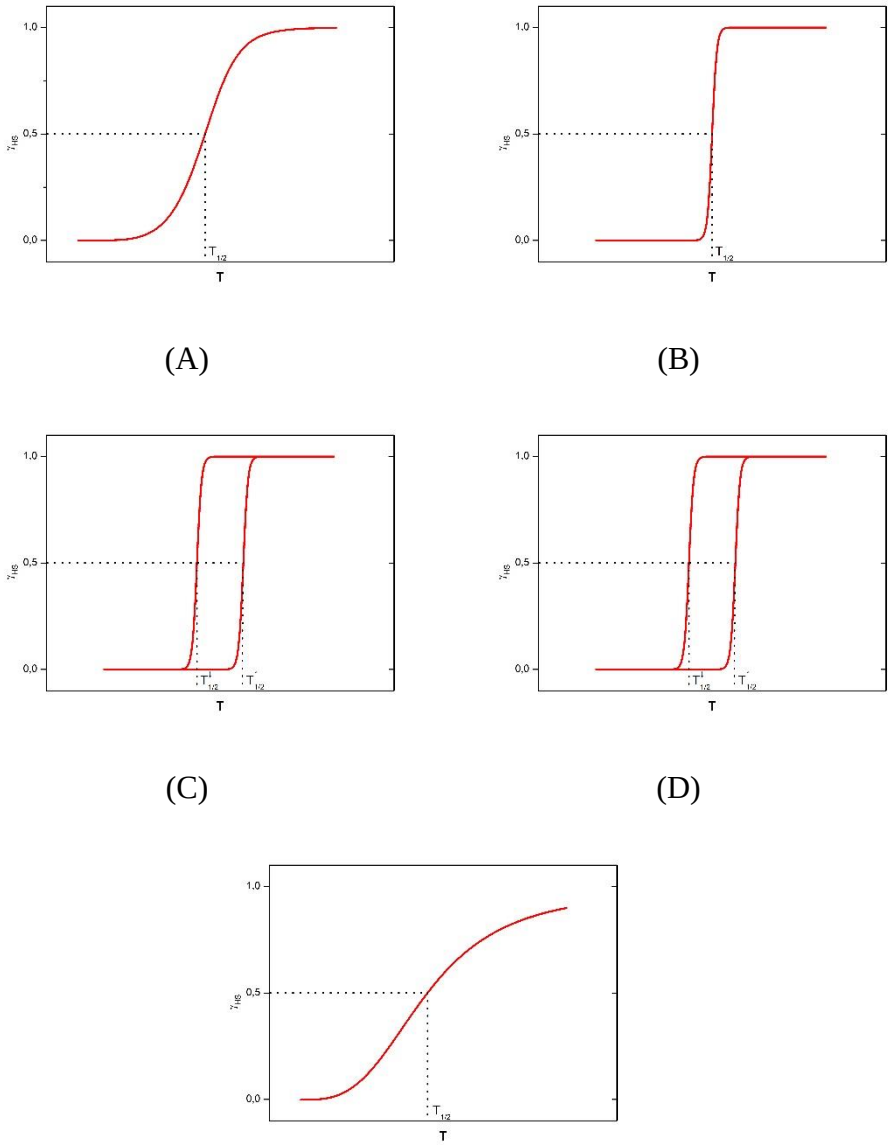

(A) (B)

(C) (D)

(E)

Figure 1.7. The nature of spin transition curves for spin crossover systems in solid state: γ_{HS} represents the high spin state fraction of complex molecule; A) Gradual, B) Abrupt, C) With hysteresis, D) With steps and E) Incomplete

1.1.4. Thermodynamic aspects in thermal spin crossover

The spin transition can also be characterized as a phase transition into a system of isolated low spin molecular system without any interaction between them under experimental conditions at same temperature and pressure. To determine which of the two states is more favorable the following expression is used:

$$\Delta G = G_{HS} - G_{LS} = \Delta H - T\Delta S \qquad (1.3)$$

where ΔG is the free energy of Gibbs for the system, ΔH and ΔS are the difference of enthalpy and entropy in the LS → HS transition, respectively [41, 42]. ΔH and ΔS are always positive and at the equilibrium temperature ($T_{1/2}$) can be defined as temperature where low spin state molecule fraction is the same as where high spin state molecule fraction. In this case, ΔG = 0, so $T_{1/2}$ can be defined as:

$$T_{1/2} = \frac{\Delta H}{\Delta S} \qquad (1.4)$$

ΔH consists of two contributions, an estimated electronic contribution, ΔH_{el} from 0 to 1000 cm^{-1} and an estimated vibrational part, ΔH_{vibr} at 100 cm^{-1}, so ΔH contribution is principally given by ΔH_{el} [43, 44].

On the other hand, the entropy variation ΔS has also two contributions. The first one, the electronic contribution, ΔS_{el} attributed to the change in the total spin momentum, *S*, (ΔS_{el}^{spin}) and the change in angular orbital momentum, *L*, (ΔS_{el}^{orb}) where the spin transition takes place. These two contributions can be expressed as a function of the spin and orbital multiplicities in these two molecular states:

María del Pilar Maldonado Illescas

$$\Delta S_{el}^{spin} = N_a k_B ln\left(\frac{2S_{HS}+1}{2S_{LS}+1}\right) \quad (1.5)$$

$$\Delta S_{el}^{orb} = N_a k_B ln\left(\frac{2L_{HS}+1}{2L_{LS}+1}\right) \quad (1.6)$$

For a ligand field with octahedral symmetry it is necessary to consider both contributions although in the most of cases the symmetry in the ligand field is lower than octahedral symmetry so the approximation $\Delta S \approx \Delta S^{spin}$ is taking into account for $1A_1 \rightarrow 5T_2$ transitions, being ΔS_{el}^{spin}= 13.38 $JK^{-1}mol^{-1}$ for an Iron (II) [45].

However, for an Iron (II) spin crossover, heat capacity measurements give values between 40-80 $JK^{-1}mol^{-1}$ [42]. This is a contribution in the vibrational part of the entropy difference, ΔS^{vibr} and comes mainly from the difference of the Fe-N distance and also FeN6 octahedron distortion [46]. From 1.3 and 1.4 equations we can deduce that, if $T < T_{1/2} \rightarrow \Delta H > T\Delta S \leftrightarrow GLS < GHS$, the enthalpy dominates and the electronic ground state is the low spin state, consequently, when $T > T_{1/2} \rightarrow \Delta H < T\Delta S \leftrightarrow GLS > GHS$, in this case the entropy becomes predominant and now the electronic ground state is the high spin state. Finally, if $T = T_{1/2} \rightarrow \Delta H = T\Delta S \leftrightarrow GLS = GHS$, enthalpy and entropy have the same value, and for this reason there is a balance in the two spin transition states [47].

Now, these processes can be simulated generally with a model introduced by Slitcher and Drickramer [48]. This theory introduces a new factor, Γ, where the cooperativity is taken into account. So, the free energy can be expressed in the following way:

$$G = n_{HS}G_{HS} + (1-n_{HS})G_{HS} + \Gamma n_{HS}(1-n_{HS}-TS_{mix}) \quad (1.7)$$

where Γ (P, T) describes the intermolecular interaction strength. Deriving this expression and considering a temperature and pressure balance, we get the following expression:

$$T = \frac{\Delta H + \Gamma(1 - 2n_{HS})}{N_a k_B ln\left(1 - n_{HS}/n_{HS}\right)} \tag{1.8}$$

the term R (Jmol^{-1}) (constant for an ideal gas) is more useful because is it more simple instead of $N_a k_B$.

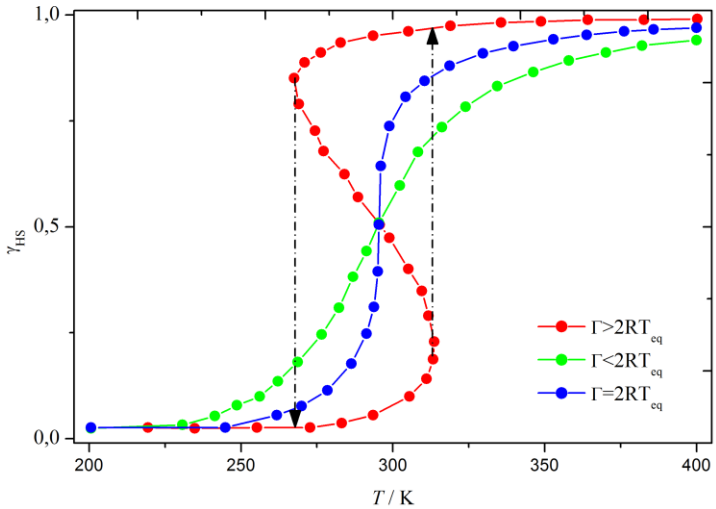

Figure 1.8. Simulations of spin crossover curves for different values of cooperativity (Γ) calculated with equation 1. The dotted lines correspond to the hysteresis phenomenon due to the presence of metastable states

María del Pilar Maldonado Illescas

Considering this, we have: firstly, if $\Gamma < 2RT_{eq} \rightarrow dT/dn_{HS} > 0$ so cooperativity is small and gradual curves is given; second if $\Gamma \approx 2RT_{eq} \rightarrow dT/dn_{HS} > 0$ is zero when $n_{HS} = 0.5$ creating an abrupt transition. Finally, in the case that $\Gamma > 2RT_{eq}$, the curve presents a minimum and a maximum, in this case there is hysteresis and shows a strong molecular interaction.

1.1.5. Detection of spin crossover phenomenon

There are various methods and techniques to follow a spin transition (table 1.2). Magnetic susceptibility as a function of temperature is the most used, not only in this thesis [49]. Currently, the high sensitivity of SQUID (Appendix I) or Foner magnetometer (vibrating sample magnetometer) allows very reliable detection techniques for spin crossover.

The second most used technique is Mössbauer spectroscopy, especially in ^{57}Fe samples [50]. Due to the high energy and extremely narrow line widths of gamma rays, Mössbauer spectroscopy is one of the most sensitive techniques [51].

Usually, the Mössbauer spectra have different curves for every spin transition state; so, for a high spin Iron (II) shows a high quadrupole splitting and an isomer shift while in a low spin Iron (II) these parameters are usually smaller [27].

Another useful technique is UV-vis spectroscopy. Even the naked eye can follow the color change due to the spin transition (from white/yellow to pink/purple in an Iron (II)-N). In a high spin state, a band close to the NIR

appears related to the $1A_1 \rightarrow 1T_1$ transition. The $1A_1 \rightarrow 1T_2$ transition presents in the UV-vis region [52].

NMR spectroscopy following Evans method for paramagnetic studies is particularly useful for solution studies [53-55]. However, this technique presents a disadvantage; the measurement temperature is limited by the melting and boiling points of the solvent.

X-ray diffraction spectroscopy is also a common technique for solid state characterization. As we have already mentioned the metal-to-ligand distances change. Therefore, upon the spin transition, lattice parameters must change (displacive transitions) even if the space group is maintained, as observed in continuous transitions[56]. In some cases, a change in the space group can be produced (discontinuous spin transition), in particular when rearrangement of the lattice packing takes place [57].

Finally, Differential Scanning Calorimetry (DSC) provides heat capacity data, directly related to changes in enthalpy and entropy during the spin transition. These important thermodynamic values also allows gathering additional information on the origin of cooperativity and hysteresis, as previously discussed [58-61]. Remarkably, Sorai and Seki first employed this technique in their spin transition compounds of the classical complexes $[Fe(phen)_2(NCX)_2]$ con X=S, Se [46, 47].

Analytical method	Characteristic value
Magnetic measurements	Magnetic susceptibility (Effective magnetic moment)
Mössbauer spectroscopy	Isomer shift Quadrupole splitting
UV-Vis spectroscopy	d-d / CT excitation energy
NMR spectroscopy	Paramagnetic chemical shift Magnetic susceptibility
X-ray structure analysis	Metal-to-ligand distance
Calorimetry	Heat capacity

Table 1.2. Overview of the experimental methods most commonly used to follow spin transition

1.1.6. Physical influences in a spin crossover in solid state. Light or pressure

As previously mentioned at the beginning of this thesis, the spin transition may be affected by temperature, pressure or light. In this section we will discuss the phenomena affected by pressure and light radiation.

McGravey et al. in 1982 were the pioneers who observed spin crossover in an Iron (II) complex by pulsed laser irradiation [62]. Later, in 1984, Decurtins et al. discovered a complex with Iron and 1-propyltetrazole in a metastable high spin state at low temperature and with a virtually infinite lifetime when it was irradiated with light. This

phenomenon was called LIESST effect (Light-Induced Excited-Spin-State Trapping) [63, 64].

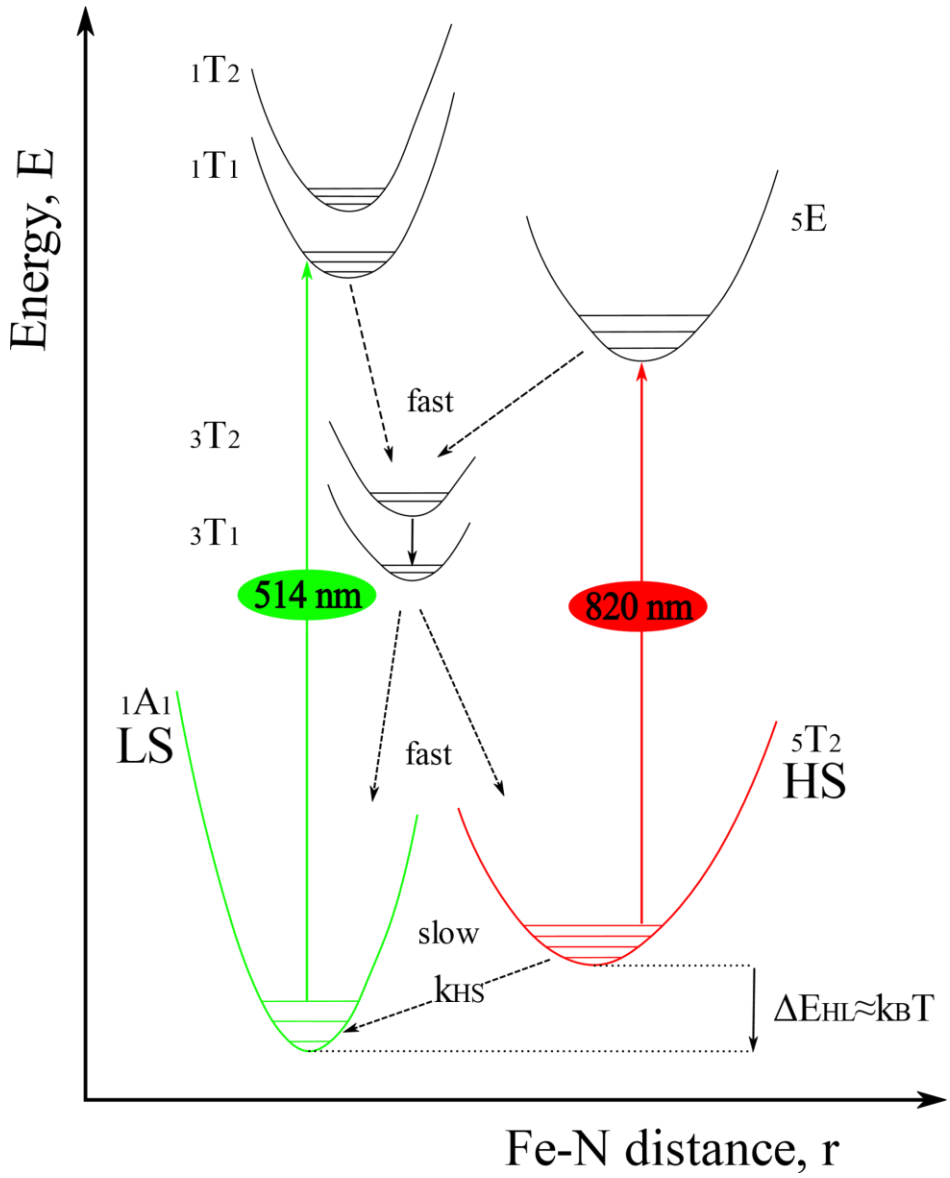

Figure 1.9. Schematic illustration of the electronic structure of the LIESST effect and reverse LIESST effect for a d6 complex in the spin crossover range

María del Pilar Maldonado Illescas

For a d^6 metal complex in the range of spin crossover, the mechanism of this process consists first in the $^1A_1 \rightarrow {}^1T_1$ excitation in a low spin compound by green light irradiation (514 nm) at temperatures under 50 K. The $^1T_1$ excited state has a half-life of 50 ns. However, it is possible that $^1T_1$ excited state decline by a double intersystem crossing through $^3T_1$ intermediate state, to achieve finally the $^5T_2$ high spin state. On the other hand, at low temperatures, the $^5T_2 \rightarrow {}^1A_1$ radiative relaxation is forbidden and the decay is slow and occurs by thermal tunneling to the $^1A_1$ ground state. In addition, it is also possible to reverse the population of states quantitatively. Decurtins et al. also introduce this phenomenon and it is denominated reverse LIESST [65, 66] , with the transformation a metastable high spin state in a low spin state by red light irradiation (820 nm), more specifically $^5T_2$ state is excited to ^5E state with the subsequent intersystem crossing processes ($^5E \rightarrow {}^3T_1 \rightarrow {}^1A_1$), allowing the transition to the low spin state (Figure 1.9). From here, many compounds with LIESST effect were found.

On the other hand, spin transition with pressure is the least studied field in spin crossover. It is well-known that spin crossover implies a considerable change in molecule volume from low spin to high spin, more specifically, metal volume, Iron (II) for this thesis.

The promotion of low spin state is the first effect where pressure is involved, metal-to-ligand distance is shorter and therefore, volume is smaller. Generally, transition temperatures change to higher values and there is an increase in the energy (zero-point energy separation) $AE°_{HL}$ [67].

Furthermore, the field approximation of free energy depends in this case of pressure and the pressure dependence of the thermal spin transition [27] is given by:

$$\frac{\partial T_{1/2}}{\partial p} = \frac{\delta v_{HL}}{\Delta s_{HL}} \tag{1.9}$$

where $\delta v_{HL} > 0$ is the volume change at molecular level and $\Delta s_{HL} > 0$ is the entropy change at the transition temperature. Moreover, there is a decrease in the width of the transition hysteresis when pressure increases [68].

Many researchers have worked in spin crossover by pressure, but Ewald et al. experimental studies are of particular interest. They performed their studies in solution at different pressures with an Iron (III) with dithiocarbamate [69]. Ewald suggested that the $^2T_2$ low spin state is favorable between $^2T_2$→ $^1A_1$ states when pressure is applied in a thermal-dependent equilibrium (Figure 1.10). Later, Drickamer et al. continued in this field with their studies in the Iron complex, $[Fe(phen)_2(NCS)_2]$, at different pressures. They monitored the effect by Mössbauer spectroscopy where pressure-dependent HS→ LS conversion appears clearly. A subsequent study performed by Usha, Srinivasin and Rao complete with the temperature-dependent study of the $[Fe(phen)_2(NCS)_2]$ and $[Fe(b\text{-}py)_2(NCS)_2]$ complexes at different pressures [70]. For the first complex, transition temperature moves to high temperatures and becomes more gradual as pressure increases. On the other hand, in the case of bipyridine complex, when temperature is close to transition temperature an increase of low spin fraction is appear maybe due to an increase of d- electron coupling strength, in the quintet state complex.

María del Pilar Maldonado Illescas

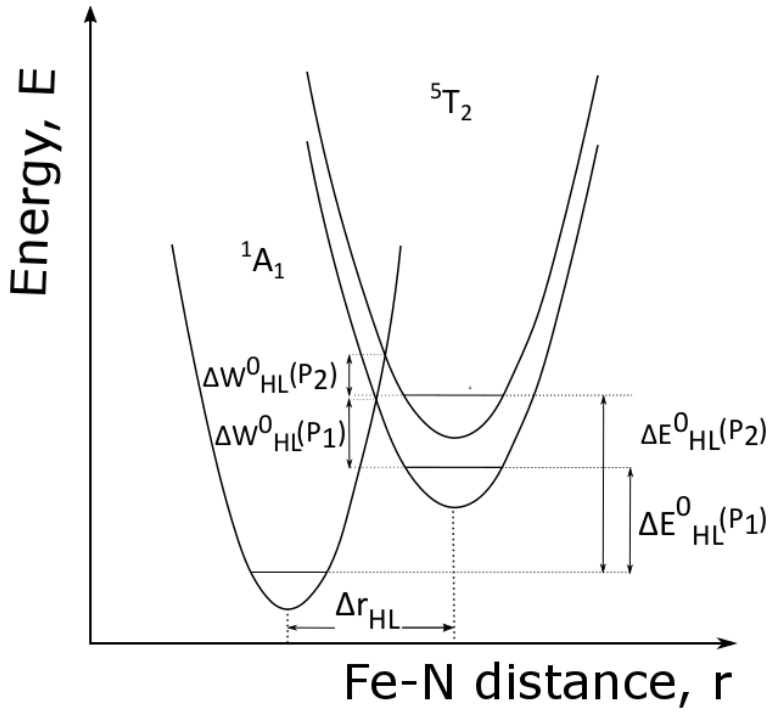

Figure 1.10. Schematic representation of pressure influence (when P2 > P1) on low spin and high spin Wells potential in an Iron (II) complex

1.1.8. Chemical influences in a spin crossover in solid state

Until now, we have explored the changes generated from some certain external stimuli; now, we also can modulate certain chemical properties to modify the magnetic behavior. There are many factors, which are viable to modify them; here we will list and explain briefly with examples some of them focusing of course in Iron (II) complexes.

A) Ligand replacement or intraligand substitution influence

A ligand exchange can modify the magnetic behavior, which is named in the table 1.3 [71]. For example, in the classic coordination compound $[FeX_2(phen)_2]$ depending on the coordinated ligand presents diverse magnetic properties. In the case of the complexes with Cl, Br and I, spin transition does not occur and the effective magnetic moment is close to 5 BM (always in high spin state). On the other hand, if we substitute these ligands by -NCS or –NCSe magnetic behavior is completely different, spin transition occurs and the effective magnetic moment goes from 1.4 BM (S = 0) to 5 BM (S = 2) approximately. Baker and Bobonich were the first who proposed a theory for this behavior [30], postulating thiocyanate and selenocyanate complexes form an antiferromagnetic coupling between paramagnetic iron centers.

Compound	T / K	μeff / BM
$[FeCl_2(phen)_2]$	-	5
$[FeBr_2(phen)_2]$	-	5
$[FeI_2(phen)_2]$	-	5
$[Fe(NCS)_2(phen)_2]$	180	1.4-5
$[Fe(NCSe)_2(phen)_2]$	230	1.4-5

Table 1.3. Magnetic properties of $[FeX_2(phen)_2]$

B) Metal dilution. Formation of mixed crystals

Magnetic behavior can also be modified with the formation of a mixed crystal, where there is a spin crossover metal and a diamagnetic or without spin crossover metal. Sorai et al. proposed the doping of an Iron salt, $[Fe(2\text{-}pic)_3]Cl_2$ where 2-pic = picolylamine with a Zinc salt resulting a mixed salt $[Fe_xZn_{(1-x)}(2\text{-}pic)_3]Cl_2$ [50]. They observed an influence on the thermal-dependent curves when a dilution of iron salt is done and thermal-dependent curves were more gradual and the transition temperature was lower when Zinc content increased. More Zinc concentration implies a decrease of Iron interactions, and a reduction of the cooperativity.

Experiments of dilution of the metal Center with other such as Mn, Co and Zn have the same behavior in all cases, so decreasing the content of iron in the molecule to promote the high-spin [27].

C) Ion exchange of not coordinating ligands

Not coordinating ligands is refered to ligands that do not form part of the sphere of coordination, but they are part of the molecule to compensate the load. These non-coordinating ions can make modifications in their crystalline structure, making different packings (lattices) so that the proximity between the Central metal atoms can vary and therefore modify the magnetic properties. The influence of ligands not coordinates was reported with the salt of $[Co(terpy)_2]^{2+}$ [72]. A clear example are strings formed from an Iron (II) Center metal and 1, 2, 4-triazole specifically, $[Fe(Rtrz)_3][A]_2$ structure. Later, there will be a section referred only to this.

Triazole (Rtrz)	Anion (A)	T / K	ΔT / K	Reference
1,2,4-triazole	BF_4^-	323/345	22	[73]
	ClO_4^-	341/358	17	[73]
	PF_6^-	269-279	10	[73]
4-amino-1, 2, 4-triazole	BF_4^-	250/260	10	[74, 75]
	ClO_4^-	247/249	2	[74, 75]
	PF_6^-	180	-	[74, 75]

Table 1.5. Magnetic properties of $[Fe(Rtrz)_3][A]_2$

It is possible to appreciate not only the exchange of ligand can modify those properties. But it is curious that we also observed many changes only by changing the contranion, that modifies not only the heating and cooling transition temperatures, but also the hysteresis width (table 1.5).

D) Modifications in the uncoordinated solvent

When a molecule is in crystalline state, the solvent (Crystal solvent molecules) usually is part of its structure without forming part of the sphere of coordination. It also causes influences in its structure. An example was the proposed Real et al. [76] where studied only its crystal structure and magnetic properties of the complex $[Fe(tap)_2(NCS)_2]\cdot nCH_3CN$ where tap = 1, 4, 5, 8-Tetraazaphenanthrene and n can be 1 or 0.5 (table 1.6).

The change of the amount of present acetonitrile molecules per unit cell can modify the crystal structure, the space group is different, the crystal parameters are also different, and therefore there is a modification in the metal distances.

Content of solvent	n = 1	n = 1/2
Space group	Triclinic, P1	C2/c
a/Å	8.920 (3)	22.636 (4)
b/Å	9.372 (3)	16.810 (3)
c/Å	16.838 (4)	18.528 (3)
α/º	96.32 (2)	-
β/º	100.47 (2)	138.55 (3)
γ/º	112.14 (2)	-
V/Å^3	1257.30	4666.90
Tsco / K	168	-

Table 1.6. Crystallographic data depending of the solvent content

In addition, the magnetic behavior modifies extraordinarily because there is, for example, in the case of salt that contains more acetonitrile transition of spin stood at 168 K transition temperature, while in the case of the structure that contains less acetonitrile there is no spin transition and compound will always be in high spin state.

E) Size of nanoparticles

Finally, I want to focus on modifications that the particle size may be altered. It is common the synthesis by reverse micelle technique, which allows adjust the particle size. Bousseksou et al. [77] have demonstrated that the particle size in Iron (II) nanoparticles plays an important role in magnetic behavior. They synthetized the [Fe(pz)(Ni(CN)$_4$)] and modifying sample preparation conditions it is possible to obtain different size particles. Smaller particles have lower temperature transition and the loss of cooperativity (loss of hysteresis) but surprisingly there is appearance of hysteresis at very low

values of particle size due possibly to the size-dependent elastic properties of the nanoparticles related with the surface tension.

1.1.9. 1, 2, 4-triazoles in coordination chemistry

The use of 1, 2, 4-triazole in spin crossover complexes are very common due to principally to the sites of coordination because they can obtain two or more sites of coordination. Moreover, for example the unsubstituted triazole (Htrz) (one of the ligand used in this thesis) is not only the form when the complex is formed; it is possible coordinated with the deprotonated form (trz^-), obtaining multiple complexes, every one with a magnetic behavior completely different [73].

It is well known the endless possibilities in synthesis of complexes with triazole, and in particular with 1,2,4- triazoles being possible the obtaining of mononuclear species [78, 79], binuclear [80, 81] or trinuclear bridges [82, 83], polymers [84] or networks [85, 86].

Htrz and its derivatives are usually coordinated to the metal ions by the 1- and 2- positions in a bridging mode [87]. The first polynuclear Iron (II) compound was $[Fe(Htrz)_2(trz)]BF_4$ obtaining by Haasnoot et al. [88]. From here, many compounds were synthetized with multiple magnetic behavior [73]. The metal ion are connected by a triple μ-N1-N2-triazole bridge resulting a linear chain shown in figure 1.11 and one of the triazole are deprotonated. The structure was explained by EXAFS [89] and XAS [90].

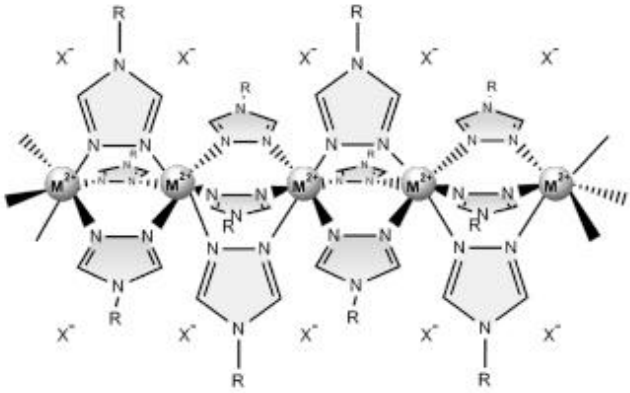

Figure 1.11. Structure of a 1,2,4-triazole chain polymer

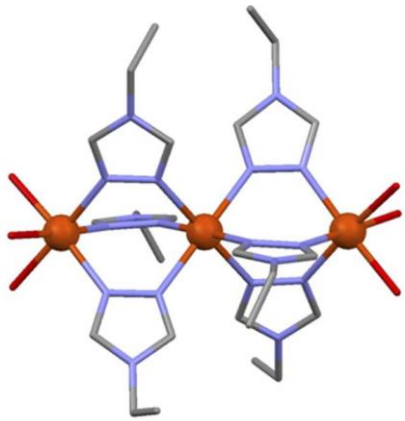

Figure 1.12. Structure of a 1, 2, 4-triazole trimer

Moreover, many compounds with these kind of ligands show a magnetic behavior close to room temperature, one of the aim of this thesis, because it is a fundamental element for real applications such as in the production of memory devices [91-93], sensors [94, 95] or combining with other compounds forming composites [96].

In addition, it is possible to obtain trimers united by μ-bridges between transition metals. The first trimer with triazole as ligand have been isolated in 1983 by Haasnoot [97]. The structure show a linear trinuclear unit formed by

two successive groups of three N1,N2- triazole ligands. The central iron can populate from low spin to high spin because it is octahedrally surrounded by six triazole N-donors, favorable for spin crossover transition. The axial iron are complexed with three molecules of water. (Figure)

1.2. Introduction to polymers

A polymer is a molecule formed by a repetition of structural units named monomers united by covalent bonds. The process were a monomer is able to bond other monomers forming long chains is called polymerization reaction [98]. The first polymer were discovered and patented by Alexander Parke in 1856 [99].

1.2.1. Type of polymers

Polymers can divided in two kind of polymers, the first one are the biopolymers responsible of the structural formation in living organisms, including DNA, proteins, nucleic acids or cellulose [100]. Synthetic polymers are the second group, which are synthetized in the laboratory, as the concrete, glass, glues or plastics.

On the other hand, the type of composition is other classification. There are two types of polymers; the homopolymers and the copolymers; the first one are composed only by one kind of monomer while the copolymers are formed by more than one kind of monomer. Copolymers can be found in nature and synthetized in the laboratory.

María del Pilar Maldonado Illescas

Finally, the most interesting organization of polymers in this thesis is attending to their properties. Multiple properties are presented in the polymers, in addition to the applications. Therefore, the most employed and the most important in this thesis are the conducting polymers.

1.2.2. Conducting polymers

In the past, polymers have been considered insulating polymers but, in 1976, Shirakawa et al. discovered a conducting polymeric compound when polyacetylene were doped with iodine. Later, in 2000, they won the Nobel Prize [101, 102]. From here, the obtaining of new conducting polymers were a priority y their applications were greater and greater. In fact, as of today, the use of these polymers is very common, for example, in sensors and biosensors [103, 104], for anticorrosion coatings [105, 106], in solar cells [107, 108], in light-emitting devices [109, 110] and much more. Because of their extraordinary properties such as electrical characteristics, controllable chemical and electrochemical properties and simple procesability many conducting polymers for example polyacetylene, polyaniline, polypyrrole, poly(phenylene)s, Poly(p-phenylene), poly(p-phenylenevinylene), poly(3,4-ethylene dioxythiophene), polyfuran and other polythiophene derivatives have awaken interest in the field of Nanoscience and Nanotechnology [111-113].

The requirement that a conducting polymer has to achieve are; firstly, it have to possess alternating double bonds. Every bond has a delocalized σ bond, which makes a strong chemical bond. Moreover, every double bond also contains a less strong localized bond (π bond) which is smoother. In order to understand this behavior, models are used, adapted to this field. So, all materials can be classified with their conducting properties (Figure). Thus,

polymers are semiconductors, being some polymers to metallic behavior, and this can be explained with the band theory.

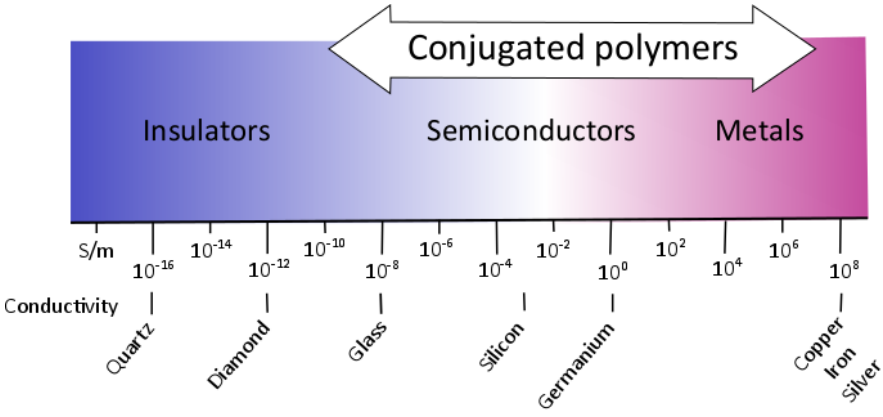

Figure. Range of conductivity of some common conducting materials

1.2.3. Band theory

First, polymers follow the band theory for a semiconductor. Band theory describes the electronic configuration in a material as bands, which correspond to the overlap orbitals in an atom, forming molecular orbital bands. For subsequent explanation, a quick definition of this theory are given, where there is a conduction band in a solid and a valence band, separated by a forbidden band or bandgap (figure). Valence band is the energy band occupied by the electrons in the last energetic level in an atom. The conduction band is the energy band occupied by the free electrons (the responsible of the electrical conduction). Finally, the forbidden band or bandgap is the band of energy required to an electron of the valence band goes to the conduction band.

María del Pilar Maldonado Illescas

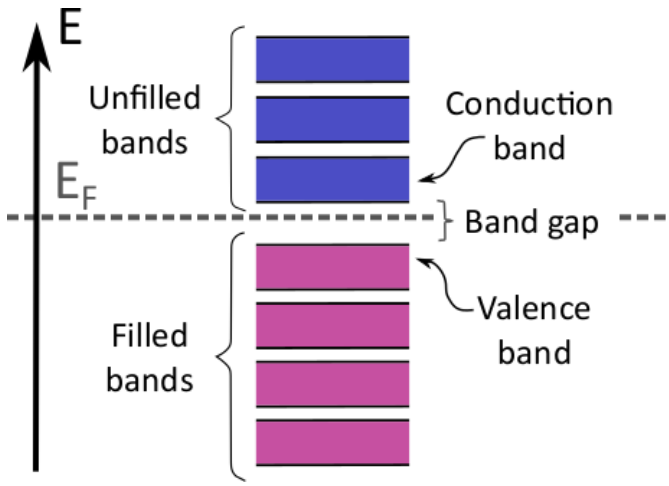

Figure. Schematic representation of the energy band in a solid

Thus, in an insulator material, the conduction band and the valence band are much separated (≈ 10 eV), requiring a very high energy to be excited. On the other hand, for conducting material, the conduction band and the valence band are overlap, and it is not necessary some energy to reach the conduction band. In a semiconductor, the bandgap is narrow, allowing the electron jump (figure).

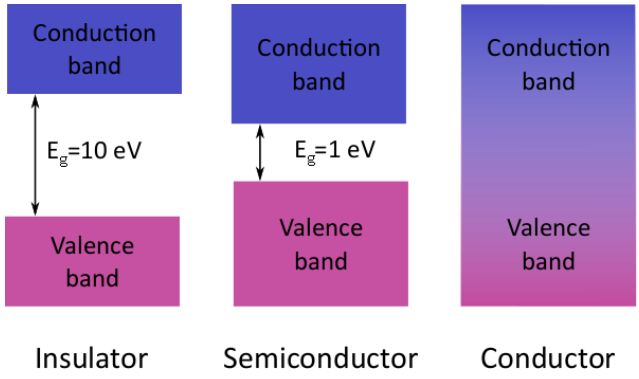

Figure. Diagrams of energy bands for conducting, semiconducting and insulator materials

This theory is related with inorganic simple compounds, but it is not completed in the case of polymers.

Band theory supports the understanding of how transport in a polymer works and is completed with the conduction model, that it will explained following.

1.2.4. Conduction model

The conduction model rises up in order to complete the behavior in semiconductors, because the most of conducting polymers are semiconductors, specifically extrinsic semiconductor, and there are some polymers with metallic character.

Extrinsic semiconductors base their semiconductivity in the added dopant. There are two types of semiconducting polymers, all based in the added dopant or the kind of preparation. The dopant can modify drastically the conducting properties and it is an important factor to modulate the grade of conduction in a material.

First of all, it is the p-type dopants, where the conduction are based in holes and the n-type dopants where the conduction are based on the contribution of impurities which take part electrons (figure).

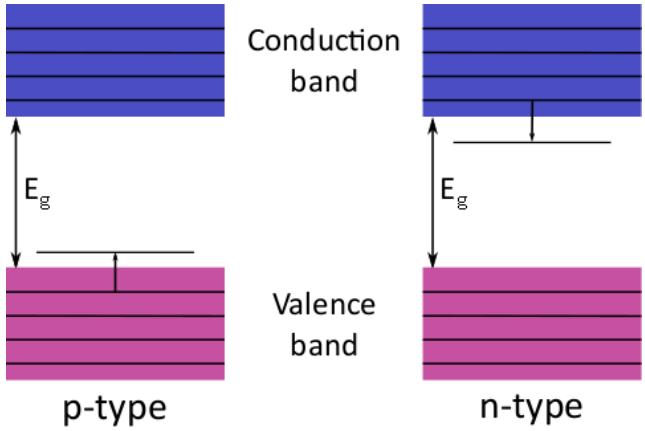

Figure. Type of doping which polymers are put down, left, p-type extrinsic doping and right, n-type extrinsic doping

On the other hand, intrinsic semiconductors are based in pure material, where the electron and hole concentration are the same because processes that provide an electron in the conduction band producing a hole in the valence band.

1.2.5. Examples of conducting polymers

Here, in this section the principal polymers employed in this thesis are summarized.

A) Poly (3,4-ethylenedioxythiophene) (PEDOT)

PEDOT is a conducting polymer based on 3,4-ethylene dioxyl thiophene monomer. It is very common their applications in high conductive organic light emitting diode displays [114], nano-fiber electrodes for unit simulation [115], solar cell [116], cathode material in electrolytic capacitors [117] and transparent electrodes for thick-film electroluminescence [118] Moreover, the principal advantages are the optical transparency in thin, very high stability, reasonable band gap, oxidized films and low redox potential [119].

B) Polypyrrole (PP)

PP is a type of organic polymer formed by polymerization of pyrrole and discovered in 1968. Polypyrrole has been widely studied due to its ease of preparation, superior redox properties [110], stabilized oxidized form, capacity to give towering conductivity [120], water soluble, commercially accessible and valuable electrical and optical properties.

1.3. References

1. Cambi, L. and A. Cagnasso, Atti Accad. Naz. Lincei, 1931. **13**.
2. Gütlich, P., A.B. Gaspar, and Y. Garcia, *Spin state switching in iron coordination compounds.* Beilstein Journal of Organic Chemistry, 2013. **9**: p. 342-391.
3. Real, J.A., A.B. Gaspar, and M.C. Munoz, *Thermal, pressure and light switchable spin-crossover materials.* Dalton Transactions, 2005(12): p. 2062-2079.
4. Halepoto, D.M., et al., *Spin crossover in chromium(II) complexes and the crystal and molecular structure of the high spin form of bis[1,2-bis(diethylphosphino)ethane]di-iodochromium(II).* Journal of the Chemical Society, Chemical Communications, 1989(18): p. 1322-1323.
5. Halepoto, D.M., et al., *Spin crossover in chromium(II) complexes.* Polyhedron, 1989. **8**(13): p. 1821-1822.
6. Sim, P.G. and E. Sinn, *First manganese(III) spin crossover, first d4 crossover. Comment on cytochrome oxidase.* Journal of the American Chemical Society, 1981. **103**(1): p. 241-243.
7. Morgan, G.G., et al., *A Manganese(III) Complex That Exhibits Spin Crossover Triggered by Geometric Tuning.* Angewandte Chemie International Edition, 2006. **45**(43): p. 7192-7195.
8. Scheuermayer, S., et al., *Spin crossover in phosphorus- and arsenic-bridged cyclopentadienyl-manganese(ii) dimers.* Chemical Communications, 2012. **48**(65): p. 8087-8089.
9. Ammeter, J.H., R. Bucher, and N. Oswald, *High-spin-low-spin equilibrium of manganocene and dimethylmanganocene.* Journal of the American Chemical Society, 1974. **96**(25): p. 7833-7835.
10. Hayami, S., et al., *Iron(III) Spin-Crossover Compounds with a Wide Apparent Thermal Hysteresis around Room Temperature.* Journal of the American Chemical Society, 2001. **123**(47): p. 11644-11650.
11. Kennedy, B.J., et al., *Variable-temperature magnetic, spectral, and x-ray crystallographic studies of "spin-crossover" iron(III) Schiff-base-Lewis-*

base adducts. Influence of noncoordinated anions on spin-state interconversion dynamics in [Fe(salen)(imd)2]Y species (Y = ClO4-, BF4-, PF6-, BPh4-; imd = imidazole). Inorganic Chemistry, 1987. **26**(4): p. 483-495.

12. Chuang, Y.-C., et al., *New Iron(II) Spin Crossover Coordination Polymers [Fe(μ-atrz)3]X2·2H2O (X = ClO4¯, BF4¯) and [Fe(μ-atrz)(μ-pyz)(NCS)2]·4H2O with an Interesting Solvent Effect.* Inorganic Chemistry, 2012. **51**(8): p. 4663-4671.
13. Grunert, C.M., et al., *Structure and Physical Properties of [μ-Tris(1,4-bis(tetrazol-1-yl)butane-N4,N4')iron(II)] Bis(hexafluorophosphate), a New Fe(II) Spin-Crossover Compound with a Three-Dimensional Threefold Interlocked Crystal Lattice.* Inorganic Chemistry, 2004. **43**(1): p. 155-165.
14. Brooker, S., et al., *[CoII2L(NCS)2(SCN)2]: The First Cobalt Complex to Exhibit Both Exchange Coupling and Spin Crossover Effects.* Angewandte Chemie International Edition, 1999. **38**(3): p. 408-410.
15. Hayami, S., et al., *Dynamic structural conversion in a spin-crossover cobalt(ii) compound with long alkyl chains.* Chemical Communications, 2008(48): p. 6510-6512.
16. Klaeui, W., W. Eberspach, and P. Guetlich, *Spin-crossover cobalt(III) complexes: steric and electronic control of spin state.* Inorganic Chemistry, 1987. **26**(24): p. 3977-3982.
17. Guetlich, P., B.R. McGarvey, and W. Klaeui, *Temperature-dependent 5T2(Oh) .dblharw. 1A1(Oh) spin equilibrium in a six-coordinate cobalt(III) complex. Investigation by phosphorus-31 NMR in solution.* Inorganic Chemistry, 1980. **19**(12): p. 3704-3706.
18. Bethe, H.A., *Splitting of Terms in Crystals.* Annals of Physics, 1929. **3**: p. 133-206.
19. Van Vleck, J.H., *Theory of the Variations in Paramagnetic Anisotropy Among Different Salts of the Iron Group.* Physical Review, 1932. **41**(2): p. 208-215.
20. Hauser, A., *Ligand Field Theoretical Considerations*, in *Spin Crossover in Transition Metal Compounds I*, P. Gütlich, Goodwin, Harold A., Editor 2004, Springer Berlin Heidelberg. p. 49-58.
21. Rayner-Canham, G. and T. Overton, *Descriptive Inorganic Chemistry*2013: W. H. Freeman.
22. Tanabe, Y. and S. Sugano, *On the Absorption Spectra of Complex Ions. I.* Journal of the Physical Society of Japan, 1954. **9**(5): p. 753-766.
23. Tanabe, Y. and S. Sugano, *On the Absorption Spectra of Complex Ions II.* Journal of the Physical Society of Japan, 1954. **9**(5): p. 766-779.

24. Hoselton, M.A., L.J. Wilson, and R.S. Drago, *Substituent effects on the spin equilibrium observed with hexadentate ligands on iron(II).* Journal of the American Chemical Society, 1975. **97**(7): p. 1722-1729.
25. Mikami-Kido, M. and Y. Saito, *Structure of tris(2-picolylamine)zinc(II) dichloride-ethanol, [Zn ([alpha]-pic)3]Cl2.EtOH; a complex related to an FeII spin crossover complex.* Acta Crystallographica Section B, 1982. **38**(2): p. 452-455.
26. Freeman, M.A. and D.A. Young, *Synthesis and structure of three (tricyclohexylphosphine)rhodium complexes and their interconversion with carbon monoxide and hydrogen.* Inorganic Chemistry, 1986. **25**(10): p. 1556-1560.
27. Gütlich, P., A. Hauser, and H. Spiering, *Thermal and Optical Switching of Iron(II) Complexes.* Angewandte Chemie International Edition in English, 1994. **33**(20): p. 2024-2054.
28. Stoufer, R.C., D.H. Busch, and W.B. Hadley, *UNUSUAL MAGNETIC PROPERTIES OF SOME SIX-COÖRDINATE COBALT(II) COMPLEXES1 —ELECTRONIC ISOMERS.* Journal of the American Chemical Society, 1961. **83**(17): p. 3732-3734.
29. Sams, J.R., J.C. Scott, and T.B. Tsin, *Tris [2-(2'-pyridyl)benzimidazole]iron(II) complexes. Some new examples of 5T2 — 1A1 spin equilibria.* Chemical Physics Letters, 1973. **18**(3): p. 451-453.
30. Baker, W.A. and H.M. Bobonich, *Magnetic Properties of Some High-Spin Complexes of Iron(II).* Inorganic Chemistry, 1964. **3**(8): p. 1184-1188.
31. Koenig, E. and K. Madeja, *5T2-1A1 Equilibriums in some iron(II)-bis(1,10-phenanthroline) complexes.* Inorganic Chemistry, 1967. **6**(1): p. 48-55.
32. König, E. and G. Ritter, *Hysteresis effects at a cooperative high-spin (5T2) ⇌ low-spin (1A1) transition in dithiocyanatobis (4, 7-dimethyl-1, 10-phenanthroline) iron (II).* Solid State Communications, 1976. **18**(3): p. 279-282.
33. *Topics in Current Chemistry*, ed. P. Gütlich, Goodwin, Harold A. Vol. 233. 2004: Springer.
34. Létard, J.-F., et al., *Wide Thermal Hysteresis for the Mononuclear Spin-Crossover Compound cis-Bis(thiocyanato)bis[N-(2'-pyridylmethylene)-4-(phenylethynyl)anilino]iron(II).* Journal of the American Chemical Society, 1997. **119**(44): p. 10861-10862.
35. Weber, B., et al., *Control of Exchange Interactions in Trinuclear Complexes Based on Orthogonal Magnetic Orbitals.* European Journal of Inorganic Chemistry, 2009. **2009**(36): p. 5535-5540.

36. Weber, B., W. Bauer, and J. Obel, *An iron(II) spin-crossover complex with a 70 K wide thermal hysteresis loop.* Angewandte Chemie - International Edition, 2008. **47**(52): p. 10098-10101.
37. Kahn, O. and E. Codjovi, *Iron(II)-1,2,4-Triazole Spin Transition Molecular Materials.* Philosophical Transactions of the Royal Society of London. Series A: Mathematical, Physical and Engineering Sciences, 1996. **354**(1706): p. 359-379.
38. Zelentsov, V.V., Soviet Scientific Reviews Series, Section B, 1981. **81**: p. 541.
39. Romstedt, H., A. Hauser, and H. Spiering, *High-spin → low-spin relaxation in the two-step spincrossover compound [Fe(pic)3]Cl2EtOH (pic = 2-picolylamine).* Journal of Physics and Chemistry of Solids, 1998. **59**(2): p. 265-275.
40. Real, J.A., et al., *Two-step spin crossover in the new dinuclear compound [Fe(bt)(NCS)2]2bpym, with bt = 2,2'-bi-2-thiazoline and bpym = 2,2'-bipyrimidine: experimental investigation and theoretical approach.* Journal of the American Chemical Society, 1992. **114**(12): p. 4650-4658.
41. Gütlich, P., *Spin crossover in Iron (II) complexes*, in *Metal Complexes*1981, Springer. p. 83-195.
42. Lindoy, L.F. and S.E. Livingstone, *Complexes of iron(II),cobalt(II) and nickel(II) with α-diimines and related bidentate ligands.* Coordination Chemistry Reviews, 1967. **2**(2): p. 173-193.
43. Goodwin, P.G.a.H.A., *Spin Crossover—An overall perspective*, in *Spin Crossover in Transition Metal Compounds I*, P.G.a.H.A. Goodwin, Editor, Springer. p. 1-47.
44. Moliner, N., et al., *Mass Effect on the Equienergetic High-Spin/Low-Spin States of Spin-Crossover in 4,4'-Bipyridine-Bridged Iron(II) Polymeric Compounds: Synthesis, Structure, and Magnetic, Mössbauer, and Theoretical Studies.* Inorganic Chemistry, 2002. **41**(26): p. 6997-7005.
45. Gütlich, P. Structural bonding. Vol. 44. 1981. 83.
46. Sorai, M. and S. Seki, *Phonon coupled cooperative low-spin 1A1high-spin 5T2 transition in [Fe(phen)2(NCS)2] and [Fe(phen)2(NCSe)2] crystals.* Journal of Physics and Chemistry of Solids, 1974. **35**(4): p. 555-570.
47. Sorai, M. and S. Seki, *Magnetic Heat Capacity Due to Cooperative Low-Spin 1A\(_{1}{\rightleftharpoons}\)High-Spin 5T2 Transition in Fe(phen)2(NCS)2 Crystal.* Journal of the Physical Society of Japan, 1972. **33**(2): p. 575-575.

48. Slichter, C.P. and H.G. Drickamer, *Pressure-Induced Electronic Changes in Compounds of Iron.* The Journal of Chemical Physics, 1972. **56**(5): p. 2142-2160.
49. Carlin, R.L., *Magnetochemistry*1986: Springer-Verlag.
50. Sorai, M., J. Ensling, and P. Gütlich, *Mössbauer effect study on low-spin 1A1 ⇌ high-spin 5T2 transition in tris(2-picolylamine) iron chloride I. Dilution effect in [FexZn1-x(2-pic)3]Ch2·C2H5OH.* Chemical Physics, 1976. **18**(1): p. 199-209.
51. *Mössbauer Spectroscopy*, ed. U. Gonser1975: Springer.
52. Biswas, S., et al., *Thermal spin-crossover in the [M3Zn6Cl 6L12] (M = Zn, FeII; L = 5,6-dimethoxy-1,2,3- benzotriazolate) system: Structural, electrochemical, Mössbauer, and UV-Vis spectroscopic studies.* Dalton Transactions, 2010. **39**(41): p. 9851-9859.
53. Evans, D.F., *The determination of the paramagnetic susceptibility of substances in solution by nuclear magnetic resonance.* Journal of the Chemical Society (Resumed), 1959(0): p. 2003-2005.
54. Weber, B. and F.A. Walker, *Solution NMR Studies of Iron(II) Spin-Crossover Complexes.* Inorganic Chemistry, 2007. **46**(16): p. 6794-6803.
55. Weber, B., et al., *Stepwise Spin Transition in a Mononuclear Iron(II) Complex with Unusually Wide Plateau.* European Journal of Inorganic Chemistry, 2008. **2008**(10): p. 1589-1598.
56. Gallois, B., et al., *Structural changes associated with the spin transition in bis(isothiocyanato)bis(1,10-phenanthroline)iron: a single-crystal x-ray investigation.* Inorganic Chemistry, 1990. **29**(6): p. 1152-1158.
57. Neville, S.M., et al., *Guest Tunable Structure and Spin Crossover Properties in a Nanoporous Coordination Framework Material.* Journal of the American Chemical Society, 2009. **131**(34): p. 12106-12108.
58. Koenig, E., et al., *The discontinuous high-spin (5T2) .dblharw. low-spin (1A1) transition in solid bis(1,10-phenanthroline-2-carbaldehyde phenylhydrazone)iron(II) bis(tetrafluoroborate): hysteresis effects, concurrent crystallographic phase change, entropy of the transition, and effect of pressure.* Inorganic Chemistry, 1984. **23**(13): p. 1896-1902.
59. Kulshreshtha, S.K., et al., *The nature of spin-state transitions in Fe(II) complexes.* Chemical Physics Letters, 1984. **110**(2): p. 201-204.
60. Kulshreshtha, S.K., R. Sasikala, and E. König, *Calorimetric investigations of the low-spin (1A1) ⇄ high-spin (5T2) transition in solid dithiocyanatobis(2,2'-BI-2-thiazoline)ir.* Chemical Physics Letters, 1986. **123**(3): p. 215-217.

61. Kulshreshtha, S.K. and R.M. Iyer, *A calorimetric study of low-spin ⇐ high-spin transitions in bis(1,10-phenanthroline-2-carbaldehyde phenyl hydrazone)iron(II) diperchlorate and ditetrafluoroborate.* Chemical Physics Letters, 1987. **134**(3): p. 239-244.
62. McGravey, J.J. and I. Lawthers, *Photochemically-induced perturbation of the 1A [right left harpoons]5T equilibrium in Fe11 complexes by pulsed laser irradiation in the metal-to-ligand charge-transfer absorption band.* Journal of the Chemical Society, Chemical Communications, 1982(16): p. 906-907.
63. Decurtins, S., et al., *Light-induced excited spin state trapping in a transition-metal complex: The hexa-1-propyltetrazole-iron (II) tetrafluoroborate spin-crossover system.* Chemical Physics Letters, 1984. **105**(1): p. 1-4.
64. Decurtins, S., et al., *Light-induced excited-spin-state trapping in iron(II) spin-crossover systems. Optical spectroscopic and magnetic susceptibility study.* Inorganic Chemistry, 1985. **24**(14): p. 2174-2178.
65. Hauser, A., *Intersystem crossing in the [Fe(ptz)6](BF4)2 spin crossover system (ptz=1-propyltetrazole).* The Journal of Chemical Physics, 1991. **94**(4): p. 2741-2748.
66. Hauser, A., *Reversibility of light-induced excited spin state trapping in the Fe(ptz)6(BF4)2, and the Zn1−xFex(ptz)6(BF4)2 spin-crossover systems.* Chemical Physics Letters, 1986. **124**(6): p. 543-548.
67. Ewald, A.H., et al., *Anomalous Behaviour at the 6A1-2T2 Crossover in Iron (III) Complexes.* Proceedings of the Royal Society of London. Series A. Mathematical and Physical Sciences, 1964. **280**(1381): p. 235-257.
68. Köhler, C.P., et al., *Nature of the phase transition in spin crossover compounds.* Journal of Physics and Chemistry of Solids, 1990. **51**(3): p. 239-247.
69. Ewald, A.H., et al., *Electronic equilibrium between the 6A1 and 2T2 states in iron(III) dithio chelates.* Inorganic Chemistry, 1969. **8**(9): p. 1837-1846.
70. Usha, S., R. Srinivasan, and C.N.R. Rao, *High-pressure magnetic susceptibility studies of spin-state transition in Fe(II) complexes.* Chemical Physics, 1985. **100**(3): p. 447-455.
71. Halcrow, M.A., *The foundation of modern spin-crossover.* Chemical Communications, 2013. **49**(93): p. 10890-10892.
72. Hogg, R. and R.G. Wilkins, *57. Exchange studies of certain chelate compounds of the transitional metals. Part VIII. 2,2[prime or minute],2[double prime]-terpyridine complexes.* Journal of the Chemical Society (Resumed), 1962(0): p. 341-350.

73. Sugiyarto, K. and H. Goodwin, *Cooperative Spin Transitions in Iron(II) Derivatives of 1,2,4-Triazole.* Australian Journal of Chemistry, 1994. **47**(2): p. 263-277.
74. Varnek, V.A. and L.G. Lavrenova, *Mössbauer study of the influence of ligands and anions of the second coordination sphere in Fe(II) complexes with 1,2,4-triazole and 4-amino-1,2,4-triazole on the temperature of the 1A 1⇆5 T 2 spin transitions.* Journal of Structural Chemistry, 1995. **36**(1): p. 104-111.
75. Dîrtu, M.M., et al., *Prediction of the Spin Transition Temperature in FeII One-Dimensional Coordination Polymers: an Anion Based Database.* Inorganic Chemistry, 2009. **48**(16): p. 7838-7852.
76. Real, J.A., et al., *spin-Crossover Behavior in the Fe(tap)2(NCS)2·nCH3CN System (tap = 1,4,5,8-Tetraazaphenanthrene; n = 1, 1/2). Crystal Structures and Magnetic Properties of Both Solvates.* Inorganic Chemistry, 1994. **33**(16): p. 3587-3594.
77. Peng, H., et al., *Re-appearance of cooperativity in ultra-small spin-crossover [Fe(pz){Ni(CN)4}] nanoparticles.* Angewandte Chemie - International Edition, 2014. **53**(41): p. 10894-10898.
78. Kitchen, J.A. and S. Brooker, *Spin crossover in iron(II) complexes of 3,5-di(2-pyridyl)-1,2,4-triazoles and 3,5-di(2-pyridyl)-1,2,4-triazolates.* Coordination Chemistry Reviews, 2008. **252**(18-20): p. 2072-2092.
79. Matouzenko, G.S., et al., *Cooperative Spin Crossover and Order-Disorder Phenomena in a Mononuclear Compound [Fe(DAPP)(abpt)](ClO4)2 [DAPP = [Bis(3-aminopropyl)(2-pyridylmethyl)amine], abpt = 4-Amino-3,5-bis(pyridin-2-yl)-1,2,4-triazole]*. Inorganic Chemistry, 2004. **43**(1): p. 227-236.
80. Cheng, X., et al., *Thermal and light induced spin crossover behavior of a dinuclear Fe(ii) compound.* Dalton Transactions, 2015. **44**(25): p. 11282-11285.
81. Klingele, M.H., et al., *The first X-ray crystal structure determination of a dinuclear complex trapped in the [low spin-high spin] state: [FeII2(PMAT) 2](BF4)4·DMF*. Chemical Communications, 2005(8): p. 987-989.
82. Ksiazek, M., G. Bednarek, and J. Kusz, *The influence of the spin crossover on the crystal structure of the [Fe3(hyetrz)6 (H2O)6](CF3SO3)6 complex compound.* Acta Physica Polonica A, 2016. **130**(4): p. 873-875.
83. Garcia, Y., et al., *Synthesis, crystal structure, magnetic properties and 57Fe Mossbauer spectroscopy of the new trinuclear [Fe3(4-(2'-hydroxyethyl)-1,2,4- triazole)6(H2O)6](CF3SO3)6 spin crossover compound.* European Journal of Inorganic Chemistry, 2000(7): p. 1531-1538.

84. Roubeau, O., *Triazole-based one-dimensional spin-crossover coordination polymers*. Chemistry - A European Journal, 2012. **18**(48): p. 15230-15244.
85. Liu, Y., et al., *Synthesis, Structure, and Magnetic Characterization of a Series of Iron(II) Coordination Frameworks with 2, 6-Bis(1, 2,4-triazole-4-yl)pyridine.* Zeitschrift fur Anorganische und Allgemeine Chemie, 2015. **641**(14): p. 2422-2428.
86. Naik, A.D., et al., *Coordination polymers and metal organic frameworks derived from 1,2,4-triazole amino acid linkers.* Polymers, 2011. **3**(4): p. 1750-1775.
87. Haasnoot, J.G., *Mononuclear, oligonuclear and polynuclear metal coordination compounds with 1,2,4-triazole derivatives as ligands.* Coordination Chemistry Reviews, 2000. **200**–**202**: p. 131-185.
88. J. G. Haasnoot, G.V., W. L. Groeneveld, Z. Naturforsch. B, 1977. **32**: p. 421.
89. Michalowicz, A., et al., *EXAFS and X-ray powder diffraction studies of the spin transition molecular materials [Fe(Htrz)2(trz)](BF4) and [Fe(Htrz)3](BF4)2.H2O (Htrz = 1,2,4-4H-triazole; trz = 1,2,4-triazolato).* Chemistry of Materials, 1995. **7**(10): p. 1833-1842.
90. Michalowicz, A., J. Moscovici, and O. Kahn, *Polymerie Fe(II) Spin Cross Over Compounds: XAS Structural Results.* J. Phys. IV France, 1997. **7**(C2): p. C2-633-C2-635.
91. Kahn, O. and C.J. Martinez, *Spin-transition polymers: From molecular materials toward memory devices.* Science, 1998. **279**(5347): p. 44-48.
92. Halcrow, M.A., *Spin-Crossover Materials: Properties and Applications*. Spin-Crossover Materials: Properties and Applications2013.
93. Rotaru, A., et al., *Nano-electromanipulation of spin crossover nanorods: Towards switchable nanoelectronic devices.* Advanced Materials, 2013. **25**(12): p. 1745-1749.
94. Galet, A., et al., *Tunable bistability in a three-dimensional spin-crossover sensory- and memory-functional material.* Advanced Materials, 2005. **17**(24): p. 2949-2953.
95. Ni, Z. and M.P. Shores, *Magnetic observation of anion binding in iron coordination complexes: Toward spin-switching chemosensors.* Journal of the American Chemical Society, 2009. **131**(1): p. 32-33.
96. Qiu, D., et al., *Spin crossover-graphene nanocomposites: facile syntheses, characterization, and magnetic properties.* RSC Advances, 2014. **4**(59): p. 31323-31327.
97. Vos, G., et al., *Unique high-spin-low-spin transition of the central ion in a linear, trinuclear iron(II) triazole compound.* Journal of the American Chemical Society, 1983. **105**(6): p. 1682-1683.

98. Ebdon, J.R., *Introduction to polymers (second edition) R. J. Young and P. A. Lovell Chapman and Hall, London, 1991. pp. 443, price £16.95. ISBN 0-412-30640-9 (PB); ISBN 0–412–30630–1 (HB).* Polymer International, 1992. **27**(2): p. 207-208.
99. *Patents for inventions*, in *UK Patent office*1857. p. 255.
100. Bruice, P.Y., *Organic Chemistry*2014: Pearson Education, Limited.
101. Shirakawa, H., et al., *Synthesis of electrically conducting organic polymers: halogen derivatives of polyacetylene, (CH).* Journal of the Chemical Society, Chemical Communications, 1977(16): p. 578-580.
102. Chiang, C.K., et al., *Electrical Conductivity in Doped Polyacetylene.* Physical Review Letters, 1977. **39**(17): p. 1098-1101.
103. Janata, J. and M. Josowicz, *Conducting polymers in electronic chemical sensors.* Nature Materials, 2003. **2**(1): p. 19-24.
104. Gerard, M., A. Chaubey, and B.D. Malhotra, *Application of conducting polymers to biosensors.* Biosensors and Bioelectronics, 2002. **17**(5): p. 345-359.
105. Talo, A., et al., *Polyaniline/epoxy coatings with good anti-corrosion properties.* Synthetic Metals, 1997. **85**(1): p. 1333-1334.
106. Riaz, U., C. Nwaoha, and S.M. Ashraf, *Recent advances in corrosion protective composite coatings based on conducting polymers and natural resource derived polymers.* Progress in Organic Coatings, 2014. **77**(4): p. 743-756.
107. Kim, J.Y., et al., *Efficient tandem polymer solar cells fabricated by all-solution processing.* Science, 2007. **317**(5835): p. 222-225.
108. Na, S.-I., et al., *Efficient and Flexible ITO-Free Organic Solar Cells Using Highly Conductive Polymer Anodes.* Advanced Materials, 2008. **20**(21): p. 4061-4067.
109. Tang, C.W. and S.A. VanSlyke, *Organic electroluminescent diodes.* Applied Physics Letters, 1987. **51**(12): p. 913-915.
110. Burroughes, J.H., et al., *Light-emitting diodes based on conjugated polymers.* Nature, 1990. **347**(6293): p. 539-541.
111. Lu, X., et al., *One-dimensional conducting polymer nanocomposites: Synthesis, properties and applications.* Progress in Polymer Science, 2011. **36**(5): p. 671-712.
112. Stejskal, J., I. Sapurina, and M. Trchová, *Polyaniline nanostructures and the role of aniline oligomers in their formation.* Progress in Polymer Science, 2010. **35**(12): p. 1420-1481.

113. Du, Y., et al., *Research progress on polymer–inorganic thermoelectric nanocomposite materials.* Progress in Polymer Science, 2012. **37**(6): p. 820-841.
114. Wang, G.-F., et al., *Modification of Conductive Polymer for Polymeric Anodes of Flexible Organic Light-Emitting Diodes.* Nanoscale Research Letters, 2009. **4**(7): p. 613-617.
115. Dierckx, W., et al., *Poly(3-alkylthiophene) nanofibers for optoelectronic devices.* Journal of Materials Chemistry C, 2014. **2**(29): p. 5730-5746.
116. Eom, S.H., et al., *Polymer solar cells based on inkjet-printed PEDOT:PSS layer.* Organic Electronics, 2009. **10**(3): p. 536-542.
117. Ma, X., et al., *Improved performances of solid tantalum electrolytic capacitors using EG-treated PEDOT:PSS conducting polymer as cathode electrodes.* Chemistry Letters, 2016. **45**(7): p. 717-719.
118. Kang, H., et al., *Polymer-metal hybrid transparent electrodes for flexible electronics.* Nature Communications, 2015. **6**: p. 6503.
119. Kirchmeyer, S. and K. Reuter, *Scientific importance, properties and growing applications of poly(3,4-ethylenedioxythiophene).* Journal of Materials Chemistry, 2005. **15**(21): p. 2077-2088.
120. Kaloni, T.P., G. Schreckenbach, and M.S. Freund, *Band gap modulation in polythiophene and polypyrrole-based systems.* Scientific Reports, 2016. **6**: p. 36554.

CHAPTER 2

Iron (II) Trinuclear Complexes with 1,2,4-Triazole Sulfonated Derivatives. A Comparative Study

UNIVERSITAT ROVIRA I VIRGILI
AVANCES EN SISTEMAS INTERACTIVOS PARA PERSONAS CON PARÁLISIS CEREBRAL
María del Pilar Maldonado Illescas

2.1. Introduction

Iron (II) complexes displaying spin crossover (SCO) behavior, a phenomenon in which the spin state of the metal center switches between low-spin (LS) and high-spin (HS) states under external stimuli, are a paradigmatic example of switchable molecular materials [1-3]. The spin transition from diamagnetic $S = 0$ to paramagnetic $S = 2$ in octahedral Iron (II) provokes a dramatic change also in color (from pink/red to white/yellow) and size (increment of 10-15% in the metal to ligand bonding distances). Besides, if this transition occurs with hysteresis a memory effect is conferred. Recently there is a renaissance of SCO materials in molecular magnetism [4-7] because, in contrast with other bistable species such as single molecule magnets [8, 9], SCO may occur at room temperature. Thus, SCO appears especially suited for applications as stimuli-responsive molecular switches for multifunctional materials, memories, electrical circuits or display devices [10-15]. Most reported complexes with hysteretic SCO are mononuclear or polymeric Iron (II) compounds, typically with neutral or cationic overall charge. During this PhD work we have focused in the search for anionic SCO complexes to increase their processing capabilities when incorporated into hybrid materials. With this in mind, we prepared sulfonated 1,2,4-triazole derivatives as building blocks with different counteranion result the possibility of tuning the magnetic behavior and being essential in the development of new devices [16, 17].

2.2. Experimental

2.2.1. Synthesis

Reagents were obtained from commercial sources and used without further purification. Yields were calculated from stoichiometric reaction. Caution! Perchlorate salts of compounds containing organic ligands are potentially explosive. Only small quantities of these compounds should be prepared and handled behind suitable protective elements.

N,N-dimethylformamide azine: a) Thionyl Chloride (28.6 mL, 0.4 mol) was added dropwise to N,N-dimethylformamide (150 mL) at 5 ºC. After 24 hours, Hydrazine (5 mL, 0.1 mol) were introduced cautious in the round bottom flask at 5 ºC. After 48 hours, the solution was filtered, washed with N,N-dimethylformamide and dried with dichloromethane and diethyl ether obtaining the N,N-dimethylformamide azine dihydrochloride (20 g). **IR** (ATR, cm^{-1}): 2940w, 2580s, 1696vs, 1504m, 1296s, 1130m, 1051m, 761s, 717m, 487s, 438s. **1H-NMR** (300 MHz, D_2O, 298 K): δ = 8.39 (s, 2 H), 3.28 (s, 12 H). b) N,N-dimethylformamide azine dihydrochloride (20 g) in water (100 mL) was treated with Na_2CO_3 (9.8 g, 0.09 mol) in water (100 mL). The solution was continuously extracted with diethyl ether during two days. The extract was evaporated under vacuum and dried in air, obtaining the desired product, N,N-dimethylformamide azine (12 g). **IR** (ATR, cm^{-1}): 2920w, 1618vs, 1435m, 1381s, 1333m, 1251m, 1101s, 962w, 735m. **1H-NMR** (300

MHz, D_2O, 298 K): δ = 7.73 (s, 2 H), 2.85 (s, 12 H).

2-aminoethane-1,1-disulfonic acid: Acrylic acid (6.85 mL, 0.1 mmol) and acetonitrile were mixed into a 500 mL tri-neck round bottom flask and the resulting mixture was cooled to -4°C (ice-salt bath). 40 mL of fuming sulfuric acid (25% SO_3) was added dropwise over 70 min; the resulting reaction mixture turned yellow and was stirred at room temperature for 30 minutes. After that, this mixture was heated to reflux for 30 min, and left at room temperature overnight. After cooling at 4°C, water (85 mL) was added cautiously and the mixture was heated to reflux for 24 hours. The solution were rested and 2-aminoethane-1,1-disulfonic acid crystallized, recovered by filtration and dried with diethyl ether. **IR** (ATR, cm^{-1}): 3437s, 2945s, 1630w, 1590m, 1506m, 1194vs, 1068m, 1016s, 897m, 814m, 731m, 595m, 511m. **1H-NMR** (300 MHz, D_2O, 298 K): δ = 4.43 (t, 1H), 3.72 (d, 2H).

Dimethyl-ammonium 4-(1,2,4-triazol-4-yl)ethanedisulfonate (trz) ($(Me_2NH_2)_2L$): N,N-dimethylformamide azine (3.0 g, 21.0 mmol) and 2-aminoethane-1,1-disulfonic acid (1.44 g, 7.0 mmol) were introduced in a round-bottomed flask with 15 mL of water, and the pH was adjusted below 6.0 with HCl (suitable pH range between 3 and 6). The solution was heated at 92ºC overnight with stirring. Then the solvent was removed under vacuum, obtaining a yellowish oil. The addition of ethanol made the solution to become cloudy and a precipitate was observed after keeping the reaction mixture a few hours in the fridge. The product was removed by filtration as a white solid, washed with ethanol and diethyl ether and dried in air. Yield:

1.70 g (70 %). **Anal.** Calcd $C_8H_{21}N_5O_6S_2 \cdot H_2O$ (365.42): C 26.30, H 6.34, N 19.17, S 17.55. Found C 26.4, H 6.0, N 19.6, S 17.5. **IR** (ATR, cm^{-1}): 3112 s, 1619m, 1591m, 1543m, 1460s, 1234s, 1189vs, 1059s, 1016s, 837m, 590m. **1H NMR** (300 MHz, D_2O, 298 K): δ = 8.59 (s, 2 H), 4.86 (d, J = 6 Hz, 2 H), 4.51 (t, J = 6 Hz, 1 H), 2.73 (s, 12 H). **13C NMR** (300 MHz, D_2O, 298 K): δ =144.78 (2C-trz ring), 74.50 (1C-CH), 43.88 (1C-CH_2), 34.50 (2C-$(CH_3)_2NH^{+2}$).

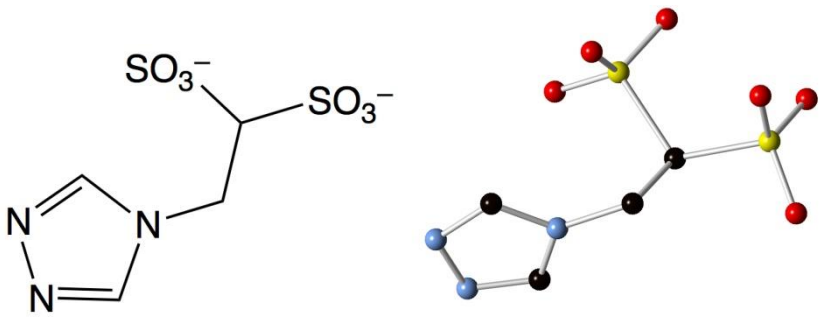

Figure 2.1. Scheme and molecular structure of the ligand L^{2-}

$(Me_2NH_2)_6[Fe_3(L)_6(H_2O)_6]\cdot 6H_2O$ (1): $Fe(ClO_4)_2 \cdot 6H_2O$ (0.089 g, 0.350 mmol) and $(Me_2NH_2)_2L$ (0.305 g, 0.875 mmol), both dissolved in water, were mixed (total volume ca. 5 mL), leading to a pale pink solution. A small amount of ascorbic acid was added to the reaction mixture to avoid air oxidation of the Iron (II) cations. The additions of ethanol (ca. 15 mL) lead to the precipitation of a pink solid. This suspension was centrifuged and the supernatant liquid was decanted. Then 10 mL of ethanol were added and the process was repeated twice. Finally, the pink solid was filtrated, washed with diethyl ether and dried in air. Yield: 0.165 g (65%). **Anal**. Calcd $C_{36}H_{102}Fe_3N_{24}O_{48}S_{12}$ (2191.6): C 19.73, H 4.69, N

María del Pilar Maldonado Illescas

15.34, and S 17.57. Found C 19.4, H 4.3, N 15.5 and S 17.7. **IR**(ATR, cm^{-1}): 3124 s, 2937 w, 2813 w, 1640 w, 1560 m, 1468 m, 1207 vs, 1063 s, 1019 vs, 844 w, 717 m, 638 m, 595 m. Pink crystals suitable for X-ray diffraction were obtained by vapor diffusion, using ethanol as volatile solvent.

$Cs_6[Fe_3(L)_6(H_2O)_6]\cdot 12H_2O$ (2): Compound **1** (0.150 g, 0.072 mmol), CsCl (0.242 g, 1.440 mmol), both dissolved in water, were mixed (total volume ca. 7 mL), leading to a colorless solution. A small quantity of ascorbic acid was also added to prevent Iron(II) oxidation. Slow evaporation of mother liquor lead to the formation of little pink needles suitable for X-ray diffraction. Yield: 0.030 g (16 %). **Anal.** Calcd $C_{24}H_{66}Cs_6N_{18}Fe_3O_{54}S_{12}$ (2820.57): C 10.22, H 2..36, N 8.99 and S 13.64. Found: C 10.37, H 2.2, N 8.95 and S 13.46. **IR** (ATR, cm^{-1}): 3449 s, 3104 s, 2940 m, 1651 m, 1556 m, 1408 w, 1201 vs, 1092 w, 1063 s, 1020 s, 847 w, 715 w, 593 m.

2.2.2. Characterization

X-ray powder diffraction

Figure 2.2 summarized the X-ray powder diffraction patterns of compounds **1** and **2**. Firstly, the diffractogram is completely different confirming that the structure is not the same. Furthermore, crystalline structure are maintained even in used samples (heated to 400 K).

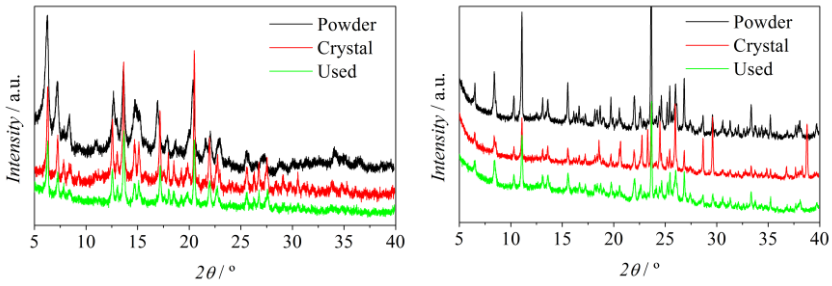

(A) (B)

*Figure 2.2. X-ray powder diffraction patterns of compound **1** (A) and **2** (B) as powder (black) or crystals (red). In green, the PXRD pattern of a crystalline sample after magnetic measurements*

Thermogravimetric Analysis

$(Me_2NH_2)_6[Fe_3(L)_6(H_2O)_6]\cdot 6H_2O$ (1)

A thermogavimetric analysis was performed on the powder sample for **1** in the 25-500 ºC range at 10 ºCmin^{-1} under synthetic air (Figure 2.3.A). The weight loss starts at 30ºC, observing three smooth steps until reaching 290ºC, when the compound completely decomposes. The two first steps correspond to the loss of twelve crystallization water molecules (seven in the first step 5.5 % and five in the second step 3.9 %). The third step starting at 200ºC corresponds with the loss of coordinated water molecules and therefore the decomposition of the compound at 290º C.

Thermogravimetric analysis from 25 to 85º C under air containing 10 % water vapor were carried out to examine the dehydration (hydration dynamics of compound **1**) (Figure 2.3.B). During the first cycle, even in the presence of humid air stream, the

María del Pilar Maldonado Illescas

compound rapidly loses over 4% of the weight. The original weight cannot be recovered showing variations around 1% in successive cycles. It is also important to emphasize that during these cycles there is no hysteresis in the hydration/dehydration process, with the water content depending only on the temperature and not on the branch of heating or cooling branch confirming that hysteresis is not related with the water content between the cooling or heating branches. Moreover, all magnetic measurements were done in perforated capsules to allow proper purging in order to avoid the content of hydration water inside it.

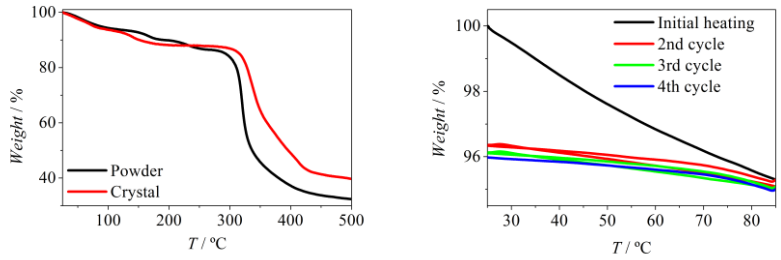

(A) (B)

Figure 2.3. TGA plots for compound 1. (A) Thermogravimetric analysis from 25 to 500º C (10 ºCmin^{-1})(B) Thermogravimetric analysis from 25 to 85º C (1 ºCmin^{-1} scan rate) under air containing 10% water vapor

$Cs_6[Fe_3(L)_6(H_2O)_6]\cdot 12H_2O$ (2)

A thermogavimetric analysis was carried out on the powder and crystalline sample for **2** in the 25-500 ºC range at 10 ºCmin^{-1} under synthetic air (Figure 2.4). The behavior is analogous to the compound **1**; the weight loss starts close to 40ºC, observing two smooth steps until reaching 270 ºC, when the compound starts to

decompose. The two first steps correspond to the loss of eleven crystallization water molecules (nine in the first step 5.52 % and two in the second step 1.04 %).. The loss of coordinated water molecules and the decomposition of the complex starts at 250 ºC.

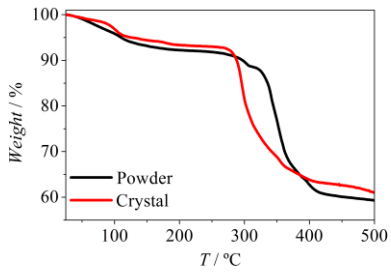

*Figure 2.4. TGA plots for compound **2***

2.3. Results and discussions

2.3.1. Description of the structures

$(Me_2NH_2)_6[Fe_3(L)_6(H_2O)_6]\cdot 6H_2O$ (1)

In this case, **1** precipitates with $(Me_2NH_2)^+$ as the counter cation. The anionic part is the trinuclear polyanion $[Fe_3(\mu\text{-}L)_6(H_2O)_6]^{6-}$ formed by a linear array of octahedral Iron (II) ions (Fe_1-Fe_2-Fe_1) connected by two triple μ-triazole bridges (Figure 2.5). The terminal Fe_1 position completes its N_3O_3 hexacoordination with three H_2O molecules in fac conformation.

María del Pilar Maldonado Illescas

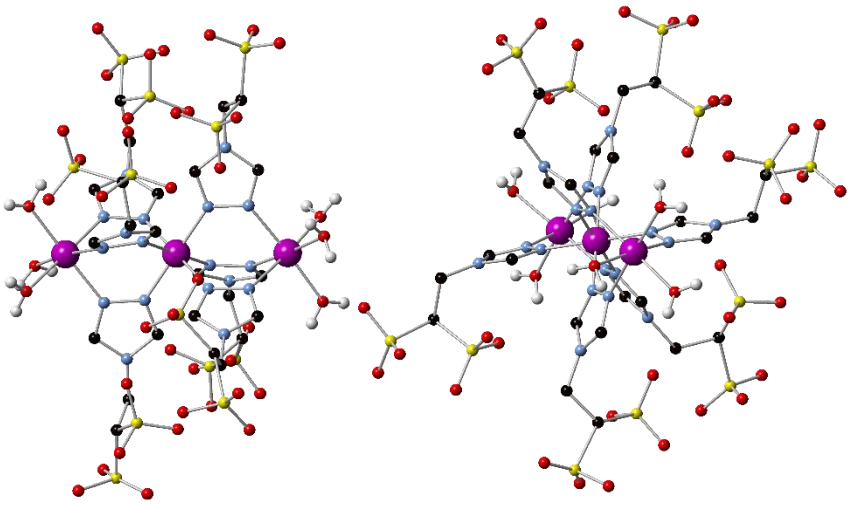

Figure 2.5. Representation and labeling of the molecular core of the $[Fe_3(L)_6(H_2O)_6]^{6-}$ *trimer*

Moreover, the metal to ligand distances at 100 K (Table II.2, in appendix II) indicate HS configuration for Fe_1 (average Fe_1-N = 2.13 Å) and LS configuration for Fe_2 (average Fe_2-N = 1.99 Å). The dangling sulfonate moieties from the ethane groups adopt multiple orientations participating in complex weakly hydrogen bonded network involving the dimethylammonium cations and water molecules. Shortest intermolecular O-O distances are in the 2.6-2.9 Å range (Figure 2.6).

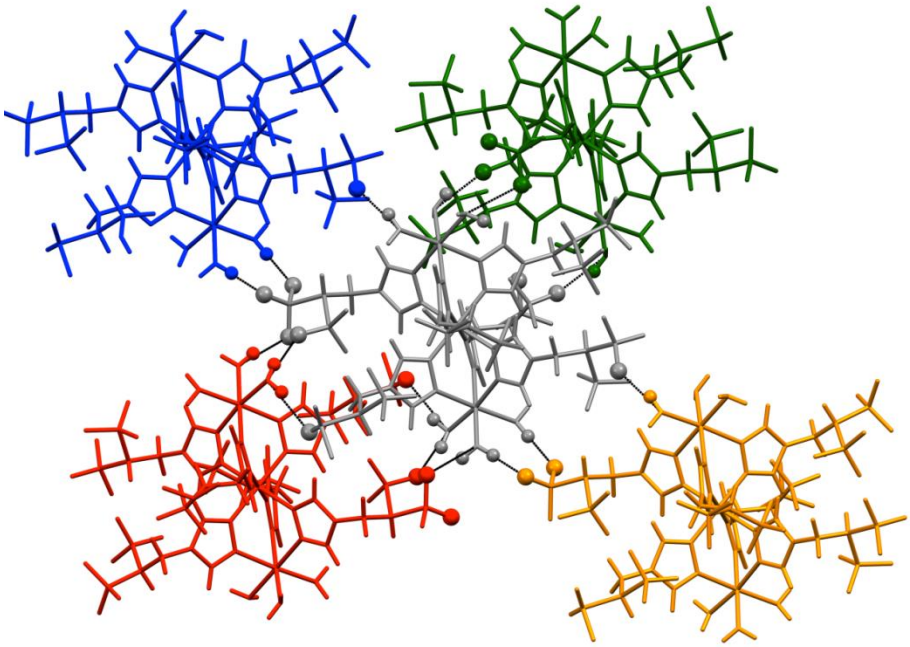

*Figure 2.6. H-bond interactions between trinuclear complexes for **1***

$Cs_6[Fe_3(L)_6(H_2O)_6]\cdot 12H_2O$ (2)

In the case of **2**, the molecular structure of the hexanionic trimer is preserved. At 100 K, it appears in the HS-LS-HS configuration, with Fe-N distance average of 2.1507 Å for the HS centers (terminal Fe atoms) and 1.968 Å for the LS center (central Fe atom). The asymmetric unit contains half a trimer, three Cesium cations, and 6.5 solvent molecules (water) (figure 2.7.A). The trimers are forming segregated anionic layers on the ac plane, with the Cs+ cations separating the layers. The trimers have short interlayer contacts, with hydrogen bonding between the sulfonate groups and the terminal water molecules of adjacent trimers (figure 2.7.B). Each trimer is directly connected to six adjacent

María del Pilar Maldonado Illescas

molecules, in a pseudo-hexagonal packing (figure 2.8). Thus, the connectivity between trimers is stronger in this compound, since only four trimers were surrounded each other in the deimethylammonium salt.

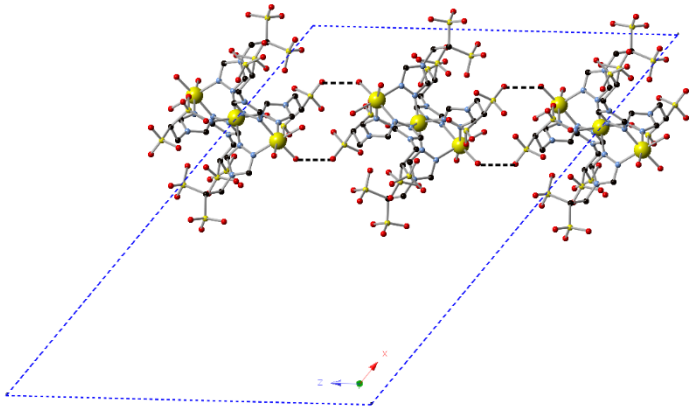

(A)

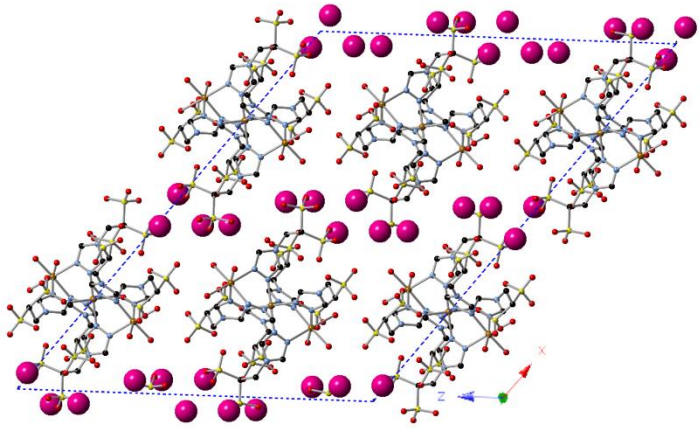

(B)

Figure 2.7. Perspective view of the crystal packing in the unit cell for ***2***

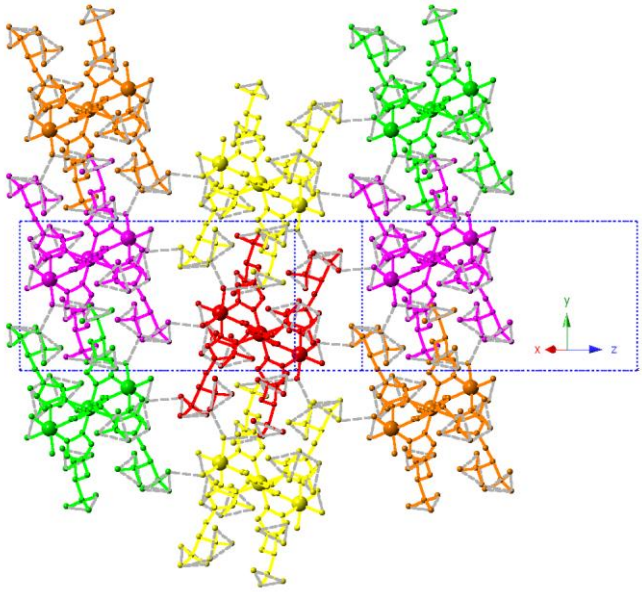

*Figure 2.8. Interactions between trimer complexes for **2***

2.3.2. Magnetic properties

$(Me_2NH_2)_6[Fe_3(L)_6(H_2O)_6]\cdot 6H_2O$ (1)

Magnetic susceptibility measurements were carried out in the 2-300 K range for grained single crystals of **1** (Figure 2.9.A). Above room temperature (Figure 2.9.A, inset), $\chi_m T$ shows a significant increase above 360 K, suggesting a spin transition to the HS-HS-HS state, reaching 7.92 $cm^3mol^{-1}K$ at 400 K. This corresponds approximately to half of the trimers undergoing spin transition. Upon cooling again, the sample goes slowly back to the HS-LS-HS state, with a hysteresis loop of over 65 K. When the sample is maintained at 400 K, $\chi_m T$ keeps increasing in time until it saturates at 8.89 $cm^3mol^{-1}K$ (Figure 2.10.A), corresponding to ≈ 84% completeness.

María del Pilar Maldonado Illescas

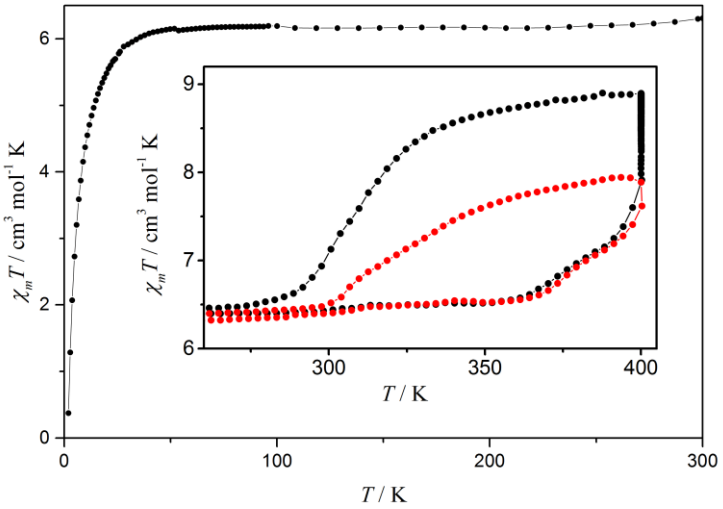

*Figure 2.9. A) χmT vs. T plots for **1** in the 2-300 K range and in the 270-400 K range (inset). Scan rate ≈ 0.1 K min^{-1}. Empty squares show the magnetic behavior when the sample is maintained at 400 K until saturation*

The cooling behavior from magnetic saturation at 400 K (Figure 2.9.A, inset), exhibits a hysteresis loop of 90 K ($T_{1/2}$ (↑) = 400 K, $T_{1/2}$ (↓) = 310 K) with a quasi-static scan rate. This is among the widest thermal hysteresis found for SCO materials [33-37]. It is also reproducible and robust as confirmed by the consistency of successive cycles (Figure 2.10.B).

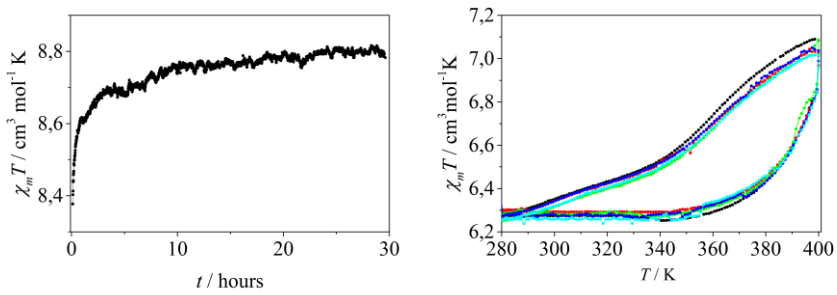

(A) (B)

Figure 2.10. A) Time evolution of the isothermal magnetization for **1** at 400 K at constant field, B) χ_mT vs T plot for **1** for successive cycles at 1 Kmin^{-1} rate. The sample was dehydrated inside the Quantum Design MPMS sample space by purging the system at 400 K before the measurements (red, green, blue and cyan), or the sample was dehydrated ex-situ at 135ºC for 12 hours (black)

Since SCO can be very sensitive to scan rate [38, 39], we studied its effect in the hysteresis cycle (Figure 2.11.A). The heating branch does not change significantly with scan rate. The cooling branch deviates at rates faster than 2 Kmin^{-1}, becoming significantly quenched at scan rates as slow as 5 Kmin^{-1}. This phenomenon, temperature-induced excited spin-state trapping (T_{TIESST}), typically requires very fast cooling (liquid nitrogen immersion) [18, 40-43], but in some rare exceptions [44]. In this case, 57% of the complexes are trapped as HS-HS-HS at a 10 Kmin^{-1} cooling rate. We extracted a characteristic T_{TIESST} = 250 K (Figure 2.11.B) following the method defined by Letard et al. [44] This is the highest T_{TIESST} reported, the previous record being 156 K [45] . At faster heating rates, the HS-HS-HS state is not completely depopulated until reaching room temperature (Figure 2.12).

María del Pilar Maldonado Illescas

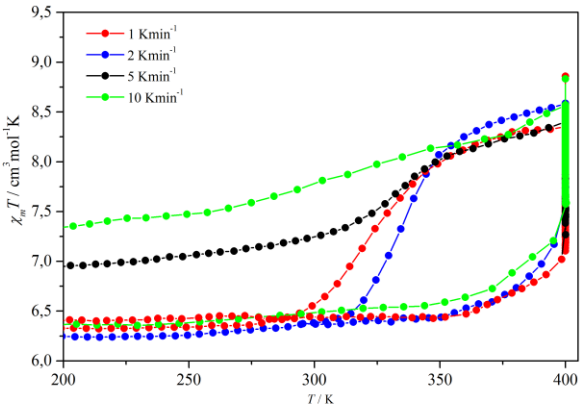

(A)

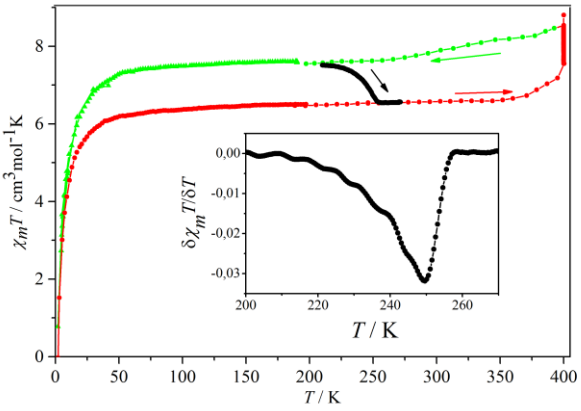

(B)

Figure 2.11. χmT vs. T plots for 1 at: (A) different heating/cooling rates, allowing for saturation at 400 K; (B) heating up to 400 K until saturation (red circles), cooling down at 10 K min–1 rate (blue circles), and warming up again at 0.3 K min–1 (black circles). (inset) δ(χmT)/δT vs T curve for the latter heating branch.

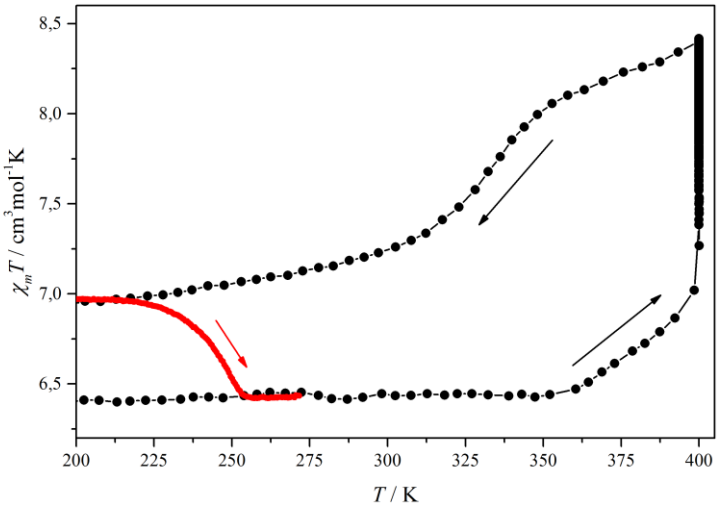

Figure 2.12. χ_mT vs T plot for **1** in a complete cycle starting from the ground HS-LS-HS state. Sample was heated up to 400 K and temperature was maintained until saturation (green stars); the cooling cycle from saturation was performed with a 5 Kmin^{-1} rate (purple diamonds); and the heating cycle was performed with a 1 Kmin^{-1} rate.

Multiple relaxation experiments were performed after heating a polycrystalline sample of **1** at 400 K for 6.5 hours, and trapping the HS-HS-HS state cooling it down to the desired temperature at a scan rate of 10 Kmin^{-1}. The time dependence of the magnetization at this point represents the kinetics of the relaxation process (Figure 2.14). From the relaxation rate at very long times, we can estimate relaxation times as long as 8 hours at 265 K, and over 3 days at 235 K. We assign such striking features to the effect of multiple anionic sulfate groups in the ligands backbone. The

María del Pilar Maldonado Illescas

thermodynamically favored HS → LS process is slowed down due to the need to overcome a large activation energy arising from the electrostatic repulsion between sulfate groups on adjacent triazoles bridges. The smaller size of the LS ground state forces shorter intramolecular distances among them.

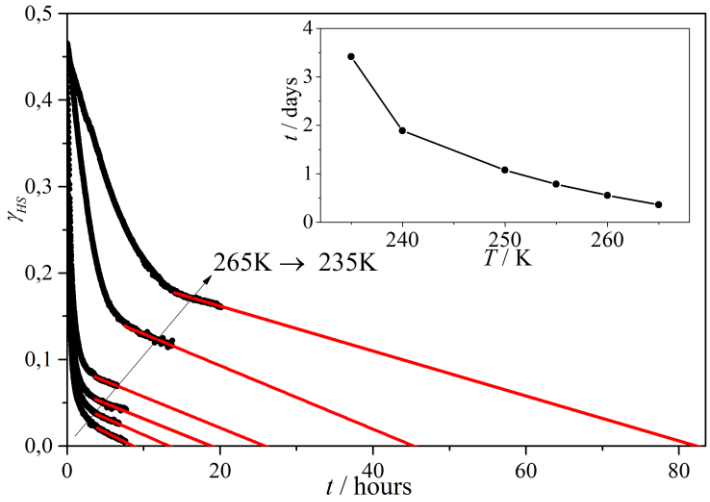

Figure 2.13. Relaxation and estimation of the trapped HS-HS-HS fraction at different temperatures: 265 K, 260 K, 255 K, 250 K, 245 K, 240 K y 235K; after cooling down the sample at 10 Kmin^{-1} from saturation value at 400 K.

In order to normalize the data, we use as variable the fraction of HS-HS-HS complexes, γ_{HS}, estimated from the equation:

$$\gamma_{HS}(t) = \frac{[(\chi T) - (\chi T)_{LS}]}{[(\chi T)_{HS} - (\chi T)_{LS}]} \qquad (2.1)$$

where $(\chi T)_{LS}$ is the magnetic value of the initial HS-LS-HS state, and $(\chi T)_{HS}$ is the maximum magnetic value reached at 400K for the corresponding sample batch.

The kinetics of a relaxation process can be described either with an exponential equation (single or stretched) [46] for non-cooperative systems; or with a sigmoidal curve for cooperative systems in a self-accelerating process [47]. The data obtained for **1** at all temperatures can be fitted, in a first order approximation, to an exponential process, which supports the low cooperativity of the system (Figure 2.11). This low cooperative is in good agreement with the gradual transition observed in the thermal hysteresis cycle. This is also consistent with the weak intermolecular interactions between SCO complexes in the crystal.

Another remarkable observation in the relaxation kinetics deals with completion. In the temperature window we studied, total conversion to the HS-LS-HS ground state is not reached. Thus, at these temperatures, the population of both states reaches a kinetic equilibrium. Indeed, at low temperatures (< 215 K), the decrease in the $\gamma_{HS}(t)$ is negligible and the relaxation curve remains flat in the timeframe of our experiments (< 1% decay after 4 hours) [44]. To take this into account for the fitting model, we include this fraction $\gamma_\infty = \gamma_{\mathrm{HS}}(\mathrm{t} \to \infty)$ in the exponential law, using the equation:

$$\gamma_{\mathrm{HS}}(\mathrm{t}) = \gamma_\infty + (\gamma_{\mathrm{HS}} - \gamma_\infty) \exp(-\mathrm{k}_{\mathrm{HL}} \cdot \mathrm{t}) \qquad (2.2)$$

María del Pilar Maldonado Illescas

where k_{HL}depends on T, and can be expressed as:

$$k_{HL}(T) = k_{HL}^{0} + k_{HL}^{\infty} \exp\left(-\frac{E_a}{k_B T}\right) \qquad (2.3)$$

where $k_{HL}^{0} = k_{HL}(T \to 0)$ and $k_{HL}^{\infty} = k_{HL}(T \to \infty)$.

An Arrhenius fit in the thermally activated region below the T_{TIESST} allows to estimate the activation energy, E_a , and the pre-exponential factor, k_{HL}^{∞}. Above T_{TIESST} the relaxation process becomes temperature independent (Figure 2.14.H). The term k_{HL}^{0} characterizes the relaxation in the quantum tunneling region, and it represents an upper limit at lowest possible temperature [48]. In our case, due to the very high temperature range at which the experiments have been done, this parameter can be neglected. The energy barrier found with this model is E_a = 6370 ± 1442 cm^{-1} and k_{HL}^{∞} = 144*1010 s^{-1}. This represents the largest activation energy found in any SCO material, in good agreement with the T_{TIESST} (250 K). For example, in SCO compounds with T_{TIESST} = 99 K, an activation energy of the 934 cm^{-1} was estimated [49].

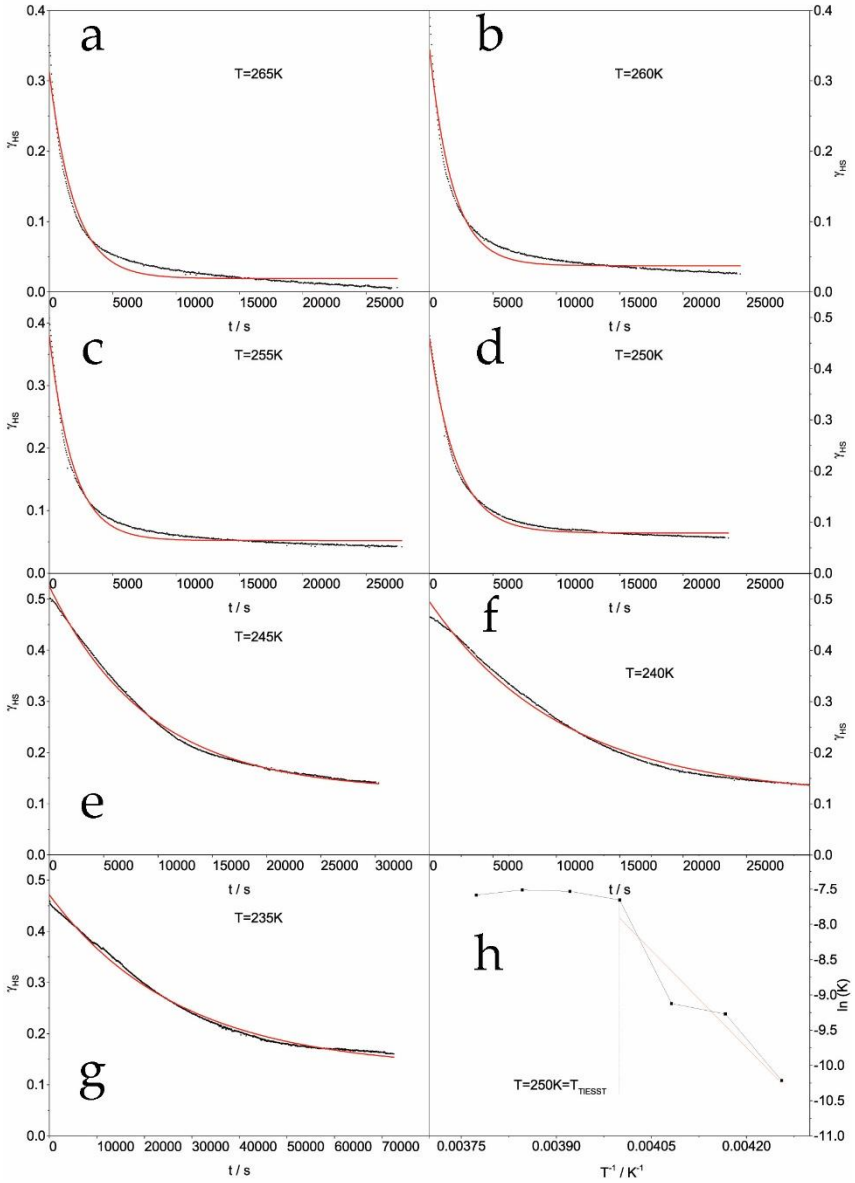

Figure 2.14. Fitting of the relaxation curves for the trapped HS-HS-HS fraction of **1** at different temperatures to exponential or sigmoidal expressions: (a) 265 K , (b) 260 K, (c) 255 K, (d) 250 K, (e) 245 K, (f) 240 K and (g) 235 K. (h) Variation of k_{HL} as a function of T^{-1}

María del Pilar Maldonado Illescas

The opposite transition from the HS-LS-HS to the HS-HS-HS state at high temperatures also shows slow kinetics, although much faster than in the previous case (Figure 2.12).

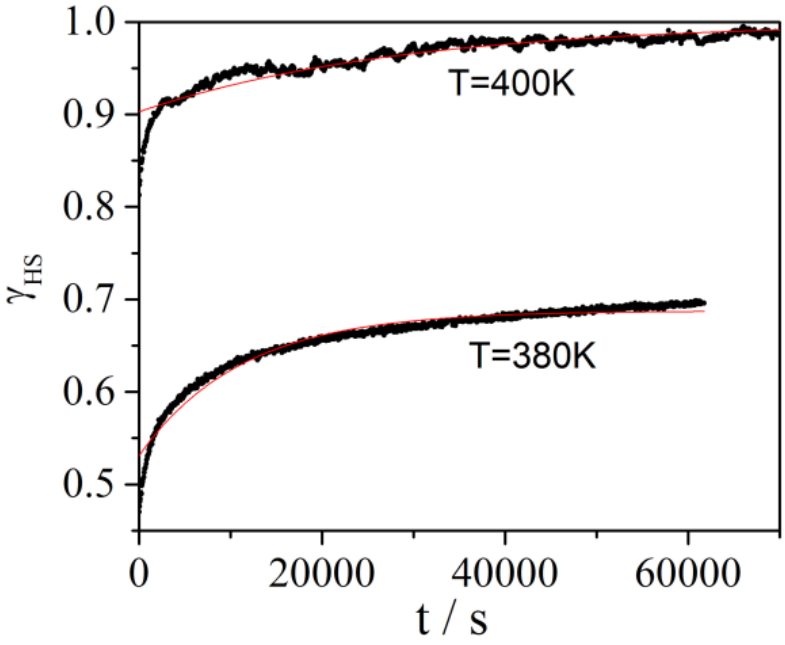

Figure 2.15. Fitting of the HS-LS-HS to HS-HS-HS transition for **1** at different temperatures to exponential expression

An analogous treatment of the data in a thermally activated process using the equation:

$$\gamma_{HS}(t) = \gamma_{\infty} - (\gamma_{\infty} - \gamma_{HS}) \cdot \exp(-k_{LH} \cdot t) \qquad (2.4)$$

where k_{LH} is analogous to k_{HL} (equation 3). The fitting is also better to an exponential expression, although not as satisfactory. This spin transition is much faster, and does not show

such a dependence with scan rate (Figure 2.11.A). The poor fitting also suggests a more complex relaxation process, where several mechanisms could be at play.

Cs6[Fe3(L)6(H2O)6]·12H2O (2)

Magnetic susceptibility measurements were performed between 200-400 K range for crystal of **2** (Figure 2.16).

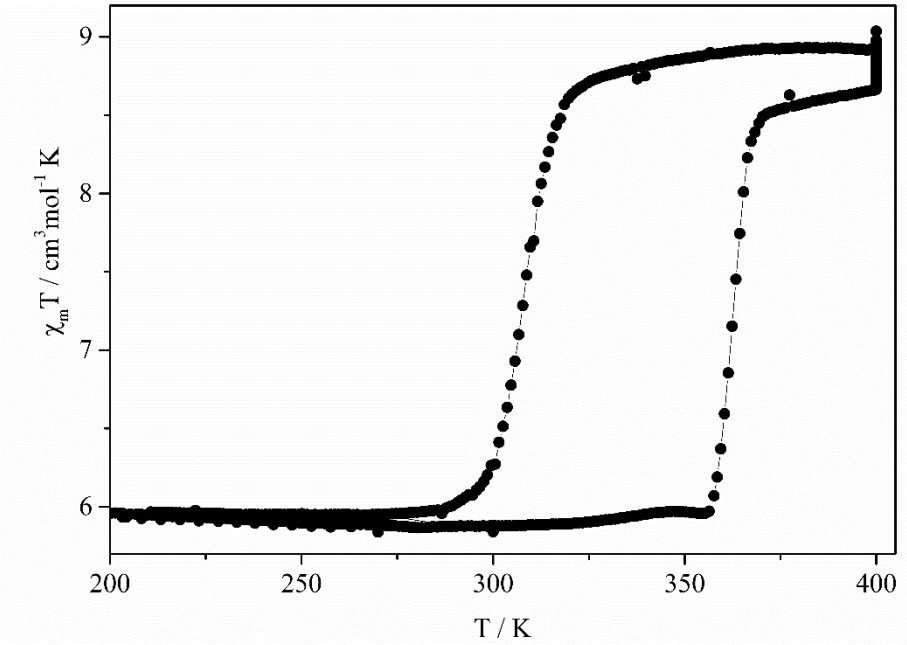

Figure 2.16. $\chi_m T$ vs. T plots for **2** in the 200-400 K range. Scan rate ≈ 0.1Kmin^{-1}

At room temperature, the $\chi_m T$ product is 5.95 cm^{3}mol^{-1}K, corresponding to what is expected for two Irons (II) in HS state and an Iron (II) in LS state (HS-LS-HS configuration). Above room temperature, $\chi_m T$ shows an abrupt increase close to 350 K, corresponding with a HS-HS-HS state, achieving a value of susceptibility of 8.93 cm^{3}mol^{-1}K at 400 K. Once cooling again, the

María del Pilar Maldonado Illescas

sample goes quickly to the initial state (HS-LS-HS state), with a hysteresis loop about 30 K ($T_{1/2}$ (↑) = 350 K, $T_{1/2}$ (↓) = 320 K).

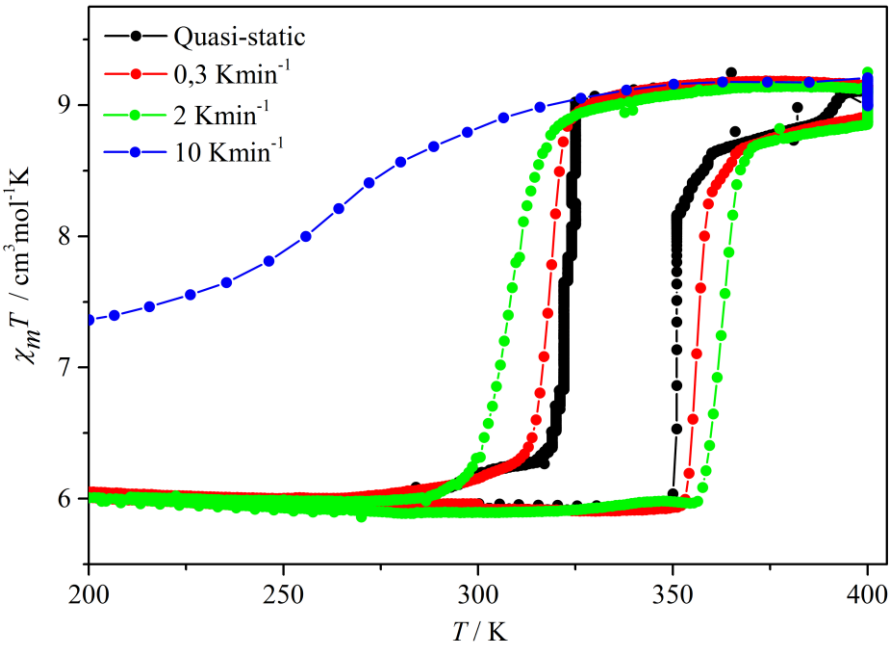

Figure 2.17. χ_mT vs. T plots for 2 at different cooling/heating rates

Figure 2.17 shows the χ_mT versus T curve at different scan rates. It is not significantly sensitive to scan rates and TIESST is harder to achieve. Trapping appears in cooling range only at 10 $Kmin^{-1}$ or faster with about 50 % of the compound remaining in the HS-HS-HS state (Figure 2.18). Under these conditions, the characteristic T_{TIESST} is 241 K (Figure 2.18, inset).

Chapter 2

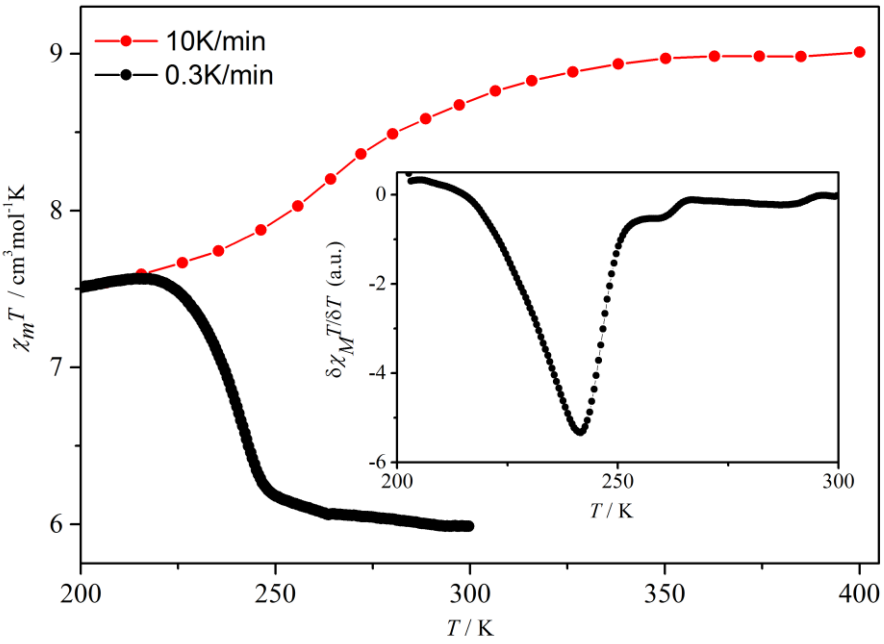

Figure 2.18. χ_mT vs. T plots for **2**. Cooling down at 10 Kmin^{-1} (red), and heating up at 0.3 Kmin-1 (black). Inset $\delta(\chi_m T)/\delta T$ vs T curve for the latter heating branch

María del Pilar Maldonado Illescas

2.3.3. Correlations between Magnetic and Structural Properties

Cation exchange not only lead a change in shape of the spin crossover molecule, but also cause lattice deformations and even crystal structure modifications. In our case, it is notable that a simple cation exchange can be modify the magnetic behavior radically. In table 2.1 are summarized the principal magnetic parameters for **1** and **2** respectively.

	1	**2**
Curve type	Gradual curve	Abrupt curve
ΔT (K)	90	30
$T_{1/2}\uparrow$ (K)	400	350
$T_{1/2}\downarrow$ (K)	310	320
$\chi_m T$ ($cm^3 mol^{-1} K$)	6.37- 8.89	6.09- 8.18

Table 2.1. Magnetic parameter between for **1** and **2**

1 has a gradual hysteresis curve and easily to trap up to 5 $Kmin^{-1}$ while **2** has an abrupt and shorter hysteresis loop. A difference in the magnetic behavior can be due to an increase or decrease of cooperativity principally and in this compound is principally the Fe-Fe distance, being the distance between active irons. For our case, the phenomenon is clearly because in **2**, irons are closer than in **1**, producing a high cooperativity, and therefore giving a gradual curve in **1** and abrupt curve in **2**.

Moreover, the width of the hysteresis loop are affected by the Fe-Fe distance but also the hydrogen bonds that in the structure appears. In 1 it is possible to see the numerous hydrogen bonds that make a wide hysteresis loop.

	1	2
Space group	$P\bar{1}$	C 2/c
***a* (Å)**	14.2287(5)	34.4273(12)
***b* (Å)**	15.1581(6)	11.4107(4)
***c* (Å)**	21.3262(9)	26.1316(9)
***α* (º)**	80.3780(14)	90
***β* (º)**	84.2804(13)	128.2290(8)
***γ* (º)**	80.3780(14)	90
Z	2	4
***V* (Å³)**	4492.55	8064.02
***dFe₁- Fe₂* (Å)**	19.721	14.257

Table 2. Crystallographic parameters for DMA and Cesium salts

2.4. Conclusions

In summary, we have isolated a polyanionic Iron (II) trimer (**1**) that exhibits spin-crossover behavior for its central Iron (II) position above room temperature with a large thermal hysteresis. Transition dynamics are remarkably slow, allowing for an easy trapping of the excited spin state when the material is cooled down at reasonably slow rates (>5 K min^{-1}). As a result, this material exhibits bistability in the high-temperature range (280−400 K), but also in the low-temperature range (2−250 K), since the metastable HS state cannot relax back to the ground state up to very high temperatures (TTIESST = 250 K). This is the highest temperature at which memory effect remains in a thermally quenched SCO system. The extremely slow relaxation exhibited at such high temperatures opens unique possibilities for room-temperature applications.

On the other hand, we performed successfully the anionic exchange of **1** changing the $(Me_2NH_2)^+$ cation by a Cs^+. The compounds **2** achieved behavior around room temperature with an abrupt thermal hysteresis loop of 30 K. The HS state ca be trapped at rates of 10 $Kmin^{-1}$ carrying through a T_{TIESST} of 241 K. Moreover, a faster dynamics are present in **2** due to the stronger connectivity between trimers units.

2.5. References

1. Gütlich, P., Y. Garcia, and H.A. Goodwin, *Spin crossover phenomena in Fe(II) complexes.* Chemical Society Reviews, 2000. **29**(6): p. 419-427.
2. Bousseksou, A., et al., *Molecular spin crossover phenomenon: Recent achievements and prospects.* Chemical Society Reviews, 2011. **40**(6): p. 3313-3335.
3. Muñoz, M.C. and J.A. Real, *Thermo-, piezo-, photo- and chemo-switchable spin crossover iron(II)-metallocyanate based coordination polymers.* Coordination Chemistry Reviews, 2011. **255**(17-18): p. 2068-2093.
4. Gütlich, P., *Spin crossover - Quo vadis?* European Journal of Inorganic Chemistry, 2013(5-6): p. 581-591.
5. Quintero, C.M., et al., *Hybrid spin-crossover nanostructures.* Beilstein Journal of Nanotechnology, 2014. **5**: p. 2230-2239.
6. Costa, J.S., et al., *Three-way crystal-to-crystal reversible transformation and controlled spin switching by a nonporous molecular material.* Journal of the American Chemical Society, 2014. **136**(10): p. 3869-3874.
7. Ohkoshi, S.I., et al., *Light-induced spin-crossover magnet.* Nature Chemistry, 2011. **3**(7): p. 564-569.
8. Sessoli, R. and A.K. Powell, *Strategies towards single molecule magnets based on lanthanide ions.* Coordination Chemistry Reviews, 2009. **253**(19-20): p. 2328-2341.
9. Bogani, L. and W. Wernsdorfer, *Molecular spintronics using single-molecule magnets.* Nature Materials, 2008. **7**(3): p. 179-186.
10. Matsumoto, T., et al., *Programmable spin-state switching in a mixed-valence spin-crossover iron grid.* Nature Communications, 2014. **5**: p. 3865.
11. Craig, G.A., O. Roubeau, and G. Aromí, *Spin state switching in 2,6-bis(pyrazol-3-yl)pyridine (3-bpp) based Fe(II) complexes.* Coordination Chemistry Reviews, 2014. **269**(1): p. 13-31.

María del Pilar Maldonado Illescas

12. Larionova, J., et al., *Towards the ultimate size limit of the memory effect in spin-crossover solids.* Angewandte Chemie - International Edition, 2008. **47**(43): p. 8236-8240.
13. Duriska, M.B., et al., *A nanoscale molecular switch triggered by thermal, light, and guest perturbation.* Angewandte Chemie - International Edition, 2009. **48**(14): p. 2549-2552.
14. Phan, H., et al., *Photomagnetic response in highly conductive iron(II) spin-crossover complexes with TCNQ radicals.* Angewandte Chemie - International Edition, 2015. **54**(3): p. 823-827.
15. Seredyuk, M., et al., *Unprecedented multi-stable spin crossover molecular material with two thermal memory channels.* Chemistry - A European Journal, 2013. **19**(21): p. 6591-6596.
16. Gómez, V., et al., *Aqueous synthesis of sulfonate-functionalized 1,2,4-triazole ligands and their 2D Cd2+ coordination networks: Crystal structure and photoluminescent properties.* Dalton Transactions, 2013. **42**(18): p. 6374-6380.
17. Gómez, V., et al., *Hysteretic spin crossover above room temperature and magnetic coupling in trinuclear transition-metal complexes with anionic 1,2,4-triazole ligands.* Chemistry - A European Journal, 2014. **20**(18): p. 5369-5379.

Chapter 2

CHAPTER 3

Multifunctional PEDOT:PSS Composite Films with Iron (II) SCO Trimers

UNIVERSITAT ROVIRA I VIRGILI
AVANCES EN SISTEMAS INTERACTIVOS PARA PERSONAS CON PARÁLISIS CEREBRAL
María del Pilar Maldonado Illescas

3.1. Introduction

Organic conducting polymers have been a colossal discovery with a massive scientific and technological impact since in 1977 Shirakawa et al. synthetized the first conducting polymer [1]. Easy procedures to synthetize [2] and their magnificent electrical properties united with physical properties as flexibility, low cost and easy processing make that the formation of composites was quicker and productive. Poly(3,4-ethylenedioxythiophene): poly(styrene-sulfonate) (PEDOT:PSS) (Figure 1) is one of the most distinguished conducting polymer with real applications. The chemical structure consists in a polymer electrolyte formed by the positively charged conjugated PEDOT and the negative charged saturated PSS. The last one is a polymer surfactant that disperse and stabilize the PEDOT. PEDOT:PSS was first commercialized by Bayer AG calling Baytron®, although currently Clevios™ is the actual trade name commercialized by Heraeus forming an aqueous dispersion (deep blue opaque solution).

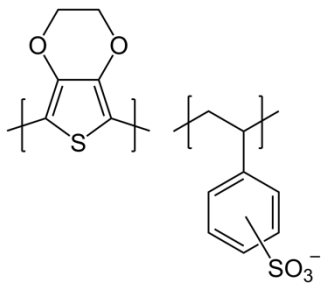

Figure 3.1. Chemical structure of PEDOT:PSS

Currently, the research of new polymers plays an important role and, specifically the formation of polymer composites with switchable magnetic properties are a promising building blocks for multifunctional materials [3, 4]. In particular, bistable multifunctional material tuning by the formation of composites with spin crossover compounds [5-8] where some properties can be changed by an external stimuli, such as temperature, pressure or light irradiation [9-11].

In this chapter, we focus on the development of a composite formed with PEDOT:PSS and a spin crossover compound verifying that with a dilution of a spin crossover, magnetic properties can be modified and even improved them.

3.2. Experimental

3.2.1. Synthesis

All reagents were commercially available and used without further purification.

$(Me_2NH_2)_6[Fe_3(L)_6(H_2O)_6]\cdot 6H_2O$ (1) were prepared according chapter 2.

1/PEDOT: PSS composite: 250 mg of (1) were dissolved in the minimum amount of water and were added into 7.63 mL of commercial PEDOT: PSS (PH 1000, solid content in water 1.0 - 1.3 %, $\rho \approx 0.00120\ \Omega\cdot cm$) under sonication for 15 minutes. After that, this dispersion was dropped on a clean glass (1 cm^2) until complete coverage and dried in an oven at 110ºC during 30 minutes, in order to

form a homogeneous and easy to peel off film. The cleaning of the glass begins with the sonication in acetone during 10 minutes and then with isopropyl alcohol.

3.3. Results and discussions

3.3.1 Synthesis and structural characterization

The synthesis was performed in a ratio of 2.5 SCO: 1 Polymer (w/w) dissolving the trinuclear in the minimum amount of water and mixing the solution with the dispersion of the polymer. The thickness of the film can be controlled dropping a particular amount of the dispersion in a 1x1 cm^2 of glass, thus it is possible to obtain a film without applying pressure and with the complete dispersion of the spin crossover that it is the aim of this project.

X-ray powder diffraction was carried out. The diffractogram is very noisy, but the appearance of some broad diffraction peaks suggests that this composite may contain phase segregation, being formed by the PEDOT:PSS and nanocrystrallites of **1**, at least partially (figure 3.2).

Scanning electron microscope (SEM) was performed on this films, which show a homogeneous distribution, with a thickness around 14 µm (figure 3.3). The presence of segregated inorganic nanoparticles inside the film could not be confirmed at this resolution, what indicates the nanoparticles must be very small, with sizes below 100 Å.

Chapter 3

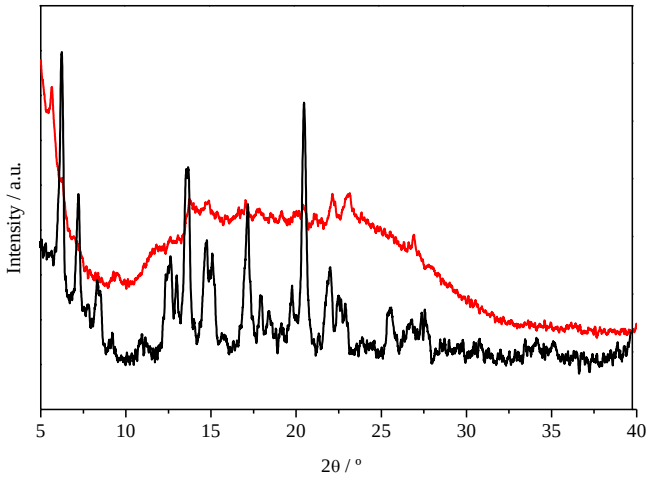

*Figure 3.2. X-ray powder diffractogram for **1** and **1/PEDOT: PSS***

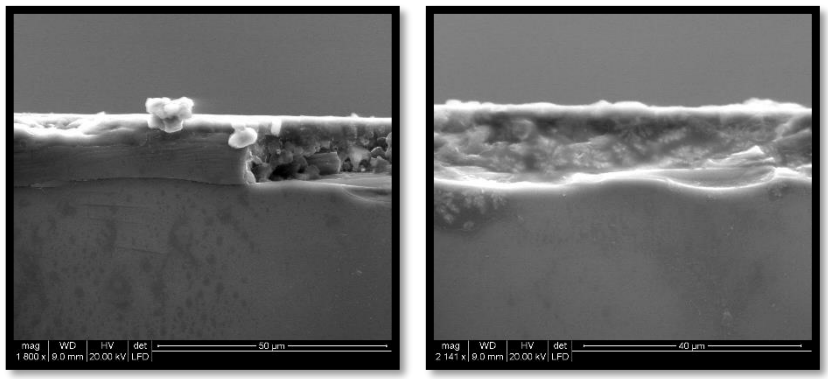

(A) (B)

*Figure 3.3. SEM image for **1/PEDOT: PSS***

María del Pilar Maldonado Illescas

3.3.2. Magnetic behavior

The composite **1/PEDOT:PSS** shows a gradual spin transition with a wide thermal hysteresis loop, which is similar to bulk, **1** (figure 3.4). However, the dynamic behavior is quite different.

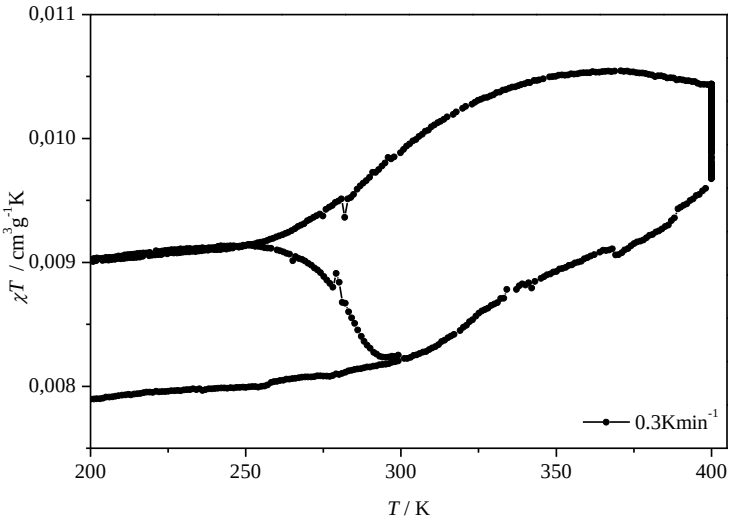

Figure 3.4. χT vs. T plots for 1/PEDOT:PSS in the 200-400K range (Scan rate ≈ 0.3 Kmin^{-1})

Figure 3.5 shows the magnetic behavior of the composite at different scan rates. The HS state is thermally populated with a $T_{1/2}(\uparrow)$ close to 400 K. However, the $T_{1/2}(\downarrow)$ could not be determined. The HS state is easily trapped, even at very low scan rates <0.3 K min^{-1}. As I mentioned in Chapter 1, the phenomenon of thermal-induced excited spin state trapping (*TIESST*) typically requires very fast cooling (10 Kmin^{-1}), and it is remarkable that in this case, *TIESST* phenomena appears at such slow cooling rates.

Chapter 3

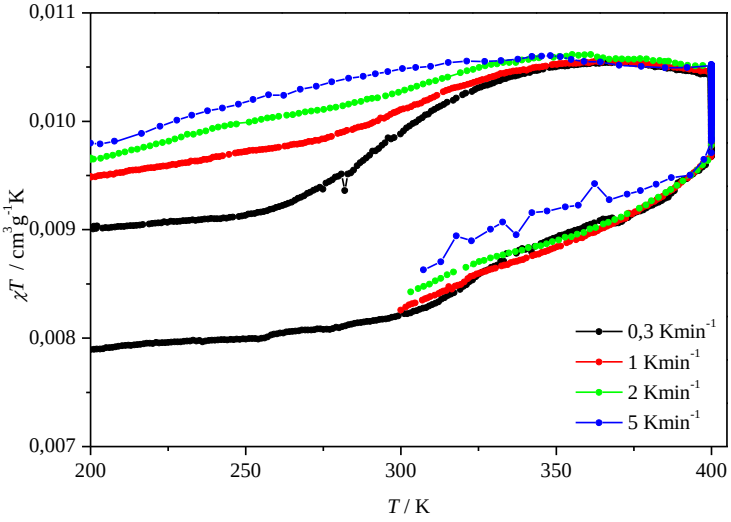

*Figure 3.5. χT vs. T plots for **1/PEDOT:PSS** at different scan rates*

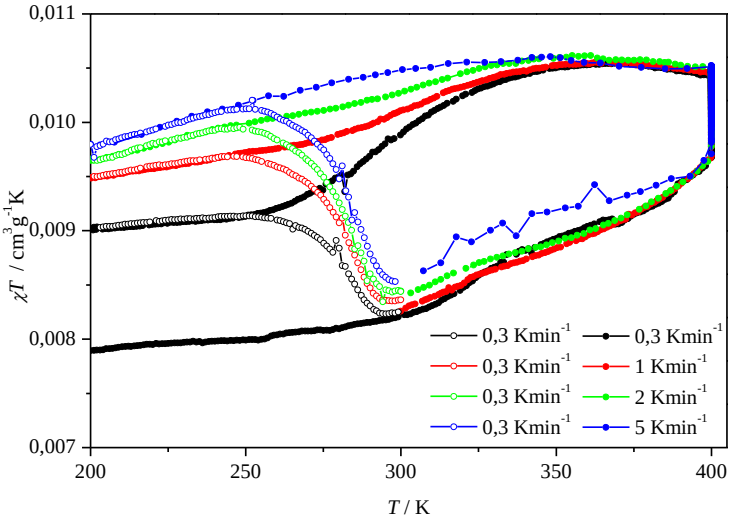

*Figure 3.6. χT vs. T plots for **1/PEDOT:PSS** at different scan rates (full dots) with their relaxation process at 0.3 Kmin^{-1} (empty dots)*

María del Pilar Maldonado Illescas

In a second heating branch, from the trapped HS state, the material relaxes back to the ground state at 0.3 $Kmin^{-1}$ (figure 3.6). From this data, we estimate a T_{TIESST} of 284 K (figure 3.7), 34 K higher than **1**, representing a new record as the highest T_{TIESST} ever observed [12].

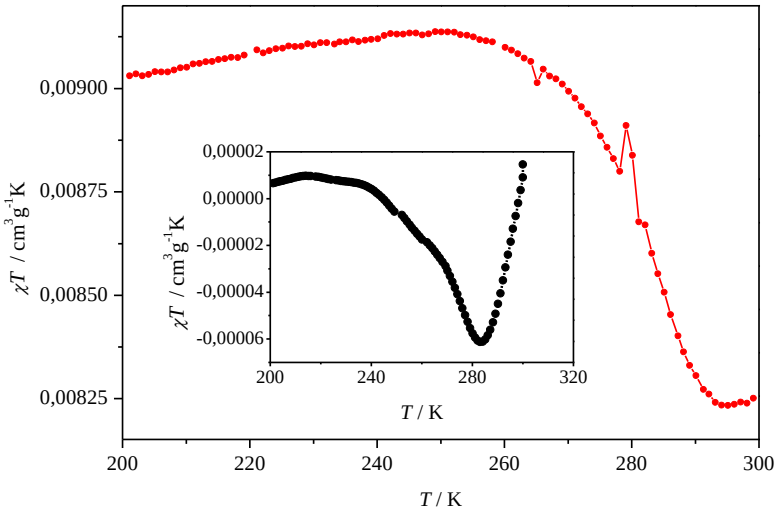

*Figure 3.7. Relaxation process for **1/PEDOT:PSS** at 0.3 $Kmin^{-1}$ when sample was cooling down quickly (5 $Kmin^{-1}$), (inset) δ(χT)/δT vs T curve for the latter heating branch*

In order to see if the observed magnetic process does not belong to a hidration/ dehydration process in the spin crossover or due to glass transition process magnetic measurements was carried out of pristine PEDOT:PSS processed by the same method that in the case of composite. In figure 3.8 are summarized these data.

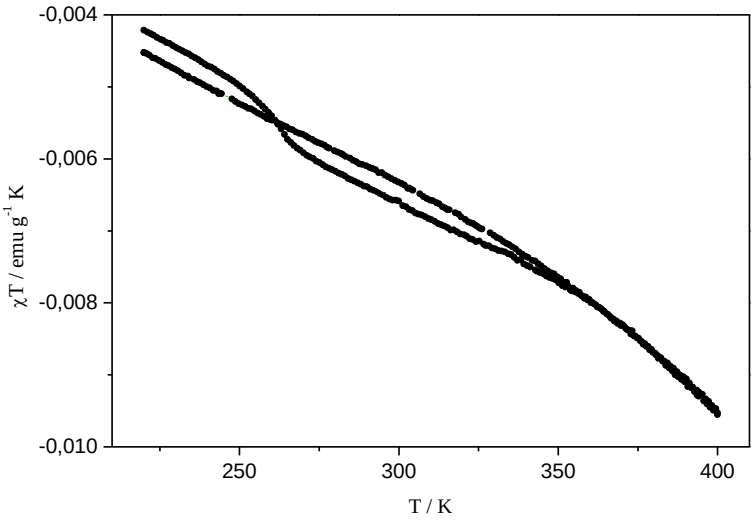

*Figure 3.8. χT vs. T plots for pristine **PEDOT:PSS** at 1 Kmin^{-1}*

Firstly, negative values are shown due to the presence of diamagnetic material in the sample. Moreover, there is no changes or hysteresis loop, so all magnetic behavior observed in the composite belong to **1** confirming that no process of hydration/dehydration occurs and no changes close to glass transition temperature appears.

3.3.3. Transport measurements

Transport measurements as a function of temperature at different scan rates are summarized in figure 3.9. Through the first heating and cooling samples (at 10 K min^{-1}), conductivity (σ) decreases monotonically, probably due to dehydration and conditioning of the film. After 4-5 cycles, the behavior is consistent and reproducible. The presence of only one hysteresis cycle, and of distinct transition

temperatures suggest the material to be formed by a single composite phase, and not by multiple phases of the trimer.

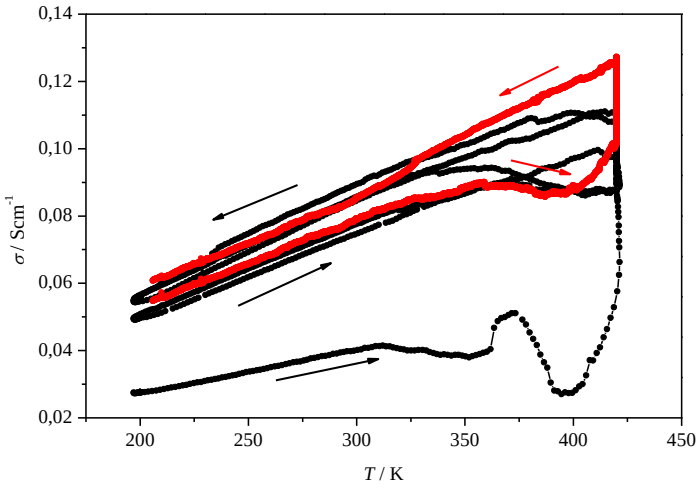

*Figure 3.9. Transport measurements. σ vs T for **1/ PEDOT:PSS** at different scan rates (10 Kmin^{-1} in black and 0.3 Kmin^{-1} in red)*

At this scan rate, the behavior is similar to a pristine PEDOT:PSS film (without SCO) obtained through the same processing method (figure 3.10).

In general, conductivity increases as temperature is increased, as expected in a semiconductor and the activation energy is 283.5 cm^{-1} (0.03515 eV), a typical value for this kind of materials.

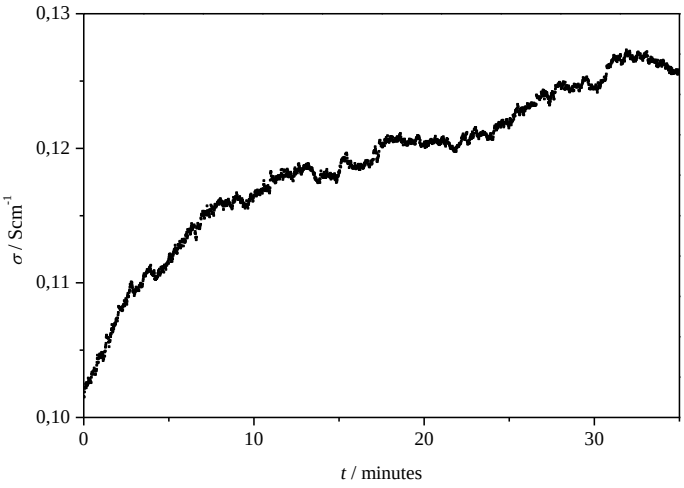

*Figure 3.10. Time evolution of the isothermal transport measurement for **1/ PEDOT:PSS** at constant temperature of 420 K*

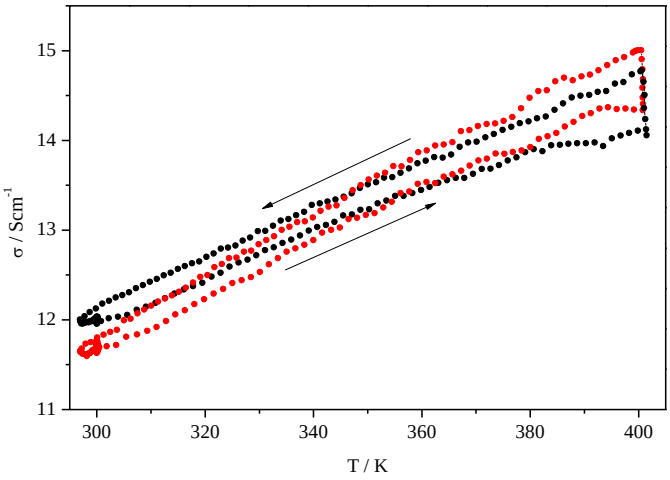

*Figure 3.11. Transport measurements. σ vs T at 5 Kmin^{-1} of pristine **PEDOT:PSS** (1st cycle in black and 2nd cycle in red)*

María del Pilar Maldonado Illescas

Since the SCO component can be trapped at very low cooling rates, we performed the transport measurements at 0.3 $Kmin^{-1}$ (red curve in figure 3.10). A hysteresis loop opens in the transport properties, analogous to the magnetic cycle. The dynamics of this process are also very slow. For example, conductivity increases at 420 K, and it does not reach its maximum value until almost 40 minutes (figure 3.10). This suggests the synergy between the spin transition and the transport properties in this composite material.

3.4. Conclusions

In this chapter we have successfully obtained PEDOT:PSS films with embedded 1. Although our objective was to obtain homogeneous films formed by a solid solution of the molecular fragments of 1 in the solvent areas of the PEDOT:PSS network, structural data indicates nanoparticles of 1 appear segregated from the polymer. Even in this case, we observe a clear effect upon the physical properties. As part of the composite, the dynamics of the spin transition have been significantly affected. Indeed, the T_{TIESST} has improved. **1**/PEDOT:PSS has a T_{TIESST} value of 284 K (250 K in bulk). We also observe a synergy between the trimer and conducting properties, since the transport measurements show an opening of a hysteresis cycle around the spin transitions. This is the first time that a SCO/conducting polymer shows synergy occurring in both directions.

These results also support the power of this composite strategy. Even when 1 was incorporated, probably, as solid state nanoparticles

into the conducting network, this is enough to yield strong interplay between both materials. This was already observed in the previous work with polylyrrole [13], where much bigger nanoparticles (> 400 nm). Although many other parameters will need to be studied, these data suggests that smaller nanoparticle sizes, as in this case, is not necessary (and it can be even counter effective) to affect the conductivity in the composite material.

3.5. References

1. Shirakawa, H., et al., *Synthesis of electrically conducting organic polymers: halogen derivatives of polyacetylene, (CH).* Journal of the Chemical Society, Chemical Communications, 1977(16): p. 578-580.
2. Sadki, S., et al., *The mechanisms of pyrrole electropolymerization.* Chemical Society Reviews, 2000. **29**(5): p. 283-293.
3. Ohkoshi, S.I., et al., *Light-induced spin-crossover magnet.* Nature Chemistry, 2011. **3**(7): p. 564-569.
4. Kahn, O. and C.J. Martinez, *Spin-transition polymers: From molecular materials toward memory devices.* Science, 1998. **279**(5347): p. 44-48.
5. Gural'Skiy, I.A., et al., *Spin crossover composite materials for electrothermomechanical actuators.* Journal of Materials Chemistry C, 2014. **2**(16): p. 2949-2955.
6. Yang, Y., et al., *Electrical switching and bistability in organic/polymeric thin films and memory devices.* Advanced Functional Materials, 2006. **16**(8): p. 1001-1014.
7. Qiu, D., et al., *Spin crossover-graphene nanocomposites: Facile syntheses, characterization, and magnetic properties.* RSC Advances, 2014. **4**(59): p. 31323-31327.
8. Baker, C.O., et al., *Size control of gold nanoparticles grown on polyaniline nanofibers for bistable memory devices.* ACS Nano, 2011. **5**(5): p. 3469-3474.
9. Mahfoud, T., et al., *Electrical properties and non-volatile memory effect of the [Fe(HB(pz) 3)2] spin crossover complex integrated in a microelectrode device.* Applied Physics Letters, 2011. **99**(5).
10. Létard, J.F., P. Guionneau, and L. Goux-Capes, *Towards spin crossover applications.* Top. Curr. Chem., 2004. **235**: p. 221-249.
11. Prins, F., et al., *Room-temperature electrical addressing of a bistable spin-crossover molecular system.* Advanced Materials, 2011. **23**(13): p. 1545-1549.
12. Wang, H., et al., *Unusual Solvent Dependence of a Molecule-Based FeII Macrocyclic Spin-Crossover Complex.* European Journal of Inorganic Chemistry, 2014. **2014**(29): p. 4927-4933.

13. Koo, Y.S. and J.R. Galán-Mascarós, *Spin crossover probes confer multistability to organic conducting polymers.* Advanced Materials, 2014. **26**(39): p. 6785-6789.

CHAPTER 4

Polymeric Iron (II) Nanoparticles with SCO: PEDOT:Tosylate Composite Films

UNIVERSITAT ROVIRA I VIRGILI
AVANCES EN SISTEMAS INTERACTIVOS PARA PERSONAS CON PARÁLISIS CEREBRAL
María del Pilar Maldonado Illescas

4.1. Introduction

Composites are a heterogeneous material which can combine their properties and improve them. One possibility can be the formation of a composite formed by a conducting polymer and an inorganic material such as spin crossover materials [1-3]. As we commented in the previous chapter, the discovery of conducting polymers supposed a revolution in Material Science due to their versatility. In this chapter, PEDOT:Tosylate was the polymer employed. This polymer is based on a cationic part, the $PEDOT^{+}$ and a dopant, the tosylate, which neutralize the charge and confer high conductivity.

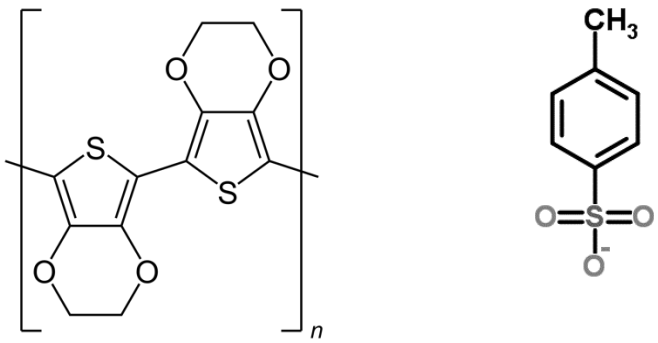

(A) (B)

Figure 4.1. The chemical structure of a) positively charged PEDOT and b) negatively charged tosylate counter ion

Furthermore, polymer composites with switchable magnetic properties or bistable material can be tunned by an external stimuli including pressure, temperature or light irradiation [4, 5]. In the past chapter we have doped the PEDOT:PSS polymers

with $(Me_2NH_2)_6[Fe_3(L)_6(H_2O)_6]\cdot 6H_2O$ (**1**) and we found that a moderate synergy is obtained. This might be due to the very slow dynamics of **1**, and the limited doping achieved with our synthetic strategy.

In terms of fast dynamics and wide hysteresis at or above room temperature the triazole based linear Iron(II) polymers are the most remarkable examples [6-8]. Being polymeric solid state materials, there is no effortless way to use them as doping in PEDOT films. However, their solid state and robust nature allows to obtain composite conducting films with organic polymers. This was already demonstrated in our group where polypyrrole was doped with Iron (II) polymers and a memory effect in transport measurements was achieved [3].

The different chemical and processing features of PEDOT with respect to polypyrrole represents a challenge, and in this chapter, we describe different approaches to obtain synergetic films, and the key processing parameters to optimize performance.

During this chapter, an Iron-triazole polymer is employed, specifically, 1,2,4-triazole is the ligand used [9-11]. This kind of spin crossover compounds arise particular interest because they have an abrupt transition close to room temperature and a wide hysteresis loop. Moreover, we focus on the performance of a composite built with PEDOT:Tos embedding the spin crossover polymers at different pressures and checking that spin crossover transition can be affected with pressure.

4.2. Experimental

4.2.1. Synthesis

All reagents were commercially available and used without further purification.

Synthesis of nanoparticles

[Fe(trz)(H-trz)$_2$] [BF$_4$]$_2$ (3): 20 mmol of $Fe(BF_4)_2 \cdot 6H_2O$ and 2.4 mmol of Ascorbic Acid were dissolved in 40 mL of distilled water. A solution of 40 mL of 1,2,4-Triazole (20 mmol) was dropped into the iron solution. The final solution became pink in a few minutes and, after 12 hours, it was filtered and washed. The product was dried at 60ºC for 24 hours and powdered by a ball mill at 25 Hz for 15 minutes.

Synthesis of polymers

PEDOT:Tos: 7,7 mmol of EDOT and 14.5 mmol of p-Toluenesulfonic Acid were added to 60 mL of distilled water afterward 15 mmol of $(NH_4)_2(S_2O_8)$ were added. The mixture was refluxed at 60ºC during 24 hours and after that, it was filtered and dried at room temperature.

Formation of composites

3/PEDOT:Tos: 0.4 g of PEDOT were mixed with 0.8 g of 3 and powdered for 15 minutes at 25 Hz by ball mill.

All mixtures were pressed in a pellet press die at the desired pressure (2, 5 and 10 Tons) obtaining circular films with, approximately, 2 mm of thickness and 13 mm of diameter.

Transport measurements of the composites showed in results and discussions are the 8th cycle when values are stable and reproducible.

4.3. Results and discussions

4.3.1. Synthesis and characterization

The synthesis was carried out in a ratio of 2 SCO: 1 Polymer (w/w) mixing the polymer and the spin crossover compound in the ball mill. After that the composite was pressed in a press die at different pressures with the objective to obtain distinct pellets. This process was made with a mechanical mixing because some problems of instability of nanoparticles at 60ºC appeared when polymerization was performed, so the procedure employed in previous work in our group was not the appropriate method [3].

Samples were characterized with X-ray powder diffraction. Figure 4.2 shows the X-ray powder diffraction pattern of **3** and **3/PEDOT:Tos**. No changes in the nanoparticles structure were observed in all pressures, although there is a decrease of crystallinity due to the amorphous character of the polymer.

María del Pilar Maldonado Illescas

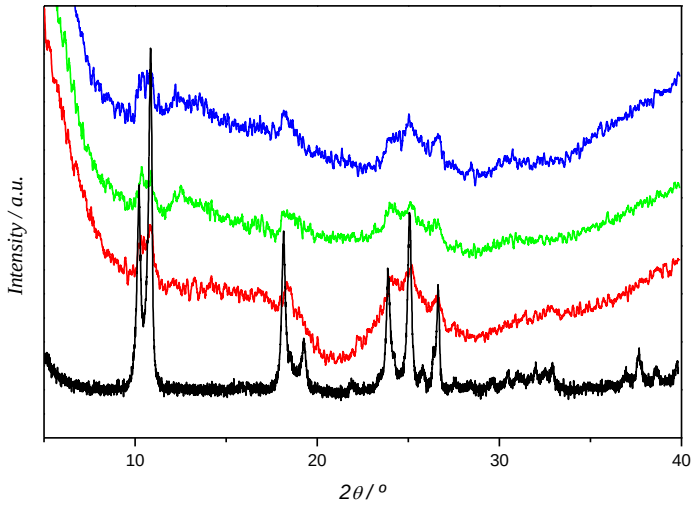

*Figure 4.1. X-ray powder diffraction pattern of **3** (black) and **3/PEDOT:Tos** at different pressures*
2 Tons in red, 5 Tons in green and 10 Tons in blue

4.3.1. Magnetic measurements

In figure 4.2 the magnetic behavior for **3** in powder at 5 $Kmin^{-1}$ is schematized. This compound presents an abrupt behavior close to room temperature with a wide hysteresis loop. All parameters are in good agreement with previous literature of this material [12].

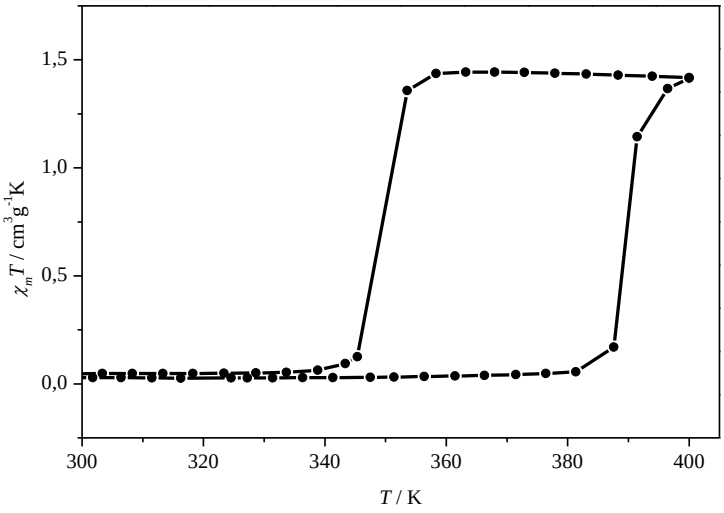

*Figure 4.2. $\chi_m T$ vs. T plots for **3** in the 320-400 K range*
Scan rate≈ 5 Kmin^{-1}

$T_{1/2}$(↑) is 390 K and $T_{1/2}$(↓) is close to 349 K with a thermal hysteresis loop of $\Delta T \approx$ 41 K. When **3** is embedded in the **3/PEDOT:Tos** composite films the magnetic behavior changes, independently of the pressure applied to make the pellet (Figure 4.3). In this case, the hysteresis loop is the same, $\Delta T \approx 41$ K [7], but $T_{1/2}$(↑) is 376 K ± 2 , and $T_{1/2}$(↓) is 337 K ± 2 for each pressure, so there is not a dependence with pressure but a difference in values appears between the **3** and the **3/PEDOT:Tos**, going to lower values.

This change in magnetic behavior must be due to pressure. It is well-known that spin transition is very sensitive to pressure stimuli. Typically, applied pressure stabilizes the ground low spin state, since it possesses less volume. It is surprising that, in this case,

María del Pilar Maldonado Illescas

we observed the opposite behavior. It is the high spin state the one getting stabilized being $T_{1/2}(\downarrow)$ the only variable affected.

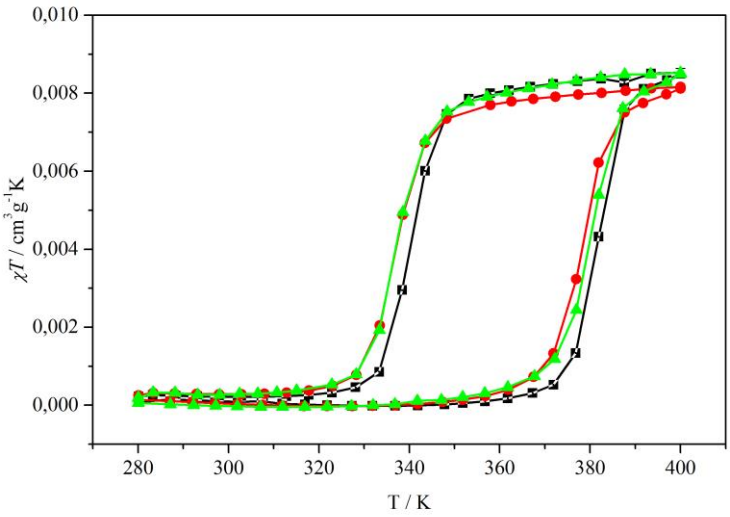

*Figure 4.3. χT vs. T plots for **3/PEDOT:Tos** composite in pellet at different pressures in the 300-400 K range*
Scan rate≈ 5 Kmin^{-1}
2 Tons in black, 5 Tons in red and 10 Tons in green

4.3.2. Transport measurements

Transport measurements were performed by 4-probe method. Firstly, we carried out the conductivity measurements of **3/PEDOT:Tos** films obtained under a pressure of 10 Tons (Figure 4.4). At room temperature, we observe a very low conductivity, about $\sigma = 5.09 \times 10^{-5}$ Scm^{-1}, quite unusual for a PEDOT film. When temperature is increased, conductivity follows a typical semiconducting behavior with an activation energy of 10.25 cm^{-1}.

Close to 390 K, a sharp increase in conductivity appears reaching a maximum of $\sigma = 0.168$ Scm^{-1}. This behavior corresponds to the spin transition of the nanoparticles, specifically, $T_{1/2}(\uparrow)$ belongs to the low spin to the high spin state transition (LS → HS). Moreover, $T_{1/2}(\downarrow)$ is close to 374 K which corresponds with the magnetic behavior.

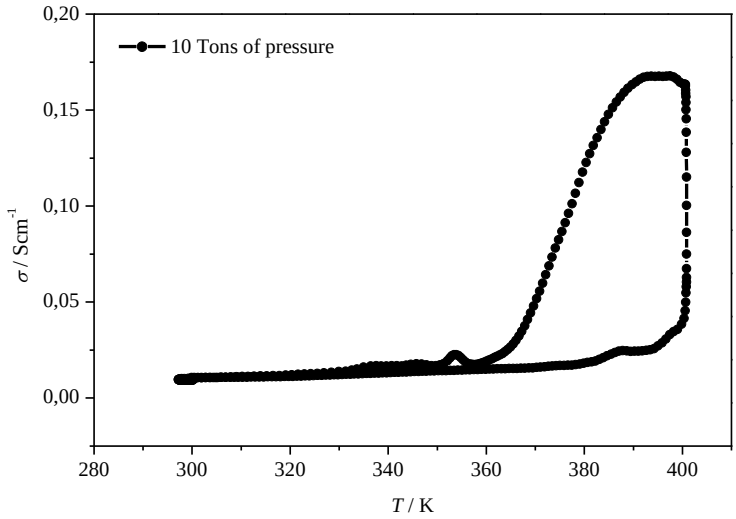

*Figure 4.4. Transport measurements of **3/PEDOT:Tos** at 10 Tons of pressure. Scan rate ≈5Kmin^{-1}*

In this case, the average difference in conductivity is bigger than 600% (figure 4.5). The Gauss curve is incomplete but it is impossible to perform measurements at temperatures above 400 K because the pellet breaks.

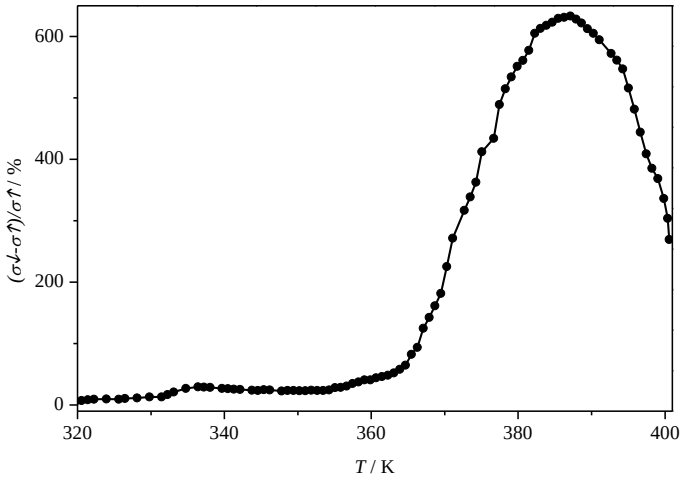

*Figure 4.5. Average difference between heating and cooling cycles of **3/PEDOT:Tos** at 10 Tons of pressure*

Secondly, transport measurements for **3/PEDOT:Tos** at 5 Tons of pressure were carried out (figure 4.6). The measurement starts at 0.004 Scm^{-1} of conductivity in LS state, higher than obtained for 10 Tons film. Upon spin transition, σ reaches 0.054 Scm^{-1} at 420 K, in HS state. In this case, the pellets are robust enough to study them at higher temperatures. The cycle is closed at 360 K going down in temperature, back to the LS conducting state. The difference in conductivity between HS and LS states is about three orders of magnitude. The maximum difference in conductivity during thermal hysteresis cycle is about 400 % (figure 4.7), being a very high value in this kind of materials [3]. For **3/PEDOT:Tos** at 5 Tons, the *T1/2(↑)* is 406 K and *T1/2(↓)* is 374 K, the same value that at 10 Tons. However, the advantage at this pressure is that pellets are more stable, because they do not break even at 425 K.

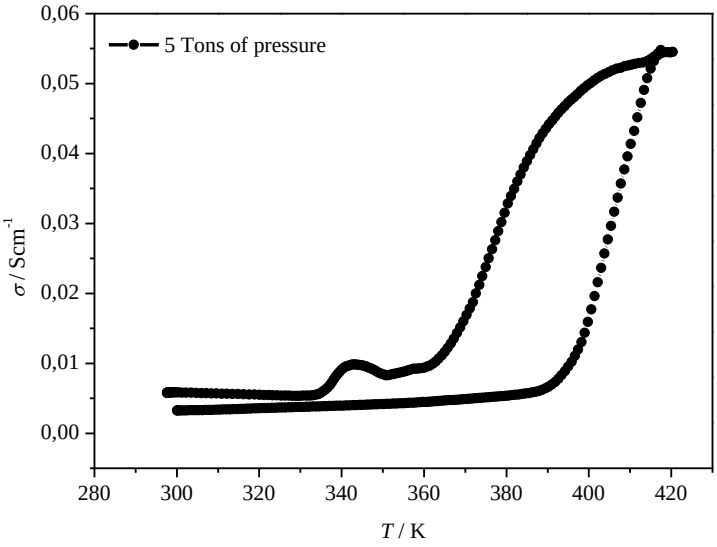

*Figure 4.6. Transport measurements of **3/PEDOT:Tos** at 5 Tons of pressure. Scan rate ≈5Kmin^{-1}*

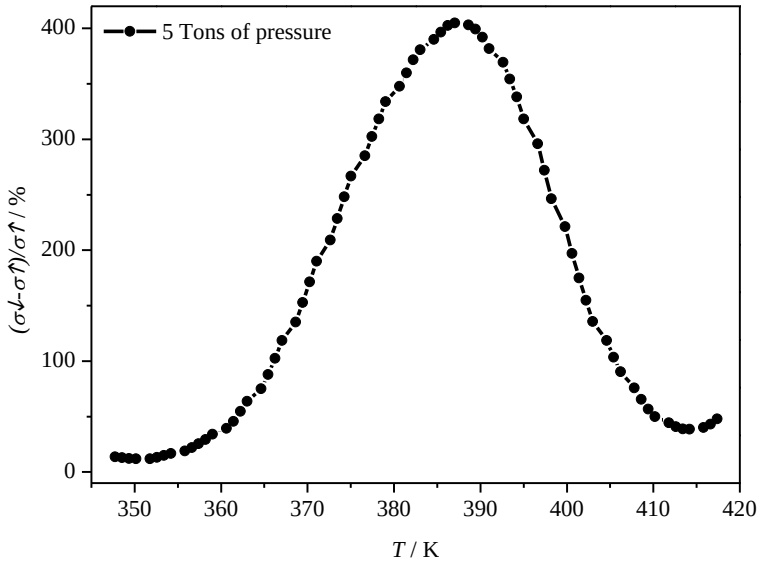

*Figure 4.7. Average difference between heating and cooling cycles of **3/PEDOT:Tos** at 5 Tons of pressure*

María del Pilar Maldonado Illescas

Finally, we performed the transport measurements of **3/PEDOT:Tos** at 2 Tons. For lower pressure, the hysteresis loop is maintained but shifts to higher temperatures being the $T_{1/2}(\uparrow)$ is 414 K (8 K higher than $T_{1/2}(\uparrow)_{5\ Tons}$) and the $T_{1/2}(\downarrow)$ is 384 K (10 K bigger than $T_{1/2}(\uparrow)_{5\ Tons}$ and $T_{1/2}(\uparrow)_{10\ Tons}$). Figure 4.8 summarizes this behavior.

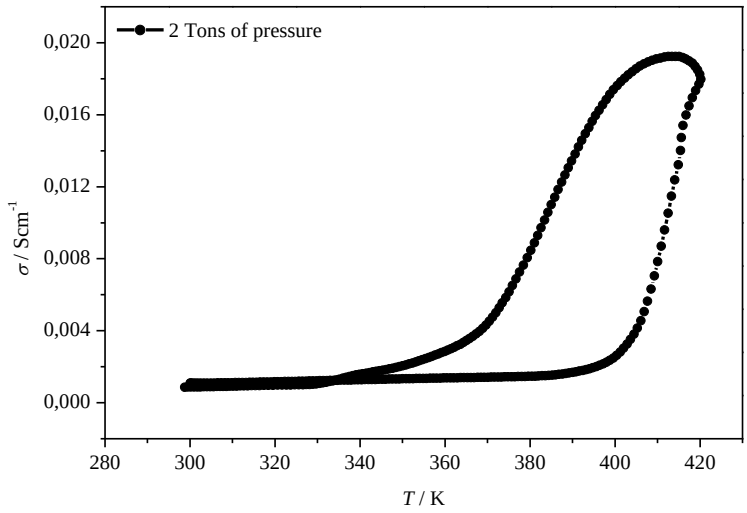

*Figure 4.8. Transport measurements of **3/PEDOT:Tos** at 2 Tons of pressure. Scan rate≈ 5 Kmin^{-1}*

Moreover, in this case the average difference is higher than measured for pellets 5 Tons, the value of average difference is close to 800 %, a record value in this kind of materials (figure 4.9).

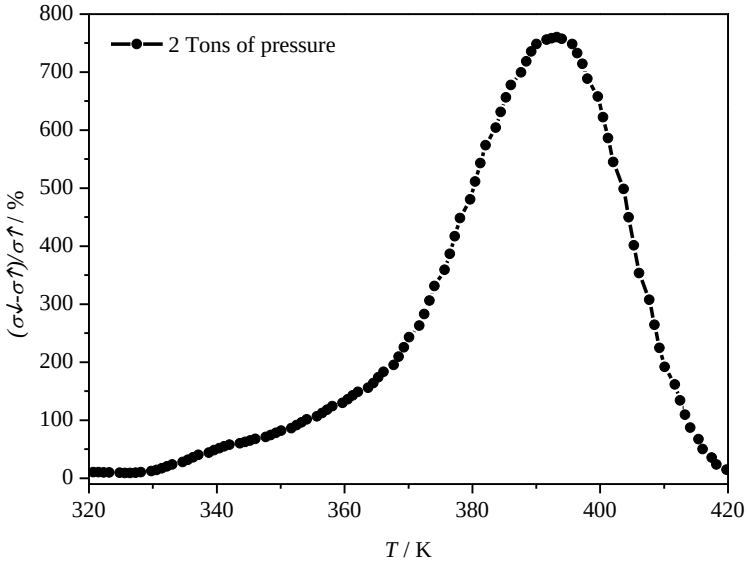

*Figure 4.9. Average difference between heating and cooling cycles of **3/PEDOT:Tos** at 2 Tons of pressure*

María del Pilar Maldonado Illescas

4.4. Conclusions

We have prepared composite films through a mechanochemical mixing of the SCO compound $[Fe(trz)(H\text{-}trz)_2]$ $[BF_4]_2$ with PEDOT:Tos. After mechanical mixing, these films were sintered at room temperature under pressure. No changes in magnetic behavior appears even at different pressures although the transport properties of these films depends greatly in the pressure applied, with better bulk conductivity as pressure increases. Moreover, the spin transition is stable, and is not affected by the processing conditions.

Additionally, these films exhibit an excellent synergy between magnetic and conducting properties. The spin transition triggers a dramatic transition in conductivity, reaching differences up to 800% between the LS and HS states. This is one order of magnitude higher than the analogous films that were previously studied in our group with polypyrrole [3]. An open question that remains is the origin of this unprecedented effect, which could be intrinsic of PEDOT:Tos, or due to the mechanochemical processing applied in this case.

4.5. References

1. Gomez-Romero, P., *Hybrid organic-inorganic materials - in search of synergic activity*. Advanced Materials, 2001. **13**(3): p. 163-174.
2. Yang, Y., et al., *Electrical switching and bistability in organic/polymeric thin films and memory devices.* Advanced Functional Materials, 2006. **16**(8): p. 1001-1014.
3. Koo, Y.S. and J.R. Galán-Mascarós, *Spin crossover probes confer multistability to organic conducting polymers.* Advanced Materials, 2014. **26**(39): p. 6785-6789.
4. Qiu, D., et al., *Spin crossover-graphene nanocomposites: facile syntheses, characterization, and magnetic properties.* RSC Advances, 2014. **4**(59): p. 31323-31327.
5. Kim, J.Y., et al., *Efficient Tandem Polymer Solar Cells Fabricated by All-Solution Processing.* Science, 2007. **317**(5835): p. 222-225.
6. Kahn, O. and E. Codjovi, *Iron(II)-1,2,4-Triazole Spin Transition Molecular Materials.* Philosophical Transactions of the Royal Society of London. Series A: Mathematical, Physical and Engineering Sciences, 1996. **354**(1706): p. 359-379.
7. Kahn, O. and C.J. Martinez, *Spin-Transition Polymers: From Molecular Materials Toward Memory Devices.* Science, 1998. **279**(5347): p. 44-48.
8. Roubeau, O., *Triazole-based one-dimensional spin-crossover coordination polymers.* Chemistry - A European Journal, 2012. **18**(48): p. 15230-15244.
9. Sugiyarto, K. and H. Goodwin, *Cooperative Spin Transitions in Iron(II) Derivatives of 1,2,4-Triazole.* Australian Journal of Chemistry, 1994. **47**(2): p. 263-277.
10. Lavrenova, L.G., et al., *1A1 ⇄ 5T2 Spin Transition in New Thermochromic Iron(II) Complexes with 1,2,4-Triazole and 4-Amino-1,2,4-Triazole.* Russian Journal of Coordination Chemistry, 2003. **29**(1): p. 22-27.
11. Varnek, V.A. and L.G. Lavrenova, *Mössbauer study of the influence of ligands and anions of the second coordination sphere in Fe(II) complexes with 1,2,4-triazole and 4-amino-1,2,4-*

triazole on the temperature of the 1A 1⇆5 T 2 spin transitions. Journal of Structural Chemistry, 1995. **36**(1): p. 104-111.

12. Kröber, J., et al., *Spin transitions and thermal hystereses in the molecular-based materials [Fe(Htrz)2(trz)](BF4) and [Fe(Htrz)3](BF4)2·H2O (Htrz = 1,2,4-4H-triazole; trz = 1,2,4 triazolato).* Chemistry of Materials, 1994. **6**(8): p. 1404-1412.

Chapter 4

CHAPTER 5

Significant Enhancement in a SCO: Polypyrrole Composite

UNIVERSITAT ROVIRA I VIRGILI
AVANCES EN SISTEMAS INTERACTIVOS PARA PERSONAS CON PARÁLISIS CEREBRAL
María del Pilar Maldonado Illescas

Chapter 5

5.1. Introduction

Nowadays, society confronts to the decline of fossil fuel supplies and the demands of the World in energy, therefore, thermoelectric material have been considerable attention because involve the conversion of heat in energy. Moreover, thermoelectric materials provide an alternative route to convert solar energy into electrical power, especially for solid-state heat engines [1, 2]. On the other hand, thermoelectric devices stand out due to the advances of technologies such as low weight, miniaturization, , high reliability and the possibility to make a one- pack system (without moving parts) [3]. The performance of thermoelectric material are quantified with the figure of merit, $\boldsymbol{ZT = S^2\sigma T/\kappa}$ where S is the Seebeck coefficient, σ is the electrical conductivity, T is the absolute temperature and κ is the thermal conductivity [4]. $\boldsymbol{S^2\sigma}$ is the power factor, P, in the dimensionless figure of merit and is related to the usable power attainable from the thermoelectric [5]. Bi_2Te_3 and $BiSbTe_5$ alloys have been the thermoelectric material par excellence, because they have achieved significant ZT but the high cost, poor processability and storage and the most important the high toxicity were a loser candidate [6-8]. For this reason, organic material, especially organic conducting polymers such as polypyrrole (PP) [9, 10], polythiophene (PTf) [11, 12] or poly(3,4-hylenedioxythiophene): poly(styrenesulfonate) (PEDOT:PSS) [13, 14], are a promising material to explore due to flexibility, low

thermal conductivity, high electrical conductivity, easy procedures to synthesize or nontoxicity. Furthermore, thermoelectric properties can be tuned by the doping process [15] and the formation of composites is an important route to improve them too [16, 17]. Polypyrrole is one of the most important employed conducting polymers and their excellent electric and thermal properties can be leveraged properly for multifunctional devices [18, 19].

In this chapter, we take advantage of the performance of composites with a conducting polymer, the polypyrrole (PP) via in situ chemical polymerization and a spin crossover chain with wide hysteresis loop and spin transition close to room temperature.

5.2. Experimental

5.2.1. Synthesis

Synthesis of nanoparticles

[Fe(NH2-trz)$_3$][SO$_4$] (4): 25 mmol of $FeSO_4 \cdot 7H_2O$ and 2.4 mmol of Ascorbic Acid were dissolved in 50 mL of distilled water. A solution of 50 mL of 4-amino-1,2,4-Triazole (75 mmol) was dropped into the iron solution. $NaSO_4$ were added little by little in order to induce the precipitation. The precipitate were washed with water four times and dried at 60ºC. After that, the product were powdered in the ball mill for 15 minutes at 25 Hz.

Synthesis of composites

4/PP composite films: 1.96 g of p-Toluenesulfonic acid (12 mmol) and 1.4 g of $(NH_4)_2[S_2O_8]$ (6 mmol) were dissolved in 200 mL of distilled water in an ice-water bath. 0.96 g of pyrrole (12.96 mmol) and 2.4 g of **4** were added sequentially to this solution, and stirring maintained during 1 hour. After filtering the **4/PP** precipitate, it was washed with water, and dried at 60ºC. After that, 300 mg of composite were powdered in the ball mill for 15 minutes at 25 Hz and pressed at 2.5 Tons with a pellet press die with 13 mm of diameter and 1.67 mm of thickness.

All the samples were thermally pretreated in an oven with seven cycles from 300 to 400 K at 1 $Kmin^{-1}$ in order to make the electrical and thermal measurements reproducible and stable.

5.3. Results and discussions

5.3.1. Synthesis

The synthesis was carried out in a ratio 2.5 (**4**): 1 PP (w/w). The nanoparticles were added during the polymerization reaction in order to embed the nanoparticles in the polymer matrix. In previous work, the composites after reaction was filtered, pressed and it was ready to measure [19] but in this case, it was impossible due to the films homogeneity because a film without superficial imperfections was required for the thermoelectric measurement. With this, the composite was filtered, washed and then dried at 60ºC. After that, the powder was homogenized in a ball mill and then a film was

achieved with a pellet press die obtaining a homogeneous pellet appropriate for this kind of measures.

5.3.2. Magnetic measurements

Figure 5.1 shows the magnetic behavior for **4** at 5 $Kmin^{-1}$ in a 300-400 range. This compound presents an abrupt spin transition with a well-shaped thermal hysteresis loop around 31 K. The magnetic moment increases with a $T_{1/2}\uparrow$ of 363 K, when the temperature decreases $T_{1/2}\downarrow$ occurs at 332 K.

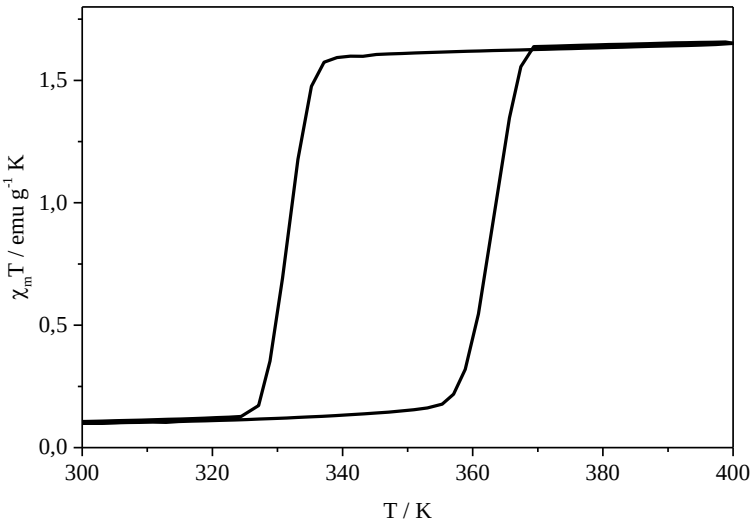

*Figure 5.1: $\chi_m T$ vs. T plots for **4** in the 300-400 K range*
Scan rate≈ 5 $Kmin^{-1}$

However, when nanoparticles are embbebed in the polymer the change a little bit. The abrup transition is maintained but the hysteresis loop is smaller, close to 26 K, due to the strength of the pressure. Moreover, the transition temperatures go to lower values of temperature reaching a $T_{1/2}\uparrow$ close to 351 K and a $T_{1/2}\downarrow$ of 325.5 K

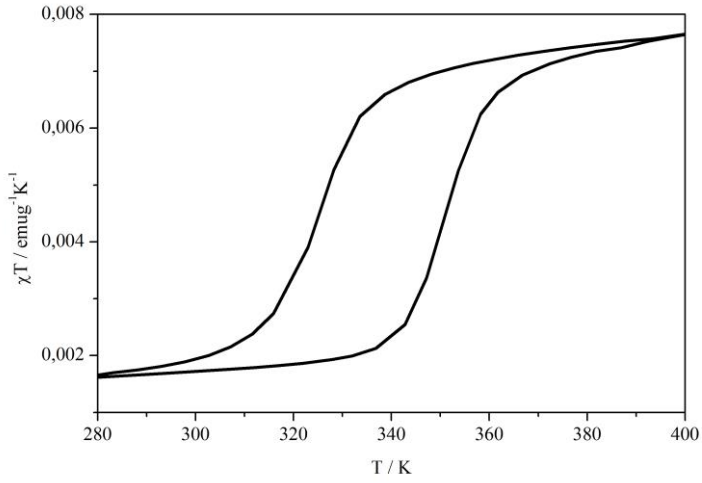

*Figure 5.2. $\chi_m T$ vs. T plots for **4/PP** in the 300-400 K range at 2.5 Tons of pressure. Scan rate≈ 5 Kmin^{-1}*

5.3.3. Electrical measurements

Transport measurements

Transport properties were determined by four-probe method. The measurement starts at 300 K with a conductivity of σ= 0.008 Scm^{-1} with a typical semiconductor behavior (linear trend). No evidence of spin transition is observed due to the reconditioning of the sample despite thermal treatment was performed after. When this branch ends (at 400 K), there is a significant conductivity close

to 0.013 Scm^{-1} (figure 5.3 in black). When the sample is cooled down a VRH behavior appears obtaining σ_0= 0.0437 Scm^{-1} and a T_0= $1.63 \cdot 10^{13}$ K. Bellow 340 K, HS→LS transition takes place. (figure 5.3 in red) reaching 0.02 Scm^{-1} at room temperature. When temperature is increased conductivity follows a typical semiconducting behavior. It is possible to model to a Mott variable-range hopping (VRH) mechanism, as a classic charge-transport in conducting polymers, with σ_0 = 0.0427 Scm^{-1} and a Mott parameter, T_0= $1.31 \cdot 10^{13}$ K. Above 358 K, σ shows an abrupt transition resulting of the LS→ HS transition (figure 5.3 in green). HS state reaches 0.095 Scm^{-1} at 400 K. Moreover, the electrical hysteresis loop is close to 36 K, with $T_{1/2}\uparrow$ of 373 K and $T_{1/2}\downarrow$ close to 337 K.

In figure 5.4 the average of conductivity is shown. A huge improvement in the average is produced, so the formation of films using the pellet press die enhances the average considerably comparing with the reported previously in our group [19]. An improvement in the average is observed, because the particles have been packaged better and therefore the difference between HS and LS is more appreciable.

Chapter 5

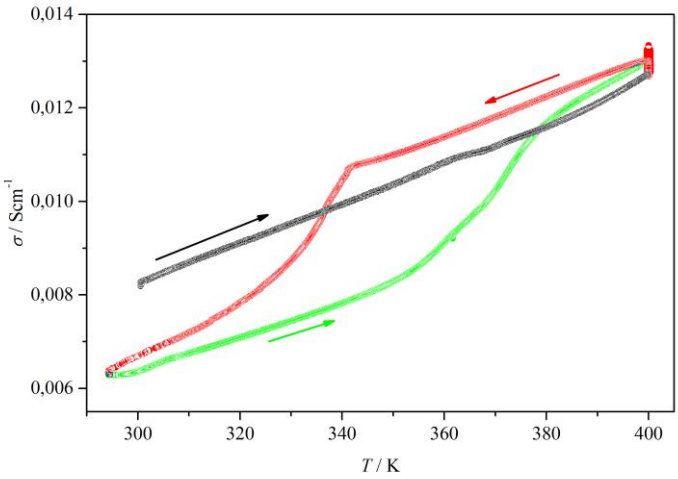

Figure 5.3. Transport measurements of 4/PP at 2.5 Tons of pressure (fisrt heating in black, cooling in red and second heating in green). Scan rate ≈ 0.5 Kmin^{-1}

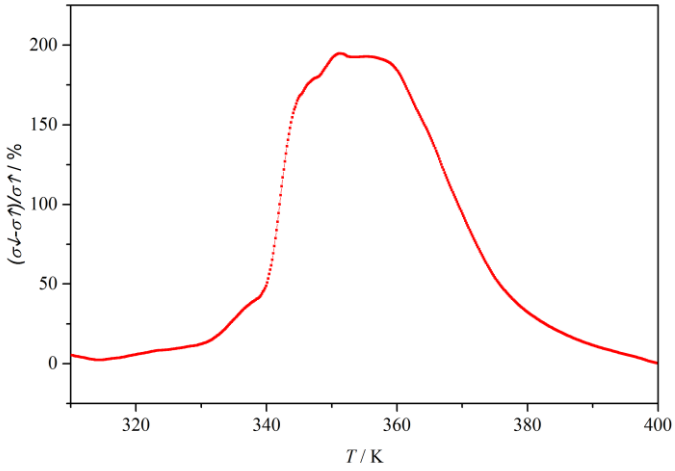

*Figure 5.4. Average difference between heating and cooling cycles of **composite** at 2.5 Tons of pressure*

Hall Effect measurements

The Hall Effect measurement in polymers shows positively charged carriers for acceptor-doped polymer (p-type) and negatively charged carrier for donor-doped polymer (n-type). Therefore, hall effect can be obtained, using a homemade system with a permanent magnet with 1,4 T employing Van der Pauw method [20] at room temperature. The procedure and results for this technique is detailed in Appendix I and III, respectively. The characteristic parameters obtained from this technique are Hall mobility, carrier concentration, Hall resistivity and kind of semiconductor.

In table 5.1, Hall parameters are summarized for pristine PP and 4/ PP composite It is clear that the nanoparticles presences modified the resistivity and the hall parameters. Although, in these work the values are different compare with others reports (reference). This difference can be attributed to the high magnetic field because the optimal value reported for these measurements is around 5000 G and the main goal of this section is determine the semiconductor type.

Parameters	Prystine PP	4/PP composite
ρ / Ω·cm	0.0618	$9.97 \cdot 10^{3}$
n / cm^{-3}	$2.913 \cdot 10^{13}$	$5.5534 \cdot 10^{13}$
μ / $cm^2V^{-1}s^{-1}$	$2.896 \cdot 10^{6}$	11.2698
Semiconductor type (V_H sign)	p-type (+)	p-type (+)

Table 5.1. Hall parameters of pristine PP and 4/ PP composite

I-V curves

I-V characteristics for 4/PP composite were carried out at room temperature giving a linear trend, so it is possible to say that a ohmic behavior is the characteristic in this case. In order to improve the electrical contact, the measurement was performed using a gold contact film. So, this lineal trend can be observed because the ohmic interaction between Au film/PP interface can be affected.

In figure 5.5 are summarized these measurements. This means that the difference of potential is proportional to the current, therefore resistance is independent of the current and tension, achieving the Ohm law, V= R·I.

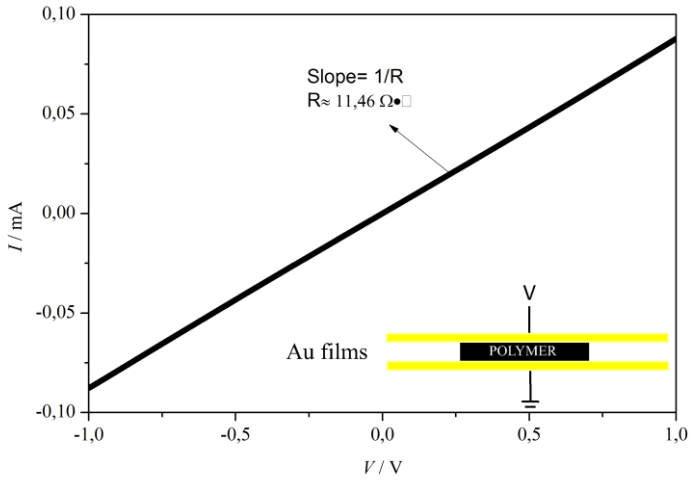

Figure 5.5. I-V curves of 4/PP

Moreover, it is possible to calculate the resistance through the I-V curve which is the inverse of the slope, 1/R and in addition,

the resistivity, ρ. In figure 5.5 are shown the value of resistivity, 11.46 Ω per square.

5.3.4. Thermoelectric measurements

Thermoelectric measurements were performed with the system follows in appendix I. Thermoelectric effect is studied in figure 5.6. The system works with one side at constant temperature of 25 ºC and the other one is variable. In the figure 5.6, ΔV versus ΔT are summarized. As much for pristine polypyrrole for 4/PP composite when the temperature difference between hot and cold junction is higher, more voltage is generated and this behavior follows a growing trend. The difference between pristine PP and 4/ PP should be attributed to the nanoparticles presence into the polypyrrole matrix. These nanoparticles are defects that are added to the polymer which contain carriers that are comprised of crosslinking sites. This behavior can be model for thermopower in a heterogeneous material developer by Kaiser [21].

An improvement appears for 4/PP at high temperatures. The pristine polypyrrole has defects too but they are restricted by the acoustic mismatch between the polymer and the gold-coated (Au/PP interface) confining a strong electrical conduction due to Ohmic interfacial contact [22].

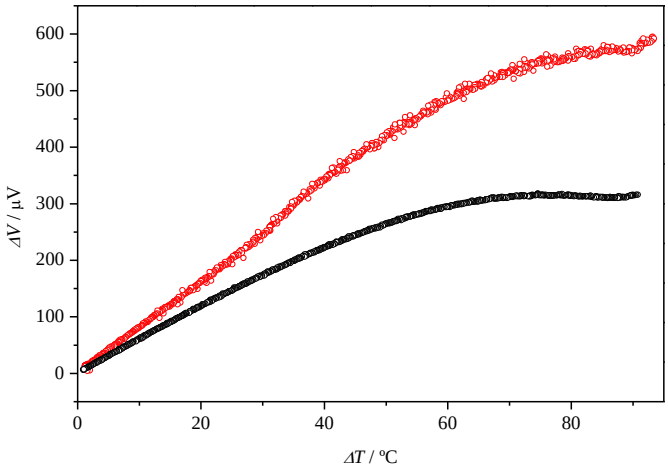

Figure 5.6. thermoelectric measurements. ΔV vs ΔT
Prystine polypyrrole in black and 4/PP in red

On the other hand, 4/PP presents an increase of the slope at high temperatures, we can attribute to the presence of nanoparticles and their spin crossover transition. When nanoparticles go from the spin state to high spin state, the carrier conduction is allowed efficiently, and as a result the accumulation of carriers is higher obtaining a difference of voltage much better than in pristine polypyrrole.

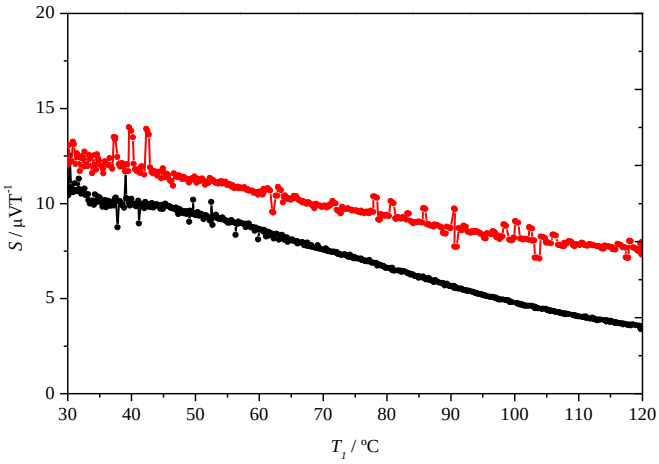

Figure 5.6. Seebeck coefficient, S vs T1
Prystine polypyrrole in black and 4/PP in red

Figure 5.6 displays the Seebeck coefficient of all samples. The Seebeck coefficient of all samples is positive, suggesting p-type conductive behavior. S goes to lower values when temperature increases due to the differences in electrical conductivity. Moreover, it is clear that in both of cases these is a decrease in the trend. In addition, S in 4/PP decrease less than the pristine polypyrrole and basically it is because of nanoparticles change their volume when they go to high pin state. So, carrier transport is more efficient and the Seebeck effect decrease suddenly.

5.4. Conclusions

In conclusion, we improved considerably the conductivity for **4/PP** modifying the procedure of pellet formation. A bistability appears in the transport measurement due to the spin crossover compound, (4) achieving a hysteresis loop about 36 K comparing with the magnetic behavior for the composite that presents a value of 10 K of difference and it is ΔT of 26 K.

Moreover, magnetic behavior is affected too, reporting a value of hysteresis loop for **4** in powder close to 31 K comparing with the 26 K describe for the composite. In addition, hysteresis loop goes to lower values in the case of composite ($T_{1/2}\uparrow$ = 351 K and $T_{1/2}\downarrow$= 325.5 K) while for 4 carries out a ($T_{1/2}\uparrow$ = 363 K and $T_{1/2}\downarrow$= 332 K), due to a the pressure effect.

We performed fortunately the type of semiconductor, in agreement with the reported in literature. We obtained on both of cases a p-type semiconductor, a material, which are characterized because it possess holes in the matrix of the structure.

Finally, we demonstrated an improvement in the Seebeck coefficient when nanoparticles are in the matrix of the polymer. No high values are presented due to the low conductivity shown in the samples.

As a suggestion, a good idea can be increase the electrical conductivity in order to compete with the reporter in literature.

5.5. References

1. Dresselhaus, M.S., et al., *New Directions for Low-Dimensional Thermoelectric Materials.* Advanced Materials, 2007. **19**(8): p. 1043-1053.
2. Bell, L.E., *Cooling, Heating, Generating Power, and Recovering Waste Heat with Thermoelectric Systems.* Science, 2008. **321**(5895): p. 1457-1461.
3. DiSalvo, F.J., *Thermoelectric Cooling and Power Generation.* Science, 1999. **285**(5428): p. 703-706.
4. Sootsman, J.R., D.Y. Chung, and M.G. Kanatzidis, *New and Old Concepts in Thermoelectric Materials.* Angewandte Chemie International Edition, 2009. **48**(46): p. 8616-8639.
5. Medlin, D.L. and G.J. Snyder, *Interfaces in bulk thermoelectric materials: A review for Current Opinion in Colloid and Interface Science.* Current Opinion in Colloid & Interface Science, 2009. **14**(4): p. 226-235.
6. Venkatasubramanian, R., et al., *Thin-film thermoelectric devices with high room-temperature figures of merit.* Nature, 2001. **413**(6856): p. 597-602.
7. Coleman, J.N., et al., *Two-Dimensional Nanosheets Produced by Liquid Exfoliation of Layered Materials.* Science, 2011. **331**(6017): p. 568-571.
8. Hicks, L.D. and M.S. Dresselhaus, *Effect of quantum-well structures on the thermoelectric figure of merit.* Physical Review B, 1993. **47**(19): p. 12727-12731.
9. Yoon, C.O., et al., *Transport near the metal-insulator transition: Polypyrrole doped with PF6.* Physical Review B, 1994. **49**(16): p. 10851-10863.
10. Kemp, N.T., et al., *Thermoelectric power and conductivity of different types of polypyrrole.* Journal of Polymer Science, Part B: Polymer Physics, 1999. **37**(9): p. 953-960.
11. Österholm, J.E., et al., *Synthesis and properties of FeCl4-doped polythiophene.* Synthetic Metals, 1987. **18**(1-3): p. 213-218.
12. Shi, H., et al., *Facile fabrication of pedot:pss/polythiophenes bilayered nanofilms on pure organic electrodes and their*

thermoelectric performance. ACS Applied Materials and Interfaces, 2013. **5**(24): p. 12811-12819.

13. Kim, D., et al., *Improved Thermoelectric Behavior of Nanotube-Filled Polymer Composites with Poly(3,4-ethylenedioxythiophene) Poly(styrenesulfonate).* ACS Nano, 2010. **4**(1): p. 513-523.
14. Jiang, F.X., et al., *Thermoelectric performance of poly(3,4-ethylenedioxythiophene): Poly(styrenesulfonate).* Chinese Physics Letters, 2008. **25**(6): p. 2202-2205.
15. Maiz, J., et al., *Enhancement of thermoelectric efficiency of doped PCDTBT polymer films.* RSC Advances, 2015. **5**(82): p. 66687-66694.
16. Du, Y., et al., *Research progress on polymer–inorganic thermoelectric nanocomposite materials.* Progress in Polymer Science, 2012. **37**(6): p. 820-841.
17. Guo, Z., et al., *Fabrication and characterization of iron oxide nanoparticles filled polypyrrole nanocomposites.* Journal of Nanoparticle Research, 2009. **11**(6): p. 1441-1452.
18. Oroumei, A., H. Tavanai, and M. Morshed, *Hysteresis Phenomenon in Heat–Voltage Curves of Polypyrrole-Coated Electrospun Nanofibrous and Regular Fibrous Mats.* Journal of Electronic Materials, 2015. **44**(7): p. 2250-2259.
19. Koo, Y.S. and J.R. Galán-Mascarós, *Spin crossover probes confer multistability to organic conducting polymers.* Advanced Materials, 2014. **26**(39): p. 6785-6789.
20. Patois, T., et al., *Characterization of the surface properties of polypyrrole films: Influence of electrodeposition parameters.* Synthetic Metals, 2011. **161**(21-22): p. 2498-2505.
21. Kaiser, A.B., *Thermoelectric power and conductivity of heterogeneous conducting polymers.* Physical Review B, 1989. **40**(5): p. 2806-2813.
22. Yan, L., et al., *High Seebeck Effects from Hybrid Metal/Polymer/Metal Thin-Film Devices.* Advanced Materials, 2011. **23**(35): p. 4120-4124.

María del Pilar Maldonado Illlescas

CHAPTER 6

General Conclusions

UNIVERSITAT ROVIRA I VIRGILI
AVANCES EN SISTEMAS INTERACTIVOS PARA PERSONAS CON PARÁLISIS CEREBRAL
María del Pilar Maldonado Illescas

General conclusions

In this Doctoral thesis, a new Iron (II) based 1,2,4-triazole derivatives anionic complexes are synthetized and spin crossover in order to have the fundamental elements in the development of functional materials. Moreover, we carried out successfully the incorporation in conducting polymer forming composites so as to approach to real application such as devices or switches. Following a detail in every chapter are reviewed:

In *chapter two*, we have isolated a polyanionic Iron (II) trimer (**1**) that exhibits spin-crossover behavior for its central Iron (II) position above room temperature with a large thermal hysteresis. Transition dynamics are remarkably slow, allowing for an easy trapping of the excited spin state when the material is cooled down at reasonably slow rates (>5 K min^{-1}). As a result, this material exhibits bistability in the high-temperature range (280−400 K), but also in the low-temperature range (2−250 K), since the metastable HS state cannot relax back to the ground state up to very high temperatures (TTIESST = 250 K). This is the highest temperature at which memory effect remains in a thermally quenched SCO system. The extremely slow relaxation exhibited at such high temperatures opens unique possibilities for room-temperature applications.

On the other hand, we performed successfully the anionic exchange of **1** changing the $(Me_2NH_2)^+$ cation by a Cs^+. The

compounds **2** achieved behavior around room temperature with an abrupt thermal hysteresis loop of 30 K. The HS state ca be trapped at rates of 10 $Kmin^{-1}$ carrying through a T_{TIESST} of 241 K. Moreover, a faster dynamics are present in **2** due to the stronger connectivity between trimers units.

On the other hand, in *chapter three* we have successfully obtained PEDOT:PSS films with embedded 1. Although our objective was to obtain homogeneous films formed by a solid solution of the molecular fragments of 1 in the solvent areas of the PEDOT:PSS network, structural data indicates nanoparticles of 1 appear segregated from the polymer. Even in this case, we observe a clear effect upon the physical properties. As part of the composite, the dynamics of the spin transition have been significantly affected. Indeed, the T_{TIESST} has improved. **1**/PEDOT:PSS has a T_{TIESST} value of 284 K (250 K in bulk). We also observe a synergy between the trimer and conducting properties, since the transport measurements show an opening of a hysteresis cycle around the spin transitions. This is the first time that a SCO/conducting polymer shows synergy occurring in both directions.

These results also support the power of this composite strategy. Even when 1 was incorporated, probably, as solid state nanoparticles into the conducting network, this is enough to yield strong interplay between both materials. This was already observed in the previous work with polylyrrole [13], where much bigger nanoparticles (> 400 nm). Although many other parameters will need to be studied, these data suggests that smaller nanoparticle

María del Pilar Maldonado Illescas

sizes, as in this case, is not necessary (and it can be even counter effective) to affect the conductivity in the composite material.

Moreover, in *chapter four*, we have prepared composite films through a mechanochemical mixing of the SCO compound $[Fe(trz)(H\text{-}trz)_2]$ $[BF_4]_2$ with PEDOT:Tos. After mechanical mixing, these films were sintered at room temperature under pressure. No changes in magnetic behavior appears even at different pressures although the transport properties of these films depends greatly in the pressure applied, with better bulk conductivity as pressure increases. Moreover, the spin transition is stable, and is not affected by the processing conditions.

Additionally, these films exhibit an excellent synergy between magnetic and conducting properties. The spin transition triggers a dramatic transition in conductivity, reaching differences up to 800% between the LS and HS states. This is one order of magnitude higher than the analogous films that were previously studied in our group with polypyrrole [3]. An open question that remains is the origin of this unprecedented effect, which could be intrinsic of PEDOT:Tos, or due to the mechanochemical processing applied in this case.

Finally, in *chapter five*, we improved considerably the conductivity for **4/PP** modifying the procedure of pellet formation. A bistability appears in the transport measurement due to the spin crossover compound, (4) achieving a hysteresis loop about 36 K comparing with the magnetic behavior for the composite that presents a value of 10 K of difference and it is ΔT of 26 K.

Moreover, magnetic behavior is affected too, reporting a value of hysteresis loop for **4** in powder close to 31 K comparing with the 26 K describe for the composite. In addition, hysteresis loop goes to lower values in the case of composite ($T_{1/2}\uparrow$ = 351 K and $T_{1/2}\downarrow$= 325.5 K) while for 4 carries out a ($T_{1/2}\uparrow$ = 363 K and $T_{1/2}\downarrow$= 332 K), due to a the pressure effect.

We performed fortunately the type of semiconductor, in agreement with the reported in literature. We obtained on both of cases a p-type semiconductor, a material, which are characterized because it possess holes in the matrix of the structure.

Finally, we demonstrated an improvement in the Seebeck coefficient when nanoparticles are in the matrix of the polymer. No high values are presented due to the low conductivity shown in the samples. As a suggestion, a good idea can be increase the electrical conductivity in order to compete with the reporter in literature.

APPENDIX I

Methods

UNIVERSITAT ROVIRA I VIRGILI
AVANCES EN SISTEMAS INTERACTIVOS PARA PERSONAS CON PARÁLISIS CEREBRAL
María del Pilar Maldonado Illescas

María del Pilar Maldonado Illescas

I.1. Electrical measurements

In this thesis, electrical conductivity measurements were performed in a system with a cryostat (VPF Series, Janis) thermal-controlled with a temperature controller (Lakeshore 325 Temperature Controller). Furthermore, a sourcemeter (Keithley series 2400) and a nanovoltmeter (Keithley series 2182A) were connected to the sample using a 4-probe method. All these instruments are connected and synchronized with the system-design platform LabVIEW from National Instruments (NI).

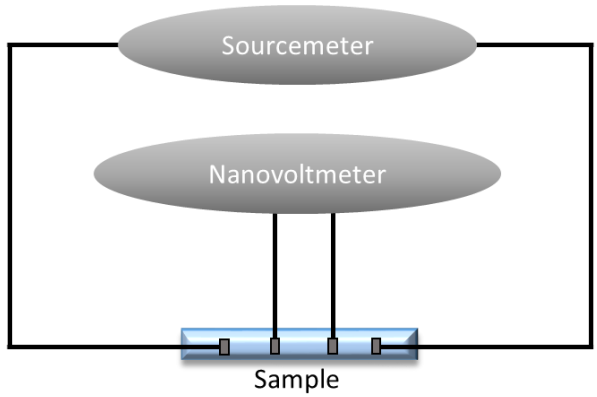

Figure III.1: Schematic representation of the set up used in transport measurements

There are a lot of way of connections in transport measurements, for example, two-probe method, four-probe method, Van der Pauw system, etc. Although the most used in this work was

the four-probe method. This method is the most commonly used in low resistive procedures and the employ of four points of contact on the film or crystal are involved. These contact points were done with wires, usually made of Gold, Copper or Platinum and about 10 to 50 µm of diameter. The wires were fixed with a Silver conductive epoxy with a cold soldering. The epoxy cure with the time and the curing can be accelerated heating the sample up. Using four probes method prevents errors in the measurement due to the wire resistance, the diffusion resistance under each wire and the contact resistance between the wire (and epoxy) and the sample. In the system, two probes were connected to the current source while a nanovoltmeter was connected to the other wires in order to measure the obtained voltage, as shows in the figure:

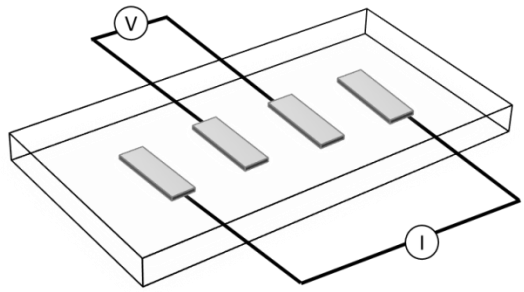

Figure III.2: Arrangement for the transport measurements in a film or monocrystal by four-probe method

Resistance is calculated with Ohm's law as follows:

$$R = \frac{V}{I}$$

María del Pilar Maldonado Illescas

where R is the resistance of the material (units: Ohms)

I is the applied current intensity (units: Amperes)

And V is the obtained voltage (units: Volts)

Resistance is proportional to the sample size, so the use of resistivity concept is required. The volume resistivity, ρ ($\Omega \cdot cm$) takes into account the morphology of the sample and is given as:

$$\rho = \frac{V \cdot A}{I \cdot L}$$

Where V is the measured voltage (V)

I is the current source (A)

A is cross-section of the sample (cm^2)

L is length of the sample (cm)

In figure shows the squema for a sample:

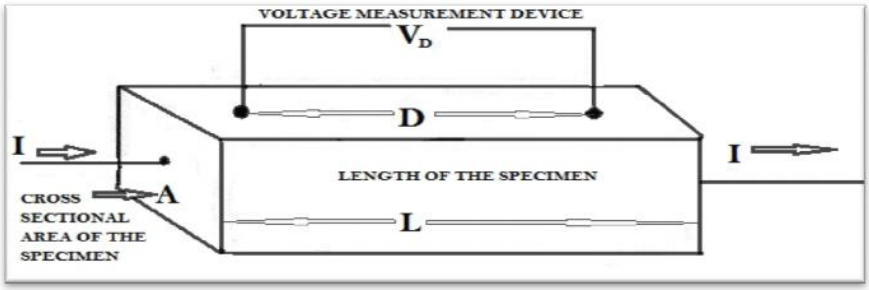

Figure III.3. Electrical resistivity measurements by four-probe method

Besides, conductivity can also be calculated, and is defined as inverse of the resistivity:

Appendix I

$$\rho = \frac{1}{\sigma}$$

where σ is the conductivity of the sample and is expressed in Siemens/cm (S/cm) or 1/Ohms·cm=$(\Omega \cdot cm)^{-1}$.

Besides, other system to know the electronic behavior in semiconductors is the Van der Pauw system, which can calculate the carrier concentration, the mobility, the resistivity in a film and the type of the semiconductor, and this is our aim with the measure. The technique consists in the application of constant current and the measure of the voltage produced. A sourcemeter (Keithley series 2400) and a nanovoltmeter (Keithley series 2182A) were connected to the sample using Van der Pauw system. All these instruments were connected and synchronized with the system-design platform LabVIEW from National Instruments (NI).

First of all, the way of connection distributed in the sample is very important. In this case, four wires of copper are used, and pasted on the sample employing a silver epoxy. In figure III.4 the distribution of contacts for the measurement are shown, where the magnetic field is applied through the z-axis perpendicular to the current flux which flow longitudinally in the material.

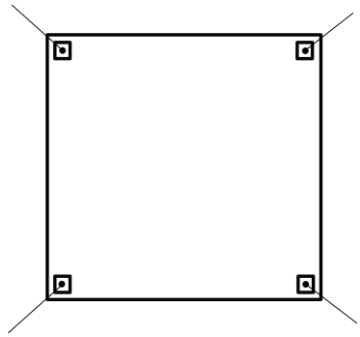

María del Pilar Maldonado Illescas

Figure III.4. Van der Pauw contacts

When this behavior occurs, a modification of potential appears perpendicularly to the current flux. The difference of potential is giving as:

$$V_H = R_H \frac{IB}{d} \tag{III.1}$$

where d is the thickness of the film and R_H is the Hall coefficient that is expressed as:

$$R_H = \frac{-n\mu_e^2 + p\mu_h^2}{e(\mu_e + p\mu_h)^2} \tag{III.2}$$

In this case, electrical transport due to electrons and holes are taking into account. μ_e and μ_h are the mobilities, and n and p are the concentration of electrons and holes carriers, respectively.

The objective of the resistivity measurements is to determine the sheet resistance, R_S. Van der Pauw demonstrated that there are two characteristic resistances, R_A and R_B, associated with the corresponding terminals which is showed in figure III.5.

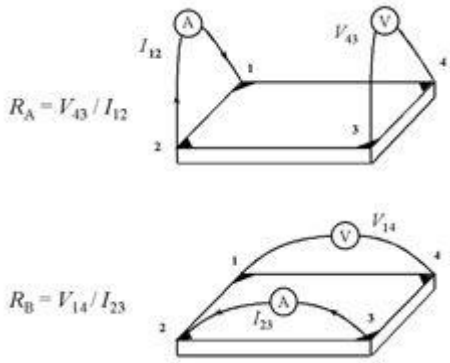

Figure III.5. Resistivity measurements

Appendix I

R_A and R_B are calculated by means of the following expressions:

$$R_A = \frac{V_{43}}{I_{12}} \tag{III.3}$$

$$R_B = \frac{V_{14}}{I_{23}} \tag{III.4}$$

R_A and R_B are related to the sheet resistance R_S through the Van der Pauw equation:

$$\exp\left(-\pi {R_A}/{R_S}\right) + \exp\left(-\pi {R_B}/{R_S}\right) = 1 \tag{III.5}$$

Which can be solved numerically for R_S. The bulk electrical resistivity ρ can be calculated using

$$\rho = R_S \cdot d \tag{III.6}$$

The objective of the Hall measurements in the van der Pauw technique is to determine the sheet carrier density n_s by measuring the Hall voltage V_H. The Hall voltage measurements consist of a series of voltage measurements with a constant current, I and a constant applied magnetic field, B perpendicular to the plane of the sample. Conveniently, the same sample, shown again in figure III.6, can also be used for the Hall measurement. To measure the Hall voltage V_H, a current, I is forced through the opposing pair of contacts 1 and 3 and the Hall voltage V_H (= V_{24}) is measured across the remaining pair of contacts 2 and 4. Once the Hall voltage, V_H is acquired, the sheet carrier density, n_s (cm^{-1}) can be calculated as follow:

$$n_s = 8 \cdot 10^{-8} \frac{IB}{q|\sum V_i|} \tag{III.7}$$

María del Pilar Maldonado Illescas

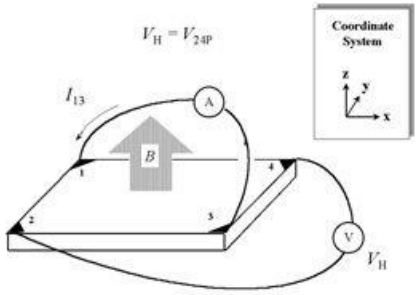

Figure III.6. Hall Voltage measurements

where $\sum V_i$ is the sum the different voltages and is given by:

$$V_C = V_{24P} - V_{24N} \quad \text{(III.8)}$$

$$V_D = V_{42P} - V_{42N} \quad \text{(III.9)}$$

$$V_E = V_{13P} - V_{13N} \quad \text{(III.10)}$$

$$V_F = V_{31P} - V_{31N} \quad \text{(III.11)}$$

In the case that the sum of voltage is negative, the sheet carrier density is called n_s, and the material is a n-type semiconductor but if the sum of voltage is positive, the sheet carrier density is named p_s and the film is a p-type semiconductor.

The bulk carrier density p or n (cm^{-3}) can be determined as follows, if the conducting layer thickness d of the sample is known:

$$n = {}^{n_s}/_{d} \quad \text{(III.12)}$$

$$p = {}^{p_s}/_{d} \quad \text{(III.13)}$$

Finally, it is possible to calculate the Hall mobility, μ ($cm^2V^{-1}s^{-1}$) from sheet carrier density and sheet resistance as follow:

Appendix I

$$\mu = \frac{1}{q n_S R_S} \qquad \text{(III.14)}$$

I.2. Magnetic measurements

Magnetic measurements were carried out in a Quantum Design MPMS® (Magnetic Property Measurement System) susceptometer, the equipment more sensitive in the magnetic field measurements based on DC Josephson effect. The principal components of these instruments are: a superconducing magnet separated by insulated layers in order to form two parallel Josephson junctions which are able to generate high magnetic fields; a superconducting detection coil which couples inductively to the sample, the detector SQUID (Superconducting Quantum Interference Device) connected to the detection coil and a superconducting magnetic shield around the SQUID [1].

A powder sample (exact weight) is placed in a diamagnetic capsule. In order to hold the powder, a glass wool is employed, in this way, when vacuum is applied; the loss of the sample is avoided. Besides, a Kapton® polyimide film is pasted around the capsule to prevent the separation of the two parts of the capsule. Finally, the capsule is placed inside of a plastic tube. It is very important to

María del Pilar Maldonado Illescas

know exactly the weight of the capsule, the sample, the glass wool and the Kapton because it is required in the calculation of susceptibility, in this appendix will be explained with more detail.

Appendix I

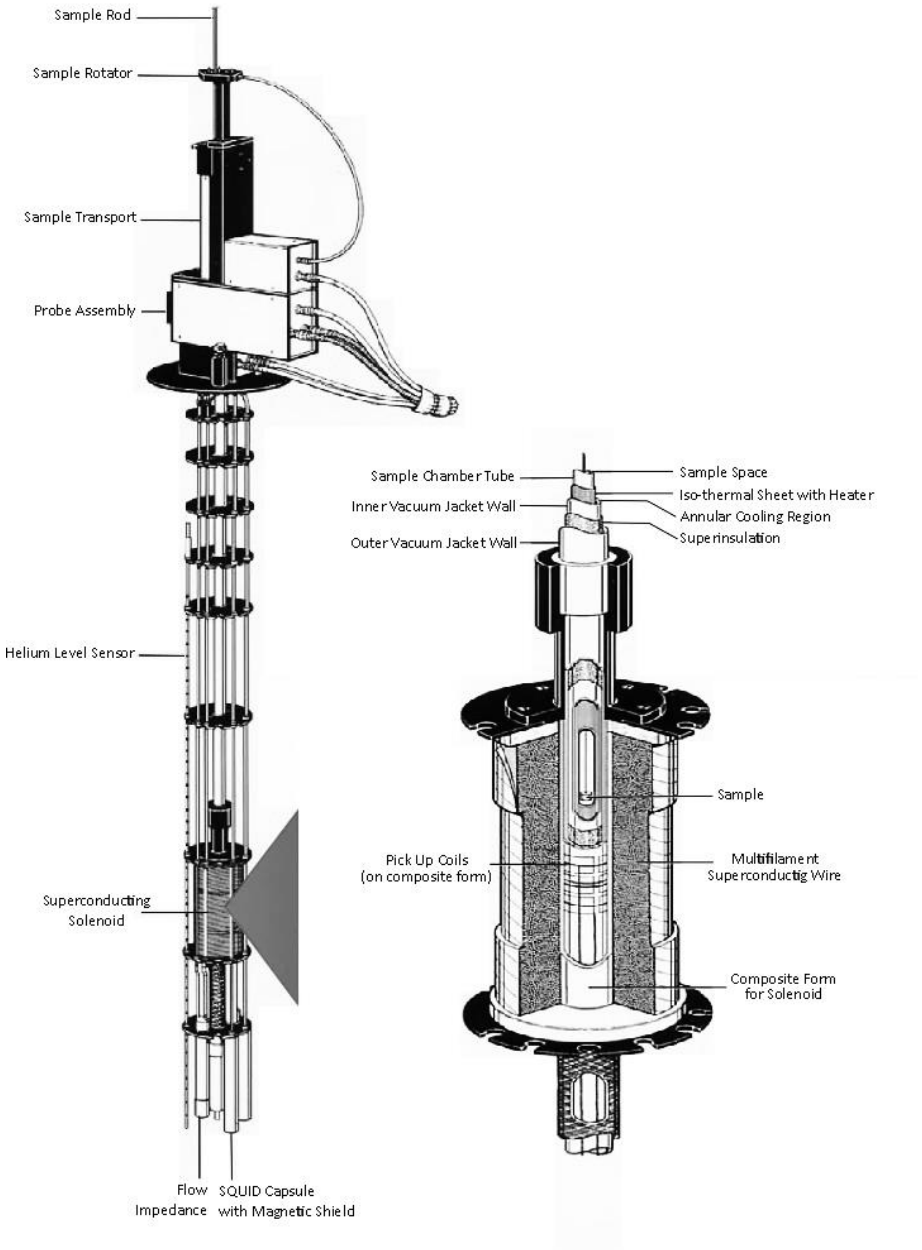

Figure III.7. MPMS components

María del Pilar Maldonado Illescas

Figure III.8. A sample ready to measure.

After introducing the sample inside the equipment, vacuum is applied in the antechamber and the chamber with helium gas in order to avoid air and humidity traces. Then, the sample is centered, where the signal is higher. This procedure is performed by moving the sample (1) through the superconducting detection coil (2) placed outside of the sample chamber and in the middle of the magnet (3).

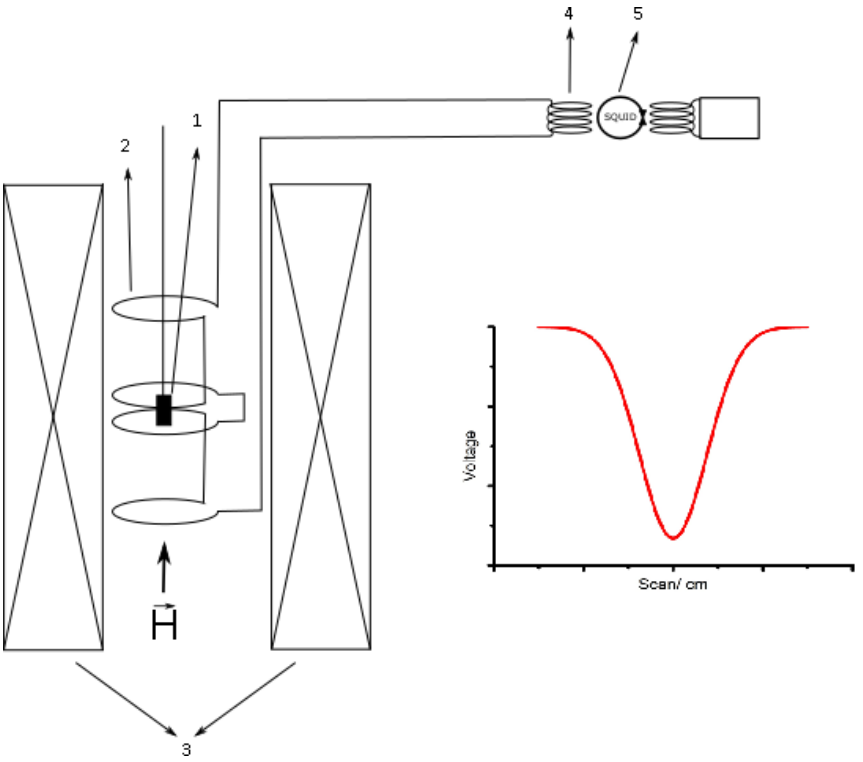

Figure III.9. Measurement of the sample

Appendix I

When the sample crosses through the coil, magnetic flow changes in the coil and it is proportional to the sample signal. Magnetic moment of the sample produces an induced current ΔI in the detection coil related with the flux variation of the magnetic field, Δφ and the impedance of the circuit L by the next expression:

$$\Delta I = \frac{\Delta \varphi}{L} \tag{III.15}$$

The detection coil and the SQUID input coil (4) form a closed-circuit, SQUID (5) detects this generated current and transforms it in a potential difference proportional to the current. In addition, the potential difference is proportional to the magnetic moment of the sample calculated automatically by the equipment giving the magnetization, M expressed in emu.

When a material is exposed to an external and homogenous magnetic field, H a magnetization appears, M that induces the sample. Thus, the magnetic susceptibility, χ_m, can be calculated like this:

$$\chi_v = \frac{M}{H} \tag{III.16}$$

$$\chi_g = \frac{\chi_v}{\rho} \tag{III.17}$$

The measured susceptibility consists of two components; a paramagnetic contribution, positive and based on a permanent magnetic dipolar moment and only acts towards applied magnetic

María del Pilar Maldonado Illescas

field direction; and a diamagnetic contribution, with negative signal, and causes a very small magnetic moment in comparison with the paramagnetic contribution.

If the magnetic susceptibility is related with the amount of the sample in the measurement, molar magnetic susceptibility, χ_m is obtained as:

$$\chi_m = \chi_g * \frac{M_r}{m} + \left(\frac{M_r}{2} * 10^{-6}\right) \quad \text{(III.18)}$$

where M_r is the molar mass of the compound

m is the weight of the sample

and $M_r/_2$ is the diamagnetic contribution correction.

On the other hand, magnetic susceptibility can also be calculated theoretically for a specific compound and compared with the experimental value. This process gives an idea about the experimentally obtained compound and can be expressed as:

$$\chi_m = \frac{N_A \cdot g^2 \cdot \mu_B^2 S(S+1)}{3k_B T} \quad \text{(III.19)}$$

which N_a is the Avogadro number

g is the Landé factor for an electron (g= 2.0023 for an Iron (II))

μ_B is the effective magnetic moment

k_B is the Boltzmann constant

T is the given temperature in every moment expressed in Kelvin

and *S* is the spin in the studied system (for a spin crossover with Iron (II), *S*= 2 in the paramagnetic state (HS) and *S*= 0 in the diamagnetic state (LS).

In this thesis, spin transition can be followed plotting $\chi_m T$ ($cm^3 \cdot mol^{-1} \cdot K$) versus *T* (K).

I.3. Thermoelectric measurements

Thermoelectric measurements were performed with a handmade dispositive formed by two thermally controlled peltiers with two Watlow temperature controllers. The acquired voltages were measured with a nanovoltmeter (Keithley series 2182A). The diagram is summarized in figure III.10.

María del Pilar Maldonado Illescas

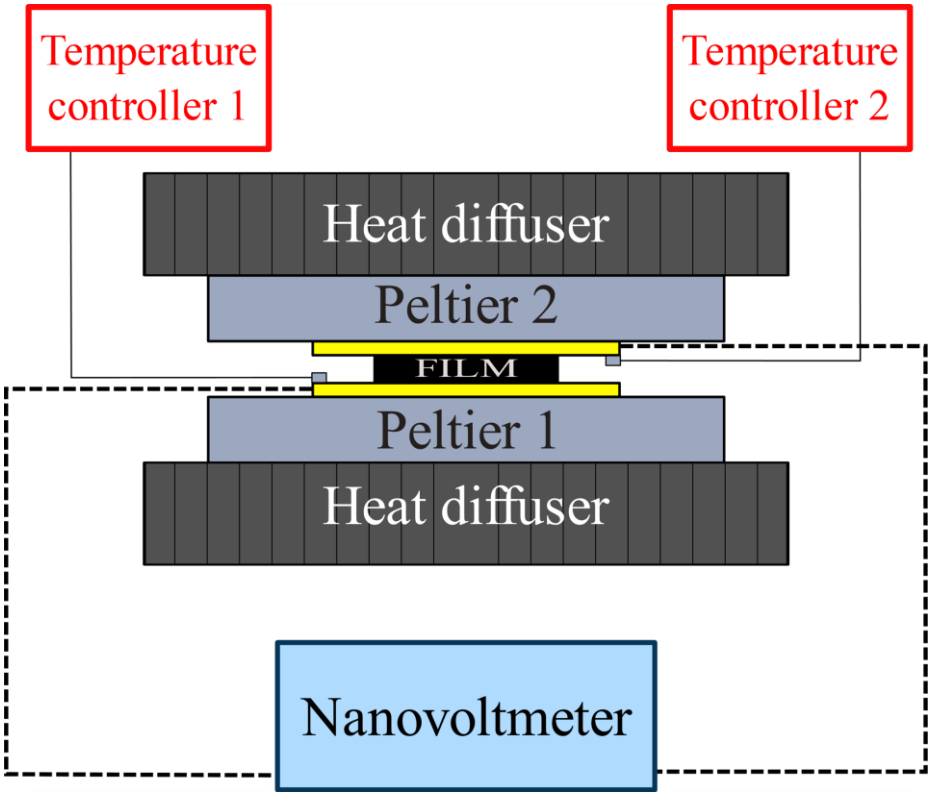

Figure III.10: Schematic representation of the set up used in thermoelectric measurements

The film is introduced between two glasses coated with Ti/Au. Whereas, the temperature sensors are on the surface of the glasses.

Seebeck effect

When a circuit is formed by two homogeneous metals, A and B, with two junctions at different temperatures, T and $T+\Delta T$, a current density J appears. This behavior is known as Seebeck effect and it is quantified with the Seebeck coefficient that is given by:

Appendix I

$$S = \frac{\Delta V}{\Delta T} \qquad \text{(III.20)}$$

The Seebeck coefficient is the slope in the graphics V vs ΔT that it is represented usually. This concept gives the efficiency of a thermoelectric process, so bigger slopes more efficient material.

I. 4. Other methods

- Elemental analysis (C, H, N and S) were carried out by the Servei de Microanàlisi of the Consell Superior d'Investigacions Científiques (CSIC, Barcelona).
- Infrared spectra were recorded in the 4000-400 cm^{-1} range with a Bruker Optics FT-IR Alpha spectrometer using the ATR mode.
- ^{1}H and ^{13}C NMR spectra were recorded on a Bruker Fourier 300 Hz NMR spectrometer. The residual solvent peak was used as internal reference.
- Powder X-ray diffraction (PXRD) data were collected on a D8 Advance Series 2Theta/Theta powder diffractometer.
- Thermogravimetric analyses (TGA) were performed with a TGA/SDTA851 Mettler Toledo instrument with a heating rate of 10ºC min^{-1} between 25 and 500ºC under a constant flow of nitrogen (80 mL min^{-1}).
- Magnetic susceptibility measurements between 2-400 K were carried out in a Quantum Design MPMS-XL SQUID magnetometer under a 1000 Oe field. Each sample was secured inside a gel capsule with glass wool, and the capsule was

María del Pilar Maldonado Illescas

pinched (0.5 mm diameter hole) on the top to allow convenient purging of the interior of the capsule. Pascal constants were used to correct the diamagnetic contribution.

- I-V curves were performed with a sourcemeter (Keithley series 2400) as a current source and a nanovoltmeter (Keithley series 2182A) as voltage data gathering.
- SEM images were obtained with Scanning electron microscopy (SEM) micrographs were acquired on an FEI Quanta 650 FEG ESEM, 20 kV, equipped with an Oxford EDX analyzer (Oxford Instruments).
- Single Crystal X-ray Diffraction Data Collection and Refinement. The measured crystals were prepared under inert conditions immersed in perfluoropolyether as protecting oil for manipulation. The crystal structure determination was carried out using a Bruker-Nonius diffractometer equipped with an APEX II 4K CCD area detector, a FR591 rotating anode with MoKα radiation, Montel mirrors as monochromator, a Kappa 4-axis goniometer and an Oxford Cryosystems low temperature device Cryostream 700 plus (T = -173 °C). Full-sphere data collection was used with ω and ϕ scans. Programs used were as follows: data collection with APEX II (Data collection with APEX II, version v2013.4-1, Bruker (2007). Bruker AXS Inc., Madison, Wisconsin, USA) data reduction with Bruker Saint (Data reduction with Bruker SAINT version V8.30c. Bruker (2007). Bruker AXS Inc., Madison, Wisconsin, USA) and absorption correction with SADABS (SADABS: V2012/1 Bruker (2001). Bruker AXS Inc., Madison, Wisconsin, USA.

Appendix I

Blessing, R. H. Acta Crystallogr. 1995, A51, 33). The crystal structure solution was achieved using direct methods as implemented in SHELXTL SHELXTL version V6.14: G. M. Sheldrick, Acta Crystallogr. 2008, A64, 112) and visualized using the program XP. Missing atoms were subsequently located from difference Fourier synthesis and added to the atom list. Least-squares refinement on F2 using all measured intensities was carried out using the program SHELX-2013. All nonhydrogen atoms were refined including anisotropic displacement parameters. Crystal data collection and refinement are given in Table S1. Compound **1** crystallizes with a high degree of disorder with one molecule of an anionic trimetalic complex, six dimethylammonium cations and five water molecules in the asymmetric unit. In the main molecule all the sulfonate groups are disordered in different orientations (ratios: 0.45, 0.52, 0.69, 0.33, 0.54, 0.11). The dimethylammonium cations are highly delocalized disordered in 16 positions (ratios: 0.5, 0.5, 0.25, 0.25, 0.5, 0.5, 0.5, 0.25, 0.5, 0.25, 0.5, 0.25, 0.5, 0.25, 0.25, 0.25). Also the five water molecules are disordered in 14 positions (ratios: 0.5, 0.5, 0.25, 0.5, 0.5, 0.25, 0.25, 0.5, 0.25, 0.25, 0.25, 0.5, 0.25, 0.25) mixed with the dimethylammonium cations. CCDC 1016539 contains the supplementary crystallographic data for this paper. These data can be obtained free of charge from The Cambridge Crystallographic Data Centre via www.ccdc.cam.ac.uk/data request/cif.

APPENDIX II

Crystallographic data

UNIVERSITAT ROVIRA I VIRGILI
AVANCES EN SISTEMAS INTERACTIVOS PARA PERSONAS CON PARÁLISIS CEREBRAL
María del Pilar Maldonado Illescas

Crystallographic data for $(Me_2NH_2)_6[Fe_3(\mu\text{-}L)_6(H_2O)_6]$ (1)

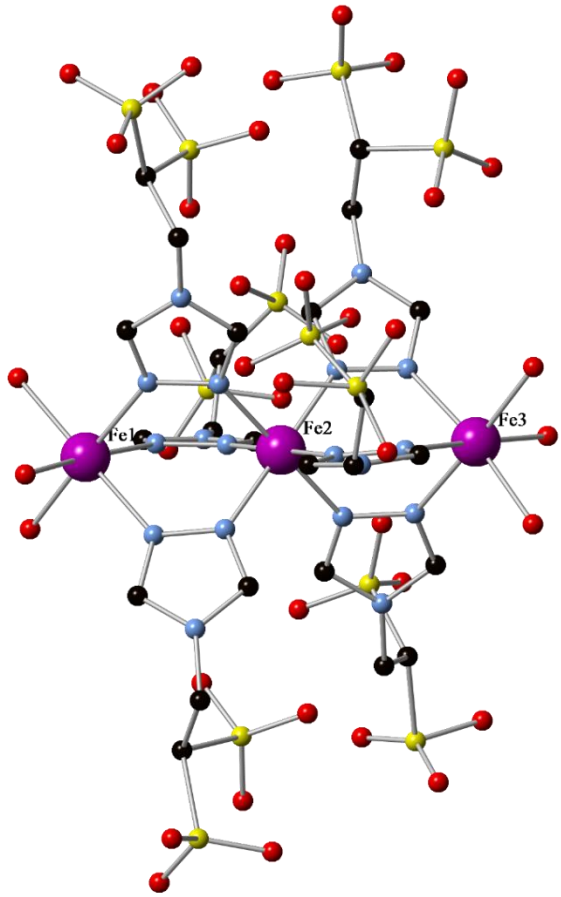

Figure I. 1. Labeling in molecular structure of $(Me_2NH_2)_6[Fe_3(\mu\text{-}L)_6(H_2O)_6]$ (H-atoms omitted for clarity). Color code: Fe = purple; S = yellow; O = red; N = blue; C = black

Appendix II

1·5H$_2$O	
Chemical formula	$C_{36}H_{100}Fe_3N_{21}O_{47}S_{12}$
Formula weight	2173.66
***λ* (Å)**	0.71073
***T* (K)**	100(2)
Crystal system	Triclinic
Space group	$P\bar{1}$
Crystal size (mm^3)	0.20×0.04×0.02
***a* (Å)**	14.287(5)
***b* (Å)**	15.1581(6)
***c* (Å)**	21.3262(9)
***α* (º)**	80.3780(14)
***β* (º)**	84.2804(13)
***γ* (º)**	83.7729(14)
V (Å^3)	4492.5(3)
Z	2
$\rho_{calcd.}$ (g cm^{-3})	1.607
μ (mm^{-1})	0.860
***F*(000)**	2260
Reflections collected	64559
Independent reflections	23819 [R(int) = 0.0340)]
Absorption correction	Empirical
θ range (º)	1.37 – 29.15
Data / restraints / parameters	23819 / 3588 / 2115
Goodness-of-fit on F^2	1.047
R_1 (I >2σ(I))	0.0740
wR_2 (I >2σ(I))	0.2217

Table I. 1. Crystallographic data for (1)

Distance / *Å*			Angle / º
Fe1-N9	2.149(2)	O37-Fe1-N11	89.62(9)
Fe1-O37	2.115(2)	O37-Fe1-N15	94.62(9)
Fe1-N11	2.156(2)	O37-Fe1-O38	90.95(10)
Fe1-O38	2.086(2)	O38-Fe1-N15	89.76(9)
Fe1-N15	2.172(2)	N11-Fe1-N15	86.01(8)
Fe1-O39	2.133(2)	N2-Fe2-N12	179.63(9)
Fe2-N2	1.985(2)	N8-Fe2-N17	179.63(9)
Fe2-N12	1.985(2)	N6-Fe2-N14	179.39(8)
Fe2-N8	1.982(2)	N6-Fe2-N2	91.87(8)
Fe2-N17	1.999(2)	N6-Fe2-N8	88.40(9)
Fe2-N6	1.993(2)	N2-Fe2-N8	88.03(8)
Fe2-N14	2.006(2)	N14-Fe2-N2	87.52(9)
Fe3-N3	2.148(2)	N14-Fe2-N8	91.53(9)
Fe3-O42	2.103(2)	O40-Fe3-N5	178.44(9)
Fe3-N5	2.145(2)	O42-Fe3-N3	176.66(9)
Fe3-O40	2.118(2)	O41-Fe3-N18	171.87(14)
Fe3-N18	2.181(4)	N5-Fe3-N18	90.06(12)
Fe3-O41	2.120(2)	O42-Fe3-N18	95.45(14)
O37-Fe1-N9	176.68(9)	O40-Fe3-O42	89.56(9)
O38-Fe1-N11	175.76(9)	O40-Fe3-N18	91.49(13)
O39-Fe1-N15	173.96(9)	O42-Fe3-N5	90.44(8)

Table I. 2. Selected bond lengths (Å) and angles (º) for (1)

Appendix II

Crystallographic data for $(Cs)_6[Fe_3(\mu\text{-}L)_6(H_2O)_6]$ (2)

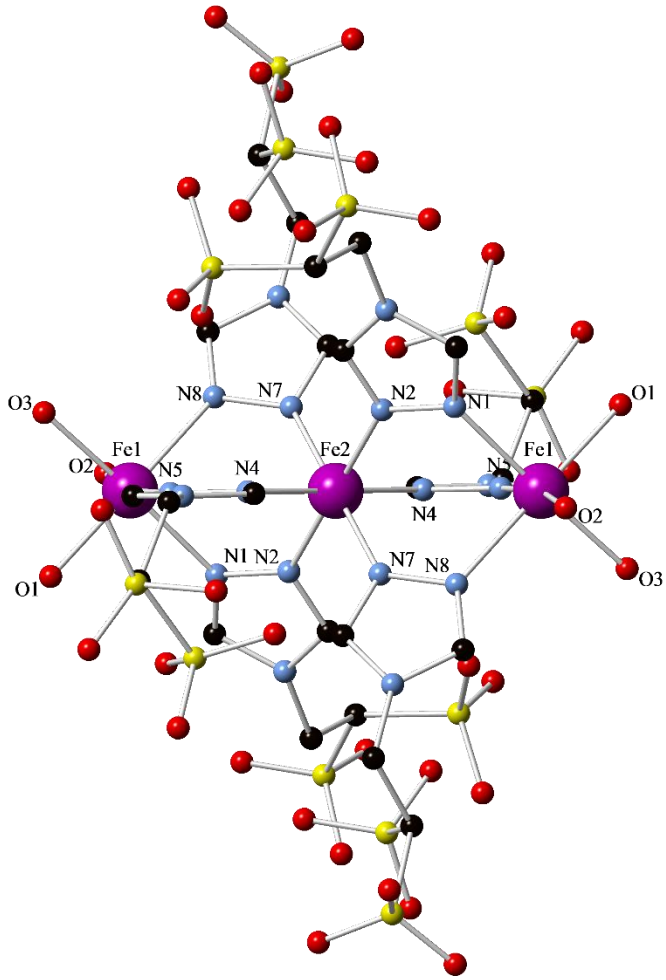

Figure I. 2. Labeling in molecular structure of $Cs_6[Fe_3(\mu\text{-}L)_6(H_2O)_6]$ (H-atoms omitted for clarity). Color code: Fe = purple; S = yellow; O = red; N = blue; C = black

María del Pilar Maldonado Illescas

2·13H$_2$O	
Chemical formula	$C_{24}H_{68}Cs_6Fe_3N_{18}O_{55}S_{12}$
Formula weight	2838.69
λ (Å)	0.71073
T (K)	100(2)
Crystal system	Monoclinic
Space group	C2/c
Crystal size (mm3)	0.40x0.02x0.01
a (Å)	34.4273(12)
b (Å)	11.4107(4)
c (Å)	26.1316(9)
α (º)	90
β (º)	128.2290(8)
γ (º)	90
V (Å3)	8064.0 (5)
Z	4
ρcalcd. (g cm-3)	2.631
μ (mm-1)	3.631
F(000)	5512
Reflections collected	38646
Independent reflections	9659[R(int) = 0.0364]
Absorption correction	Multi-scan
θ range (º)	1.583- 28.010
Data / restraints / parameters	9659/ 922/ 585
Goodness-of-fit on F2	1.029
R1 (I >2σ(I))	0.0679
wR2 (I >2σ(I))	0.1971

Table I. 3. Crystallographic data for (2)

Appendix II

Distance / Å			Angle / º
Fe1-N1	2.174(6)	N1-Fe1-N5	90.8(2)
Fe1-N5	2.184(7)	O1-Fe1-N8´	175.2(2)
Fe1-N8	2.199(6)	O3-Fe1-N8´	91.8(2)
Fe1-O1	2.076(5)	O2-Fe1-N8´	85.2(2)
Fe1-O3	2.098(6)	N1-Fe1-N8´	90.4(2)
Fe1-O2	2.173(6)	N5-Fe1-N8´	85.2(2)
Fe2-N7	1.961(6)	N7-Fe2-N7´	180.0
Fe2-N7´	1.961(6)	N7-Fe2-N4	87.1(2)
Fe2-N4	1.968(6)	N7-Fe2-N4´	92.9(2)
Fe2-N4´	1.968(6)	N7-Fe2-N4´	92.9(2)
Fe2-N2	1.976(6)	N7´-Fe2-N4´	87.1(2)
Fe2-N2´	1.976(6)	N4-Fe2-N4´	180.0
O1-Fe1-O3	86.3(2)	N7-Fe2-N2	86.9(3)
O1-Fe1-O2	99.3(2)	N7-Fe2-N2´	93.1(3)
O3-Fe1-O2	92.5(2)	N4-Fe2-N2	92.3(2)
O1-Fe1-N1	91.4(2)	N4-Fe2-N2´	87.7(2)
O3-Fe1-N1	177.7(2)	N7-Fe2-N2´	93.1(3)
O2-Fe1-N1	88.3(2)	N7´-Fe2-N2´	86.9(3)
O1-Fe1-N5	90.3(2)	N4-Fe2-N2´	87.7(2)
O3-Fe1-N5	88.8(2)	N4´-Fe2-N2´	92.3(2)
O2-Fe1-N5	170.4(2)	N2-Fe2-N2´	180.0(3)

Table I. 4. Selected bond lengths (Å) and angles (º) for (2)

APPENDIX III

Hall effect measurements

UNIVERSITAT ROVIRA I VIRGILI
AVANCES EN SISTEMAS INTERACTIVOS PARA PERSONAS CON PARÁLISIS CEREBRAL
María del Pilar Maldonado Illescas

María del Pilar Maldonado Illescas

Hall effect measurements for (4)/polypyrrole composite and polypyrrole films

The current is applied between two contacts and the voltage is measured between the others. The disposition of the contact are shown in the figure.

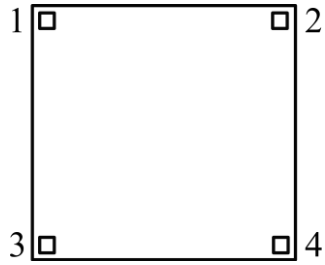

Figure II.1. Van der Pauw contacts

As it is explained in appendix III, measurements are done with and without magnetic field. In this case, a permanent magnet with 14000 G of magnetic field is employed. Following, the values of voltage for the composite are summarized in the table II.2. The sign of the magnetic film indicates the direction of the field.

In addition, Hall effect also was calculated for a film of polypyrrole at the same condition of synthesis and formation of the pellets. Table II.2 summarizes these measurements.

Appendix III

Resistivity Measurements		Hall Voltage Measurements	
Field, B = 0		**+B Field**	
I / µA	**V / mV**	**I / µA**	**V / mV**
I_{21} = 1	V_{34} = 26.6	I_{13} = 1	V_{24P} = -20.3
I_{12} = 1	V_{43} = 26.5	I_{31} = 1	V_{42P} = -20.3
I_{32} = 1	V_{41} =6.2	I_{42} = 1	V_{13P} = 20.5
I_{23} = 1	V_{14} =6.2	I_{24} = 1	V_{31P} = 20.5
I_{43} = 1	V_{12} = 26.7	**-B Field**	
I_{34} = 1	V_{21} = 26.5	**I / µA**	**V / mV**
I_{14} = 1	V_{23} = 6.3	I_{13} = 1	V_{24N} = -36
I_{41} = 1	V_{32} = 6.3	I_{31} = 1	V_{42N} = -35.1
		I_{42} = 1	V_{13N} = 34.7
		I_{24} = 1	V_{31N} = 34.6

Table II.1. Measured voltage for composite films

Resistivity Measurements		Hall Voltage Measurements	
Field, B = 0		**+B Field**	
I / mA	**V / mV**	**I / µA**	**V / mV**
I_{21} = 1	V_{34} = -0.9	I_{13} = 1	V_{24P} = 0.3
I_{12} = 1	V_{43} = -0.9	I_{31} = 1	V_{42P} = 0.3
I_{32} = 1	V_{41} = -0.75	I_{42} = 1	V_{13P} = -0.3
I_{23} = 1	V_{14} = -0.75	I_{24} = 1	V_{31P} = -0.3
I_{43} = 1	V_{12} = 1	**-B Field**	
I_{34} = 1	V_{21} = 1	**I / µA**	**V / mV**
I_{14} = 1	V_{23} = 1	I_{13} = 1	V_{24N} = 0.3
I_{41} = 1	V_{32} = 1	I_{31} = 1	V_{42N} = 0.3
		I_{42} = 1	V_{13N} = -0.3
		I_{24} = 1	V_{31N} = -0.3

Table II.2. Measured voltage for polypyrrole films

DOCTORAL THESIS

SPIN CROSSOVER PHENOMENA: TOWARDS MOLECULE-BASED MEMORIES AND SWITCHES

MARÍA DEL PILAR MALDONADO ILLESCAS

2017

UNIVERSITAT ROVIRA I VIRGILI
AVANCES EN SISTEMAS INTERACTIVOS PARA PERSONAS CON PARÁLISIS CEREBRAL
María del Pilar Maldonado Illescas

UNIVERSITAT
ROVIRA i VIRGILI